THESIS

HEAT TRANSFER ENHANCEMENT IN TWO-PHASE MICROCHANNEL HEAT EXCHANGERS FOR HIGH HEAT FLUX ELECTRONICS

Submitted by

Jensen Hoke

Department of Mechanical Engineering

In partial fulfillment of the requirements

For the Degree of Master of Science

Colorado State University

Fort Collins, Colorado

Spring 2020

Master's Committee:

Advisor: Dr. Todd Bandhauer

Dr. Bret Windom
Dr. Karan Venayagamoorthy

ABSTRACT

HEAT TRANSFER ENHANCEMENT IN TWO-PHASE MICROCHANNEL HEAT EXCHANGERS FOR HIGH HEAT FLUX ELECTRONICS

Laser diodes are semiconductor devices that emit high intensity light with a small spectral bandwidth when a forward voltage is applied. Laser diodes have a high electrical to light conversion efficiency which can be greater that 50%. These robust, high efficiency laser sources are used in medical and manufacturing fields and, if their power can be increased, show promise in inertial confinement fusion and defense applications. Individual diode emitters are arrayed into bars with a footprint of 1 mm by 10 mm to increase their light output power. These bars are further combined into arrays with the light emitting edges stacked close together. As the spacing in these arrays are reduced to increase brightness, thermal management becomes the limiting factor for each bar. State of the art diode arrays can have heat fluxes exceeding 1 $\mathrm{kW\,cm^{-2}}$. Effective thermal management strategies are key because the diode's output wavelength, bandwidth, efficiency and lifetime are temperature dependent.

Commercially available high powered laser diode arrays are traditionally cooled using a single-phase fluid passing through conduction coupled copper-tungsten channels. These heat exchangers have high thermal resistances which require the coolant to be significantly subcooled before entering the device. High working fluid flow rates are required to reduce thermal gradients in the diode bars and working fluid conditioning is required to reduce corrosion in the cooling plates. Many of these issues can be addressed by cooling the diodes with a two-phase working fluid in a corrosion resistant, silicon microchannel heat exchanger. The high heat transfer coefficients associated with flow boiling, as well as the high surface area to volume ratios in microchannel arrays allow the working fluid temperature to be much closer to that of the diode which reduces the cooling load on a system level. Additionally, as heat is added to a two-phase fluid, there is virtually no

change in temperature. Therefore, the working fluid flow rate can be much lower than a comparable single-phase heat exchanger, which reduces pump work. However, using a two-phase working fluid presents its own unique set of challenges.

This work presents a novel approach to increasing the effective critical heat flux and reducing thermal resistance in an array of 125 high aspect ratio silicon microchannels (40 μm$\times$ 200 μm) subjected to heat fluxes up to 1.27 $\mathrm{kW\,cm^{-2}}$. R134a is used as the two-phase working fluid and outlet vapor qualities up to 80.7% are reported. The silicon heat exchangers are manufactured using a DRIE MEMS process that allows fine control over feature sizes. The performance of traditional plain walls is compared to a novel sawtooth structuring pattern that increases available heat transfer area by 41% and provides bubble nucleation sites. A 17% decrease in thermal resistance is reported for one of the area enhancement schemes and critical heat flux is increased in both area enhanced parts.

A thermal FEA model is used to determine heat transfer coefficients and local heat fluxes within the test section. This model is used to investigate alternate patterning schemes. An adjustment to the Bertsch two-phase heat transfer coefficient is also suggested for smaller microchannels geometries and higher heat fluxes. Examination of the model results show that performance increase observed in the area enhanced test sections is driven by an increase in bubble nucleation sites. The additional area available for heat transfer has little effect because reduction of heat flux at the fluid wall interface reduces two-phase heat transfer coefficients. This effect is driven by the relative importance of nucleate boiling in these small channels.

ACKNOWLEDGEMENTS

I would like to thank my partner Erika for her unwavering support, enthusiasm and patience through this process. I'm so grateful that you brought me to CSU and encouraged me in pursuing a Master's. It's always nice to have someone to lend a sympathetic ear and remind me that at least it's not veterinary school.

I would also like to thank my parents who supported my decision to return to school. That support has been life changing and I can't imagine

The members of the ITS lab, specifically Derek Young, David Hobby, Shane Garland, Josh Ritchey, and Bryan Burk deserve special recognition as well. I'm truly grateful to have landed in a lab filled with these individuals.

Additionally I would like to thank the members of the Lawerence Livermore National Lab team, Jack Kotovsky, Paul Fontejon, Taylor Bevis and Julie Hamilton, without whom, this work would not have been possible.

Finally, I would like Dr Todd Bandhauer for his support, council, and the time spend teaching and troubleshooting; it's been a great couple years.

TABLE OF CONTENTS

LIST OF TABLES

LIST OF FIGURES

LIST OF SYMBOLS

Symbol	Description	Units
A	Area	m^2
B	Bias Uncertainty	mixed
Bo	Boiling Number	-
C	Specific Heat	$\mathrm{kJ\,kg^{-1}K^{-1}}$
Co	Confinement Number	-
D	Diameter	m
e	Euler's Constant	-
f	Friction Factor	-
G	Mass Flux	$\mathrm{kg\,m^{-2}s^{-1}}$
h	Heat Transfer Coefficient	$\mathrm{Wm^{-2}K^{-1}}$
I	Current	Amps
i	Enthalpy	$\mathrm{kJ\,kg^{-1}}$
k	Conductivity	$\mathrm{W\,m^{-1}K^{-1}}$
K	Coverage Factor	-
L	Length	m
M	Molecular Mass	$\mathrm{g\,mol^{-1}}$
N	Number of Samples	-
Nu	Nusselt Number	-
P	Pressure	kPa
p	Random Sampling Error	-
Pr	Prandtl Number	-
Q	Heat	W
q''	Heat Flux	$\mathrm{W\,m^{-2}}$
r	Radius	m
R	Resitance	mixed
Re	Reynolds Number	-
RMSE	Root Mean Square Error	mixed
See	Standard Error of Estimation	mixed
Sx	Standard Deviation	mixed
T	Temperature	$^\circ\mathrm{C}$
U	Uncertainty	mixed
V	Voltage	V
We	Weber Number	-
w	Width	m
X	Martinelli Parameter	-
x	Quality	-

Greek Symbols

Symbol	Description	Units
β	Roughness Angle	$^{\circ}\mathrm{C}$
Δ	Change	-
λ	Wavelength	nm
μ	Dynamic Viscosity	Pa s
ν	Kinematic Viscosity	$\mathrm{m}^2\mathrm{s}^{-1}$
ω	Beam Radius	m
σ	Surface Tension	$\mathrm{N\,m}^{-1}$
$\sum$	Sum	-
θ	Contact Angle	$^{\circ}$

Subscripts

Symbol	Description
A	per unit area
adb	adiabatic
ae	area enhancement
amb	ambient
avg	average
c	critical
cb	convective boiling
cond	conduction
conv	convection
cs	calibrated standard
di	dryout incipience
fo	fluid only
h	hydraulic
H	heated
in	inlet
l	liquid
max	maximum
min	minimum
nb	nucleate boiling
out	outlet
rad	radiation
sat	saturation, saturated
sp	single-phase
tp	two-phase
v	vapor
vap	vaporization
w	wall

Chapter 1: Introduction

1.1 Background and Motivation

Laser light has several properties that make it of interest. Generally, light from a laser source is emitted as a beam, meaning that it can propagate over long distances with little divergence. This light is also emitted over a narrow optical bandwith and can be emitted either continuously or in short pulses depending on the application. Producing a high brightness, narrow bandwith light that can easily be focused is useful in a variety of cases. In manufacturing, lasers are used for cutting, welding and soldering. These processes are accomplished with higher precision and lower stress in the material as compared to traditional manufacturing methods such as drilling or cutting. In medicine, lasers are used in procedures ranging from LASIK to surgery. High-power laser systems are one method of creating fusion reactors. In this chapter, the methods of creating a laser will be explored and semiconductor lasers will be explained in depth in Section 1.1.1. The thermal management of these laser sources will be outlined in Section 1.2.

1.1.1 Diode Bars

Laser diodes are an electrically pumped solid state laser source. The diode is formed from a P-n junction bounded by reflective, polished mirrors. When a forward bias is applied, as shown in Figure 1.1, negatively charged electrons and positively charged holes migrate toward the junction. When they combine in the junction, energy is released either as heat (phonon) or light (photon). If the latter occurs, the photon will reflect between the polished surfaces, occasionally striking excited particles. When this collision occurs, the excited particle will be induced to release a photon at the same wavelength. In this way, a buildup of light with a narrow spectral width occurs in the junction. Eventually, this light migrates to the edge of the diode structure and is emitted [4]. Light emitted from the diode can either be focused and used directly, coupled into a fiber optic beam, or pumped into a laser gain medium to increase power.

Laser diodes, as described above, are advantageous over other methods of creating lasers, such as light pumped cavity lasers, because wall plug efficiencies for laser diodes can exceed 50%. For

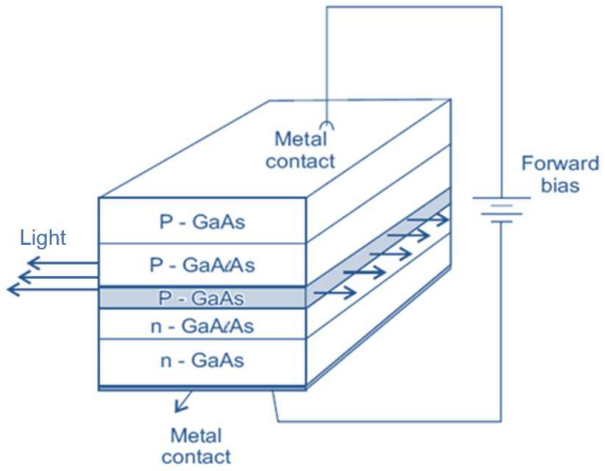

Figure 1.1: Laser diode P-n junction [1]

comparison, flash lamp pumped lasers can be have efficiencies as low as 10% [5]. Additionally, diodes are much more compact and robust than light pumped lasers.

As higher power outputs are required, single diode emitters as described in Figure 1.1 and shown in Figure 1.2(a) can be arrayed into a bar as shown in Figure 1.2(b). Bars can then be further combined into an array as shown in Figure 1.2(c) where the the packaging shown in beige is thermal management architecture. A key parameter of free space diode arrays is pitch. This metric, which refers to the bar to bar spacing, is shown in Figure 1.2(c). Pitch is important because it effectively controls the brightness (radiance) of the output beam. However, as the diode pitch is reduced to increase brightness, volumetric heat loads increase and thermal management becomes more challenging. Brightness will be discussed further in the following section.

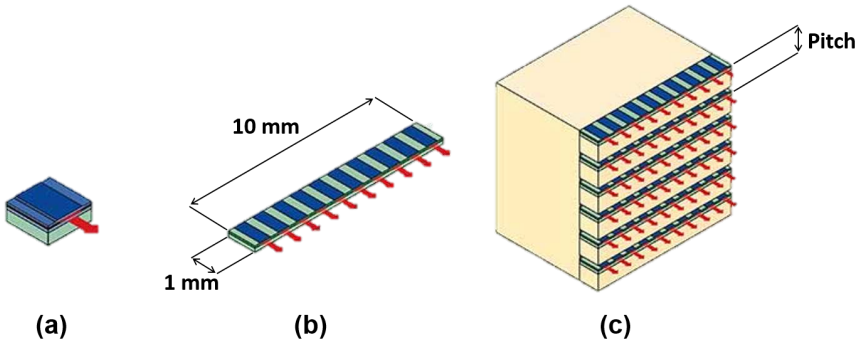

Figure 1.2: Laser diode emiter (a), bar (b) and array (c) with corresponding dimensions.

1.1.1.1 Beam Coupling

Packaging of laser diodes can be divided into two general categories based on the beam coupling techniques: free space and fiber coupled. The focus of this work is the examination of free space diodes, where each diode is packaged close together and simple optics are used to focus the beam. Fiber coupled diodes, on the other hand, can be spaced further apart by using fiber optic cables to bring beams together. However, this is done at the cost of more complicated optics as well as decreased coupling efficiencies. An example of each is shown in Figure 1.3.

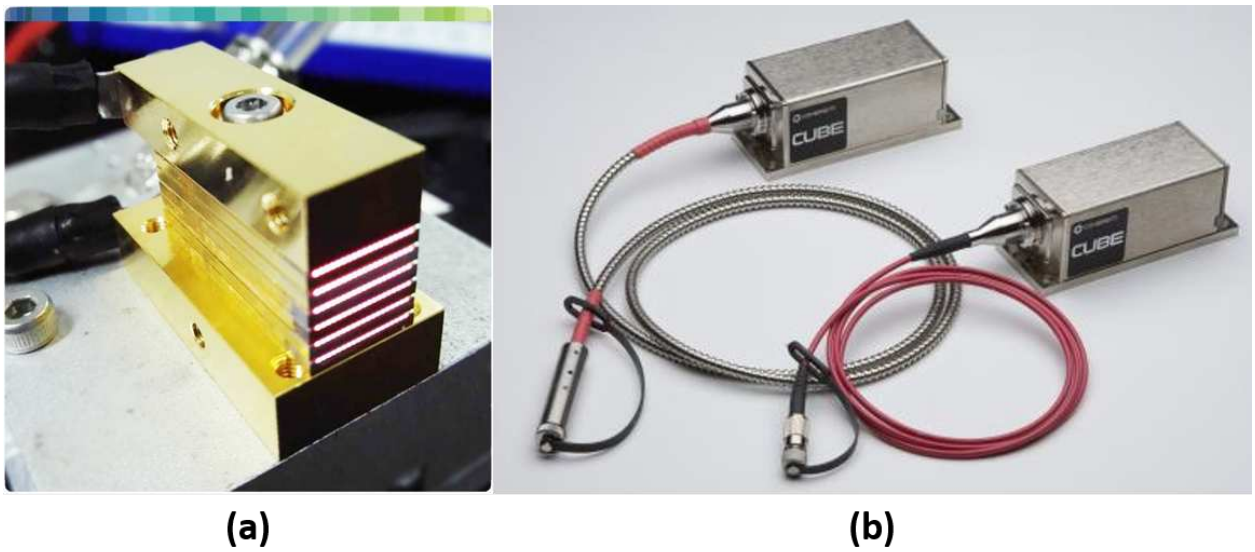

Figure 1.3: A comparison of free space(a) and fiber coupled(b) diode packages.

Free space diode arrays consist of several bars stacked closely and packaged in a forced convection cooling architecture. Each bar is coupled with a fast axis collimating (FAC) lens that runs the length of the bar. In contrast, fiber coupled packages usually contain only a few small bars as well as an optical assembly to focus the beam into the fiber. In fiber coupled packages, thermal management can often be accomplished with thermoelectric coolers because the spacing between diode bars is greater.

1.1.1.2 Brightness, Beam Quality and Efficiency

In this section, three important parameters that measure the performance of laser diode bars will be defined. In general, each of these parameters is tied in some way to the temperature of the diode bar. This highlights the need for effective thermal management strategies.

Brightness, as it applies to lasers, is often used as a qualitative term to describe luminance. In this work, brightness is narrowly defined to mean radiance. Radiance is defined in equation 1.1 using the paraxial assumption [6].

$$\begin{aligned} R &= \frac{P}{\pi\omega_{\mathrm{o}}^2\pi\theta^2} \\ &= \frac{P}{\pi\omega_{\mathrm{o}}^2\left(\frac{\lambda}{\pi\omega_{\mathrm{o}}}\right)^2} \\ &= \frac{P}{\lambda^2} \end{aligned} \tag{1.1}$$

In equation 1.1 it can be seen that brightness depends on power, *P*, as well as beam radius, ω [7], and beam divergence, θ [8], which can be defined in terms of wavelength, λ.

Brightness is an important parameter because it is often difficult to increase brightness beyond the source brightness using simple optics. For a free space diode focused on a target using a passive lens, if brightness is increased at the target beyond the brightness of the source, net light transfer will be from the target back to the source. Therefore, average brightness at the array determines the final brightness at the target.

The final metric affecting brightness is beam quality. Beam quality is a measure of how tightly a laser beam can be focused. Beams with high beam quality have smooth wavefronts, meaning that a lens is able to focus such that the wavefronts are plane. Beams with plane wavefronts are desirable because because they can be further focused to a target as shown in Figure 1.6.

A standard metric for beam quality is the M^2 factor, where a diffraction-limited Gaussian beam has the highest beam quality of $M^2 = 1$ [9]. Equation 1.1 was derived assuming a diffraction-limited Gaussian beam and can be expanded to a more general form in equation 1.2.

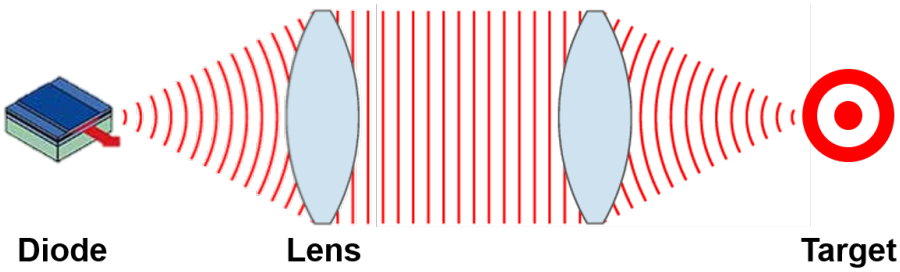

Figure 1.4: Focusing of a beam with plane wavefronts using simple lenses.

$$R = \frac{P}{\left(M^2\right)^2 \lambda^2} \tag{1.2}$$

Many of the properties of laser diodes discussed above depend directly on the diode's temperature. Chief among these is the wavelength of the output light, which affects efficiency. In general, the peak emitted wavelength increases by roughly 0.3 $\mathrm{nm\,K^{-1}}$ [10]. Diodes achieve peak efficiency for a specific wavelength and as the wavelength shifts, efficiency drops [10]. For GaAs diodes, efficiency increases with a decrease in operating temperature. For example, Frevert et. al. [11] showed that decreasing operating temperature from 25°C to -55°C increased the electrical conversion efficiency of a GaAs diode from 62% to 74%. An example of this is shown in Figure 1.5 where applied current is compared to the optical output power on the left axis. The slope of this line is used to calculate the power conversion efficiency (PCE) which is shown on the right axis.

Effective thermal management of laser diode arrays is crutial because the key properties of the output light are all temperature dependent. State of the art thermal management strategies, as well as shortcomings in the field, will be explored in the following section.

1.2 Thermal Management for Laser Diode Arrays

Thermal management strategies for laser diodes have progressed in step with the need for more powerful laser diodes. On average, the power output of a single emitter has grown by roughly 15% per year since the introduction of laser diodes in the early 1960's [10]. For low power bars (< 60 W per bar) conduction cooling is preferred [12]. This method uses a high conductivity material,

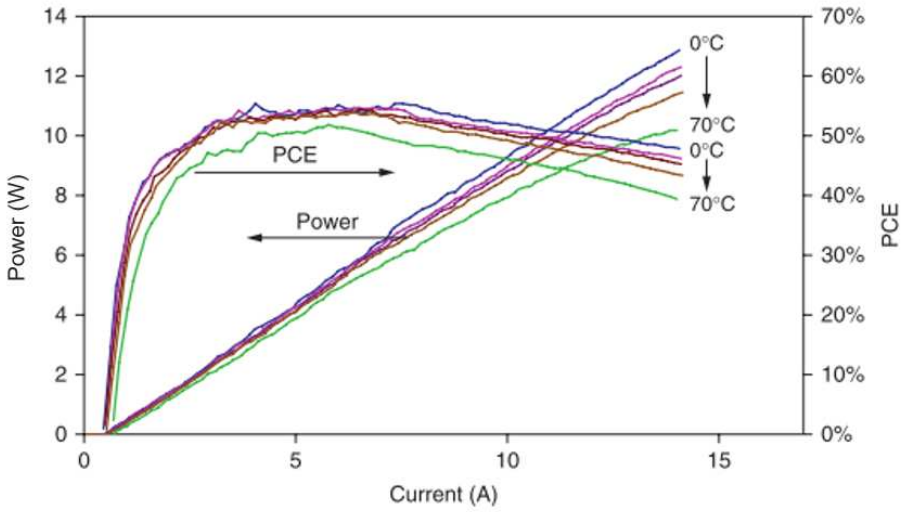

Figure 1.5: Diode temperature effect on power conversion efficiency (PCE) [10].

typically copper, to remove heat from the diode bar. As power increases, active cooling of the diode bar is required. In most cases water is used as the working fluid and state of the art thermal management strategies use microchannels. Two competing criteria determine the material used in the microchannel heat exchanger. Because of its high thermal conductivity, copper is better from a heat transfer standpoint. However, it is important to match the thermal expansion coefficient (CTE) of the diode bar and the substrate on which it is mounted to reduce stress in the diode bar during operation. Many researchers use Copper-Tungsten (CuW) or Aluminum Nitride (AlN) [12] which can be incorporated into any thermal management architecture but it adds a layer, negatively affecting thermal performance.

The highest performance laser diode thermal management system in the literature comes from Skidmore et. al. [13] and is shown in Figure 1.7. This microchannel array consists of an etched silicon block bonded to an etched glass manifold. The thermal resistance is reported to be 0.032 $^{\circ}\mathrm{C\,W^{-1}}$ and a maximum heat flux of 1.5 $\mathrm{kW\,cm^{-2}}$ is achieved. The heat exchangers are constructed by etching silicon wafers with potassium hydroxide, KOH, along the {1,1,1} plane to form triangular recesses on both the top and bottom. The channels are $28\,\mu\mathrm{m}$ wide and located on a 60 μm pitch, leading to a fin thickness of $32\mu\mathrm{m}$. The spacing between diode bars along the plane

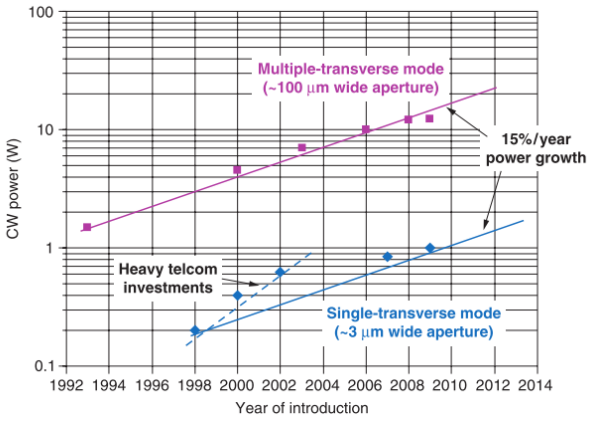

Figure 1.6: Growth in multimode and single-mode continuous wave (CW) power for laser diodes [10].

of the cooler is 1.7 mm. However, diode pitch is measured along the optical axis, so the effective pitch is 0.98 mm.

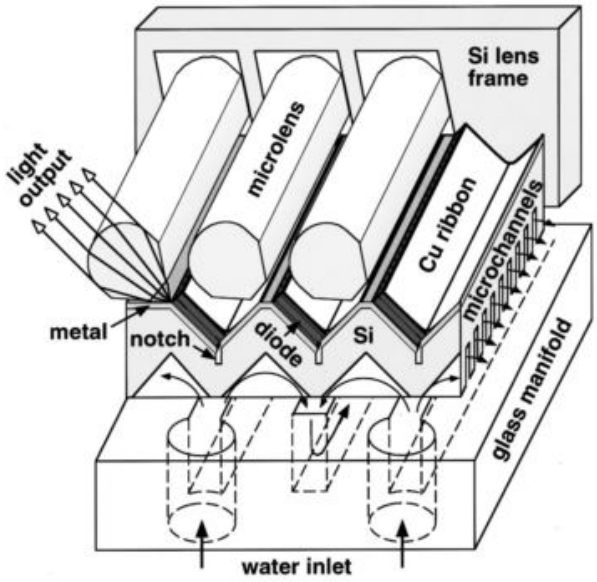

Figure 1.7: Laser diode thermal management system from Skidmore et. al. [13].

1.2.1 Two-Phase Cooling

One novel approach to increasing the performance of laser diode coolers is to introduce flow boiling within the channels. This has several advantages over single-phase flow. First, the heat

transfer coefficients associated with boiling in microchannels can be up to an order of magnitude higher than single-phase heat transfer coefficients for the same flow parameters [14]. Additionally, the high enthalpy of vaporization of fluids allows mass flow rates to be greatly reduced compared to systems using sensible heating. For example, the heat exchanger described by Skidmore et. al. [13], used a flow rate of 0.049 $\mathrm{kg\,s^{-1}}$ which can be used to calculate the temperature rise of the working fluid in equation 1.3.

$$\begin{aligned} \Delta T &= \frac{Q}{\dot{m}C} \\ \Delta T &= \frac{0.149[\mathrm{kW}]}{0.049[\mathrm{kg\,s^{-1}}] \cdot 4.187[\mathrm{kJ\,kg^{-1}K{-}1}]} \\ &= 0.791[^{\circ}\mathrm{C}] \end{aligned} \tag{1.3}$$

where *C* is the specific heat of the fluid.

To find the flow rate required to dissipate the same amount of heat with no rise in temperature by using a two-phase fluid, a similar calculation can be performed. R134a is assumed as the working fluid which has a saturation pressure of 414 kPa at 10°C,similar to the Skidmore et. al. study. An outlet vapor quality of 80% is assumed in equation 1.4.

$$\begin{aligned} \dot{m} &= \frac{Q}{\Delta h_{\mathrm{vap}} \cdot X_{\mathrm{out}}} \\ \dot{m} &= \frac{0.149[\mathrm{kW}]}{191[\mathrm{kJ\,kg^{-1}}] \cdot 0.8} \\ &= 7.8 \times 10^{-4}[\mathrm{kg\,s^{-1}}] \end{aligned} \tag{1.4}$$

where Δh_{vap} is the enthalpy of vaporization of the fluid and X_{out} is the outlet vapor quality.

Comparing the calculated flow rate from equation 1.4 to the data provided by Skidmore et. al., it can be seen that the mass flow rate for the two-phase system is 50 times lower than for the state of the art single-phase system. This corresponds directly to a similar drop in the pumping work required for the system. This is demonstrated using the simplified pump work equation for an incompressible fluid shown in Equation 1.5.

$$\dot{W}_{\text{pump}} = \frac{\dot{m}}{\rho}\Delta P_{\text{pump}} \tag{1.5}$$

Assuming a pressure drop of 10 kPa through both systems, the calculations for pump work for both the single-phase water system and the two-phase R134a system are shown in Equation 1.6.

$$\begin{aligned}
\dot{W}_{\text{pump,sp}} &= \frac{0.049[\text{kg s}^{-1}]}{999.7[\text{kg m}^{-3}]}10,000[\text{Pa}] \\
&= 0.49\text{W} \\
\dot{W}_{\text{pump,tp}} &= \frac{7.8 \times 10^{-4}[\text{kg s}^{-1}]}{1261[\text{kg m}^{-3}]}10,000\text{Pa}] \\
&= 6.2 \times 10^{-3}\text{W}
\end{aligned} \tag{1.6}$$

However, using two-phase cooling in microchannels subjected to high heat fluxes comes with its own set of challenges. For example, flow instabilities are often characteristic of two-phase flow in microchannels in which flow within the channel can reverse. Additionally, microchannels subjected to high heat fluxes with high vapor qualities can experience dryout in which the two-phase heat transfer coefficient drops precipitously. The physics of two-phase flow will be described in detail in section 2.1.

1.3 Research Objectives

The main objective of this effort is to investigate the use of two-phase microchannel coolers for the thermal management of high-powered laser diode arrays. Building on previous work from Bevis et. al. [2] and Burk et. al. [15], this study investigates a novel area enhancement technique with the aim of reducing thermal resistance and increasing critical heat flux in 67 μm hyrdaulic diameter silicon microchannels with a high aspect ratio (5:1).

Experiments were performed to compare an unaltered, plane walled test section to two test sections with area enhancement. The two area enhancement schemes differ in feature height, from 3 μm to 6 μm. The experimental data was input into a modified version of the thermal FEA model presented by Burk et. al. [15] to determine heat spreading through the part, local heat flux, and

local heat transfer coefficients. This novel modeling approach uses a finite element approach to model the solid domain of the microchannel heater. To reduce computational loads, the fluid domain is modeled as a local fluid temperature and heat transfer coefficient. Two-phase heat transfer coefficients are calculated locally at each point on the solid-fluid interface using correlations developed from average heat transfer coefficient conditions. Values, such as local heat flux, are taken from the model and used in the heat transfer coefficient calculation.

The present work contains the following chapters: Literature Review, Experimental Procedure, Data Reduction, Experimental Results, and Conclusion. The literature review is broken into two sections. First, an overview of the physics of microchannel flow boiling is presented which includes a detailed explanation of some of the behaviors limiting widespread use. This is followed by a survey of methods used to address many of these issues. In chapter 3, the experiment is described in detail. This includes both a description of the microchannel coolers themselves as well as overview of the experimental test facility. A detailed explanation of the uncertainty analysis that was performed for this study is also included in chapter 3. In chapter 4, the computational model used is explained. This includes a description of the geometry, an overview of two-phase heat transfer coefficient correlations surveyed, and an explanation of the mesh development. Finally, chapter 5 presents the experimental results and the results from the computational model. In this section, a modification to the most suitable heat transfer coefficient correlation is also presented. Finally, the model is used to investigate other area enhancement geometries with the goal of further increasing the heat exchanger performance. To conclude, chapter 6 presents closing remarks and recommendations for future work.

Chapter 2: Literature Review

As shown above, laser diodes are a robust, efficient way to create laser light, which is useful in a variety of applications. However, effective thermal management strategies will increase their usefulness. Two-phase microchannel coolers are an attractive option. A review of the literature has two aims: to understand the underlying physics of microchannel flow boiling and to investigate improvements to microchannel heat exchanger performance. These two aims are fleshed out in section 2.1 and 2.2 respectively.

2.1 Microchannel Flow Boiling

2.1.1 Bubble Nucleation

Fundamental to boiling in channels is the single-phase to two-phase transition that occurs in the fluid. This can occur one of two ways: homogeneous nucleation or heterogeneous nucleation [16]. Homogeneous nucleation arises from the distribution of energy in a fluid. Some fraction of the molecules in a substance will have higher energy than the bulk fluid. This excess energy causes the molecules to be activated. If a sufficient number of activated molecules occupy the same region of space, a vapor bubble is formed. If the number of molecules is below the vapor bubble formation threshold, they are likely to transfer their energy to neighboring molecules and no bubble is formed. Because the likelihood of a sufficient number of activated molecules occupying the same space is low, homogeneous nucleation is not a driving force in phase change phenomena. As a result, the wall temperatures predicted by assuming homogeneous nucleation can be an order of magnitude higher than those measured in practice.

In systems with heterogeneous nucleation, bubble growth is shown to occur on the bounding surfaces of a system, rather than within the fluid. Therefore, heterogeneous nucleation, which occurs at the solid-liquid interface, must be considered. This is first examined by considering a plane surface as shown in Figure 2.1. Here a vapor bubble of radius r is formed on a solid surface. The contact angle between the solid and fluid is θ. In this situation, the solid is assumed to have some superheat, ΔT, above the bulk liquid temperature. Heat is added to the vapor bubble

along the solid-vapor interface. The vapor will now be above the fluid's saturation temperature, so heat will be transferred from the growing bubble to the bulk fluid along the fluid-vapor interface. The rate at which heat transfer into and out of the bubble occurs will depend on the size of each interface. As the contact angle, θ, decreases, the liquid-vapor interface will grow relative to the solid-vapor interface. This will result in an increase in heat transfer out of the vapor bubble relative to the heat transfer into the bubble. If heat transfer into the bubble outweighs heat transfer from the bubble to the bulk fluid, the bubble will grow until it reaches a critical diameter at which point buoyancy and flow forces will allow it to detach from the wall. Critical bubble diameter depends on several factors including the degree of wall superheat, viscosity and conductivity of the fluid, and flow patterns. Departure diameter is increased for high wall superheats, low thermal conductivity, and low flow rates [17].

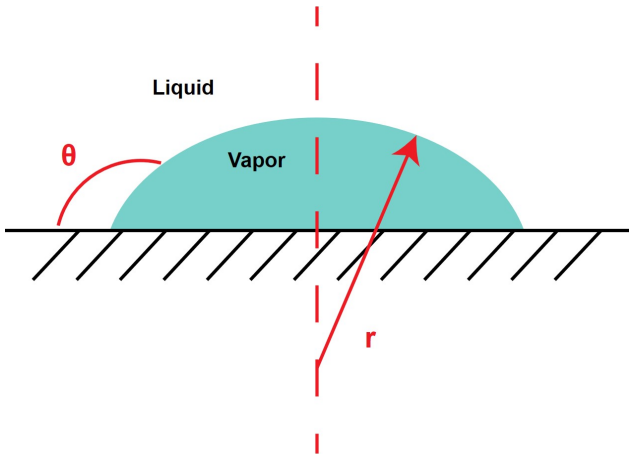

Figure 2.1: Heterogeneous bubble nucleation on a plane surface.

Bubble nucleation is altered when surface roughness is introduced. As seen in Figure 2.2 where a rough surface is shown that is comprised of conical cavities. In this case, a bubble forming in one of these cavities will have a larger solid-vapor interface relative to its vapor-liquid interface when compared to the plane walled case. This will decrease the superheat required to nucleate a bubble and increase the likelihood that a given bubbles will reach the critical diameter required to detach from the wall. The opposite will be true for a bubble forming on the edge or tip of a

rough feature, where the ratio of vapor-solid to vapor-liquid interface area will decrease relative to a bubble forming in the cavity. From the preceding information, it can be concluded that bubbles will form preferentially in cavities over plane faces, within the bulk fluid, or on surface projections. Additionally, poorly wetted surfaces should promote nucleation over well wetted surfaces.

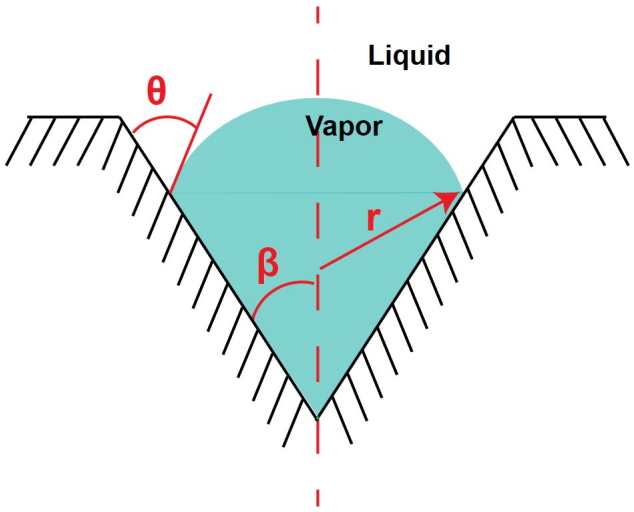

Figure 2.2: Heterogeneous bubble nucleation in a conical cavity.

There are many standards for describing surface roughness and no one parameter fully describes any given surface. Studies investigating the effect of surface on pool boiling typically use the maximum profile peak height, R_{p} [18] which is described by the International Organization for Standardization (ISO) 4287 [19]. The maximum profile peak, R_{p} is defined as the maximum feature height over the measured area as shown in Figure 2.3. Although this is not the most robust parameter available to describe surface roughness, most studies that have examined the effect of roughness on bubble nucleation have used emery paper to texture the surface. In these cases, R_{p} corresponds directly to the roughness of the emery paper used while other parameters such as the arithmetical mean height, R_{a}, are not as easily found.

Not all surface roughness feature sizes will promote bubble nucleation relative to a plane wall. If the feature size is too small, there will be an insufficient solid-vapor interface relative to the liquid-vapor interface and the bubble will shrink. If the feature size is too large, bubbles are

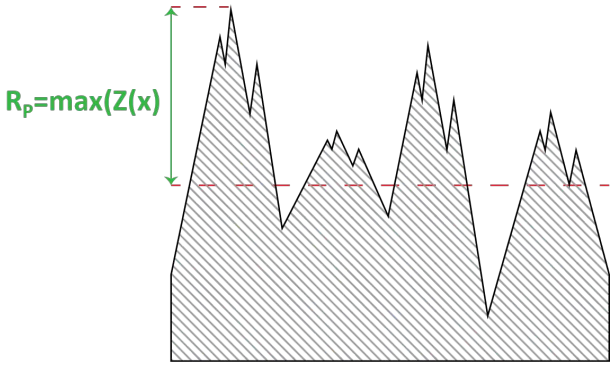

Figure 2.3: Maximum profile peak, R_{p}.

unlikely to bridge to the other side of the feature and the feature acts as a plane wall. Hsu et. al. presents equation 2.1 which give the upper and lower size limit for active nucleation sites [20].

$$r_{\mathrm{c,max,min}} = \frac{\delta}{2C_1}\left[1 - \frac{\theta_{\mathrm{sat}}}{\theta_{\mathrm{w}}} \pm \sqrt{\left(1 - \frac{\theta_{\mathrm{s}}at}{\theta_{\mathrm{w}}}\right)^2 - \frac{4AC_2}{\delta\theta_{\mathrm{w}}}}\right] \tag{2.1}$$

δ, θ_{w}, and θ_{sat} are the thermal boundary layer thickness, wall superheat, and difference between the wall temperature and the fluid saturation temperature respectively. The constants, C_1 and C_2 depend on the angle of nucleation cavity as well as the contact angle between the fluid and solid. Equation 2.1 can be used to produce a plot showing the size range of active nucleation sites for a heat exchanger. An example of this from Kuo et. al. [21] is shown in Figure 2.4. Here the size range of active nucleation sites is shown as a function of wall superheat. Below 5°C, there is not enough wall superheat to initiate bubble nucleation. As wall superheat increases, moving right on the graph, a great range of cavity sizes can nucleate bubbles.

2.1.2 Instability and Backflow

One of the primary behaviors limiting the use of two-phase microchannel heat exchangers is backflow [22]. Instabilities resulting from backflow can cause a number of problems, including inducing mechanical vibrations that can damage system components [23] as well as lowering the vapor quality and heat flux at which dryout occurs [24]. Because of the high heat transfer coefficients associated with boiling in microchannels, bubbles that form do so explosively. A rapidly

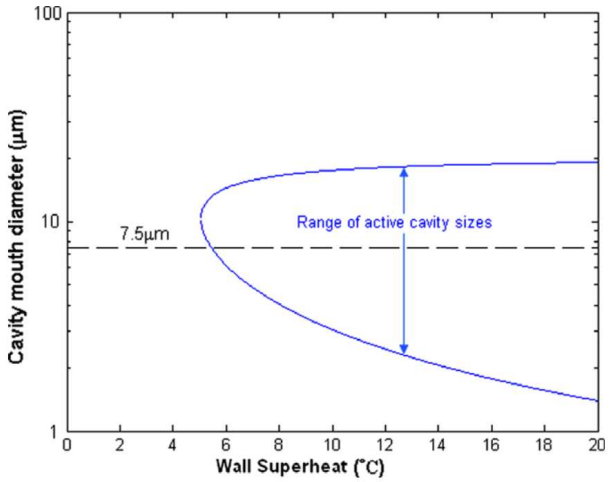

Figure 2.4: Size range of active nucleation sites from Kuo et. al. [21] based on the criteria presented by Hsu [20].

growing bubble that is bounded by the channel walls can only expand along the direction of flow. As this bubble continues to grow, it will expand upstream if the expansion forces momentarily overcome the momentum forces from the upstream fluid [25]. Many authors have reported this behavior during experimentation in microchannels [26, 27] as well as conventionally sized channels. A diagram of this behavior is shown in Figure 2.5.

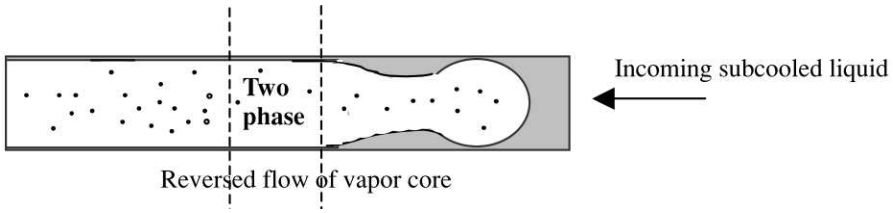

Figure 2.5: Instability resulting from vapor core expanding upstream [24].

Y. Peles [28] studied water in silicon microchannels with hydraulic diameters ranging from 50 μm to 200 μm and found that the single-phase to two-phase transition location varied following fluctuations in flow rate and pressure. Hetsroni et. al. [29] showed that instabilities, like those observed by Peles, resulted in fluctuating and non uniform heater temperatures in silicon microchannels ranging in diameter from 103 μm to 129 μm when cooled with two-phase water.

It was also found that increasing vapor quality lead to an increase in the flow, temperature, and pressure oscillations observed.

Kuo and Peles [21] as well as Park and Thome [30] showed that instabilities resulted in an earlier onset of critical heat flux. The later study showed that flow instabilities reduced critical heat flux by more than 20% at the same flow conditions. Control of flow instabilities will be discussed in section 2.2 and critical heat flux is explained in more detail in section 2.1.3.

2.1.3 Critical Heat Flux

Critical heat flux occurs as the vapor quality in a channel increases as the fluid is heated. Below critical heat flux, vapor bubbles will form on the channel wall, grow until they reach the critical diameter and then ripped away. When the bubble leaves the channel wall, liquid from the anulus will flow in to replace the bubble. When vapor quality is sufficiently high, and high heat fluxes are rapidly generating bubbles, insufficient liquid is available to cover the channel wall. When this happens, the heat transfer mechanism switches to single-phase heat transfer and the heat transfer coefficient drops dramatically. This drop in heat transfer coefficient is accompanied by a spike in wall superheat. This is of critical importance to this study because this spike in wall superheat can easily damage sensitive laser diodes.

This phenomenon is best visualized by considering the flow boiling curve presented in Figure 2.6. This image represents a uniformly heated channel where the working fluid enters as a subcooled liquid, is heated to its saturation temperature and then transitions to a two-phase fluid. Initiallybubbles form on the wall, they are ripped off, and then are pulled along with the bulk fluid. When the fluid reaches its saturation temperature, these bubbles become entrained in the main flow, although the bulk fluid is dominated by liquid. As heat is added along the channel and vapor quality increases, these discrete bubbles begin to coalesce into larger bubbles that take up the center of the channel. While vapor quality is still low, these vapor slugs are separated by liquid. As vapor quality increases further, these vapor slugs now coalesce and the channel center is dominated by vapor surrounded by a liquid annulus. As shown in the Figure 2.6, this is accompanied by the highest heat transfer coefficients. Eventually, the vapor quality increases to such an extent that the

annulus thins dramatically. As a bubble is formed, there is no longer sufficient liquid in the annulus to replace it. Here, the heat transfer mechanism switches from two-phase to single-phase and the heat transfer coefficient drops precipitously [31].

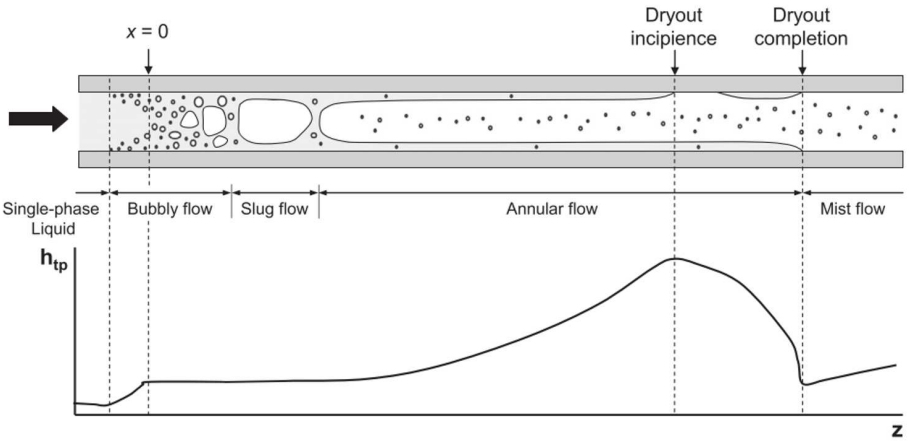

Figure 2.6: Boiling curve for a uniformly heated channel [32].

Dryout incipience is a function of bulk vapor quality and heat flux as well as a number of transport properties [32]. Four primary mechanisms have been proposed to explain dryout incipience. The first of these is the Boundary Layer Separation Model which states that the rate of vapor leaving the wall becomes large enough to reduce to the liquid velocity at the wall to near zero [33]. The Bubble Crowding Model asserts that critical heat flux (CHF) occurs when bubbles departing the channel wall cannot join the vapor annulus and therefore are kept against wall [34]. The Sublayer Dryout Model looks at the thin annuls of liquid at the wall and postulates that CHF occurs when the total enthalpy of vaporization in this annulus is less than the heat being supplied to the channel wall [35]. Finally, the Interfacial Lift-off model looks at the vapor core present during annular flow to explain CHF. The vapor core is often observed to be turbulent and fluctuations along its boundary cause the vapor core to come into contact with the channel wall [36].

2.1.4 Two-Phase Heat Transfer Coefficient

As mentioned above, the two main heat transfer regimes in flow boiling are nucleate boiling and convective boiling. Nucleate boiling, which is also present in pool boiling, is characterized by

the heterogeneous nucleation on the channel wall. As the bubble grows, inertial forces overcome surface tension forces and the bubble leaves the wall, taking heat with it. Convective boiling occurs at the vapor-liquid boundary instead of the solid-liquid boundary. Here, heat is conducted away from the wall, through the liquid, to vapor pockets in the bulk flow. Although many conflicting findings have been presented, in general, nucleate boiling is strongly dependent on local heat flux and independent of mass flow rate. Conversely, convective boiling is directly influenced by mass flux and independent of heat flux at the fluid wall interface. In terms of flow patterns, nucleate boiling occurs in bubbly and slug flow while convective boiling is present more in annular and mist flow regimes.

Although two-phase heat transfer is often described as the superposition of convective and nucleate boiling, many studies have found nucleate boiling to be the dominate regimein microchannels. [37, 38]. In fact, good agreement with experimental data from microchannels is shown in several cases when a correlation developed for pool boiling is used to predict heat transfer [39–41]. Here the pool boiling calculation accounts only for the nucleate boiling regime.

While it is clear that the two-phase heat transfer coefficient depends on flow regime, there is not good agreement on where these regimes begin and end. This is illustrated by examining the conclusions of several studies that cover similarly sized channels with similar refrigerants. Wambsganss et. al. [42] studied R113 in 2.92 mm horizontal tubes, Bao et. al. [43] examined R111 and R123 in 1.95 mm diameter horizontal tubes and Lazarek and Black [44] performed experiments with R113 in 3.1 mm vertical tubes. All three studies found that heat transfer coefficients were strongly dependent on heat flux. Negligible influence of vapor quality was found. Therefore it was concluded that nucleate boiling was the dominant wall heat transfer mechanism. However, Tran et. al. [45] examined 2.46 mm diameter tubes with R12 and found that convective boiling was dominate at low heat fluxes. Furthermore, Yan and Lin [46] studied R134a flow boiling in a 2.0 mm diameter tube and found that the heat transfer coefficient was not influenced by heat flux at high vapor qualities. Finally, in upward flow boiling of heptane in 2.4 mm channels, Wadekar [47] found that the heat transfer coefficient varied strongly with mass flux, indicating a convective boil-

ing regime. From this review it can be seen that there is poor agreement on how to define heat transfer regimes in microchannels.

2.2 Flow Boiling Enhancement

Considering the practical limits in flow boiling, several approaches have been demonstrated to both increase local heat transfer coefficients and suppress dryout incipience. This review focuses specifically on mortification to the channel wall or design and includes inlet restriction, carbon nanotubes, artificial nucleation cavities, micropillars, and vapor extraction. These methods are presented in section 2.2.1 through section 2.2.4.

2.2.1 Inlet Restriction

A common method for reducing instabilities and backflow in microchannel flow boiling is to ensure that pressure drop through the system is not dominated by pressure drop through the channel. This is often accomplished by the introduction of a restriction placed at the inlet to each channel. For example, in a study of 200 μm wide 264 μm deep parallel channels, Kosar et. al. investigated the efficacy of varying the length of a 20 μm wide inlet restriction on reducing flow instabilities and promoting even flow distribution [48]. The inlet restrictions, pictured in Figure 2.7, varied in length from 50 μm to 400 μm and were compared to channels without inlet restrictions. A dimensionless parameter, *M*, was developed to described the increase in pressure drop that resulted from introducing the channels. It was found that the onset of unstable boiling increased asymptotically with *M*. This delay in instability allowed heat loads to increase until critical heat flux became the limiting factor.

2.2.2 Carbon Nanotubes

As discussed in section 2.1.4, nucleate boiling is the dominant heat transfer mechanism in microchannels. For this reason, many of the methods aimed at enhancing heat transfer in microchannels target bubble nucleation, the physics of which are described in section 2.1.1. To reiterate, bubble nucleation is increased by roughening the surface to increase the ratio of vapor-solid to

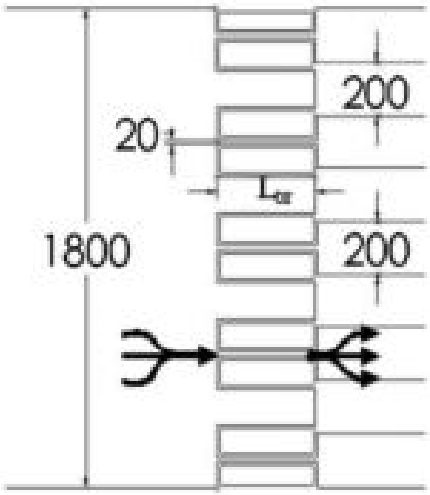

Figure 2.7: Inlet restriction from Kos et. al. [48]. Restriction lengths varied from 50 μm to 400 μm

vapor-liquid interfacial area in a forming bubble. One such method of creating artificial surface roughness in microchannels is through the use of carbon nanotubes (CNTs). Khanikar and Mudawar [49] showed that the introduction of CNT arrays at low mass fluxes reduced wall superheat by increasing bubble nucleation frequency as well as acting as high efficiency fins that penetrate into the bulk fluid. This study covered 44.8 mm long, 10 mm wide, 0.371 mm wide channels where deionized water was used as the working fluid. Heat flux was increased from 33.5 $\mathrm{W\,cm^{-2}}$up to 41.5 $\mathrm{W\,cm^{-2}}$ at the lowest mass flux. For this study, mass flux ranged from 86 $\mathrm{kg\,m^{-2}\,s^{-1}}$ to 386 $\mathrm{kg\,m^{-2}\,s^{-1}}$. At low mass velocities, the CNTs protrude into the flow, increasing surface roughness and inducing turbulence. However, at higher velocities, the CNTs fold and lay flat against the wall, removing any difference from the untreated channels.

Similarly Pranoto et. al. coated the smooth aluminum walls of 80 mm x 60 mm channels with two carbon nanotube structures with different properties and noted an increase in critical heat flux from 66.7 $\mathrm{W\,cm^{-2}}$ to 100 $\mathrm{W\,cm^{-2}}$ [50]. Additionally, they noted that the carbon nanotube structures increased the two-phase heat transfer coefficient by up to 160%. An example of the carbon nanotube structure is shown in Figure 2.8.

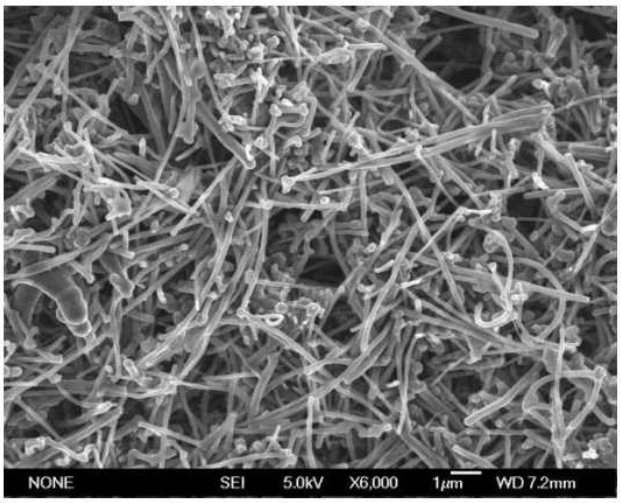

Figure 2.8: Carbon nanotube structure from Pranoto et. al. [50] which promoted an increase in two-phase heat transfer coefficient and critical heat flux.

2.2.3 Nucleation Cavities

Similar to CNTs, cavities can be artificially created by etching patterns that promote bubble nucleation. By altering the microstructure, often of the channel walls, the ratio of vapor-solid to vapor-liquid interface is increased over that of a plain wall and growing bubbles are more likely to reach a critical diameter and detach from the wall. In many studies, Kou and Peles showed the introduction of nucleation cavities etched vertically into the wall to increased critical heat flux increased the two-phase heat transfer coefficient and reduced instability [21, 51]. These studies combine a large reentrant cavity (ϕ = 50 μm) that provides area for a bubble to grow, with a small mouth ($w = 7.5$ μm) that allows a bubble to enter the bulk flow.

The 2006 study by Kuo and Peles examined test sections that contained interconnections between the nucleation cavities as shown in Figure 2.9. As this was the only test section studied, the effect of the reentrant cavities could not be determined. However, some observations relevant to this study were made. First, as mass flux increased, the vapor quality threshold for bubble nucleate dominated heat transfer decreased. Next, bubble departure frequency increased with heat flux. Tied to this, as heat flux increased, bubble departure diameter decreased.

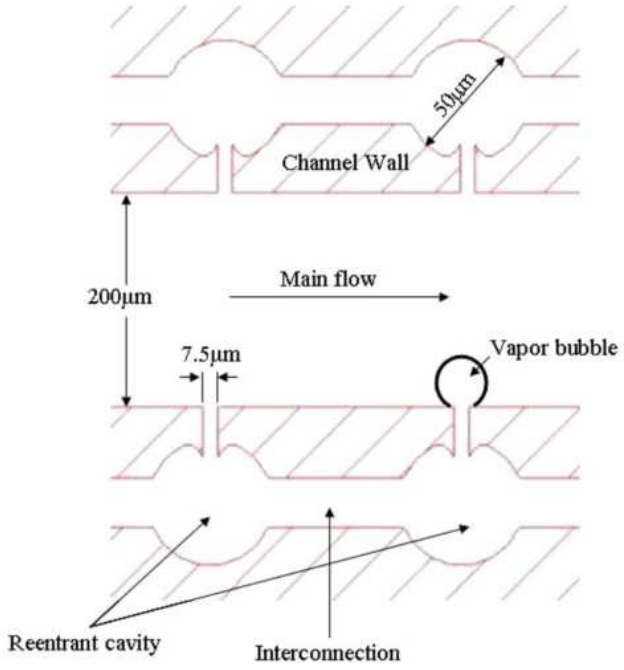

Figure 2.9: Schematic of microchannels studied by Kuo and Peles [51] in which the nucleation sites are linked.

The following year, Kuo and Peles compared similarly enhanced channels, as shown in Figure 2.10, to plane walled channels with the same dimensions [21]. The channels shown here are viewed isometrically, with the tops of the channel walls shown in white and the floor in dark gray. Reentrant cavities are etched vertically down the channel walls and are connected to the fluid by small passages. The microchannels with artificial nucleation sites showed better nucleation site distribution. This led to lower wall superheat required to initiate boiling as well as larger heat transfer coefficients. Because bubble departure diameter was reduced and departure frequency was increased, instability and flow oscillations were suppressed and critical heat flux was enhanced.

Similarly, Li et. al. [52] compared the heat transfer performance of microchannels with and without triangular cavities etched into the vertical walls of the channels. In this study, the channels had a nominal 200 μm$\times$ 200 μm$\times$ 2 cm (width, depth, length). Each channel contained a restriction at the inlet and experiments were performed with acetone as the working fluid. Mass fluxes ranged from 93 $\mathrm{kg\,m^{-2}\,s^{-1}}$ to 442 $\mathrm{kg\,m^{-2}\,s^{-1}}$. The outlines of both channel dimensions are shown in Figure 2.11 where the plane walled channels are shown on top and the channel with tri-

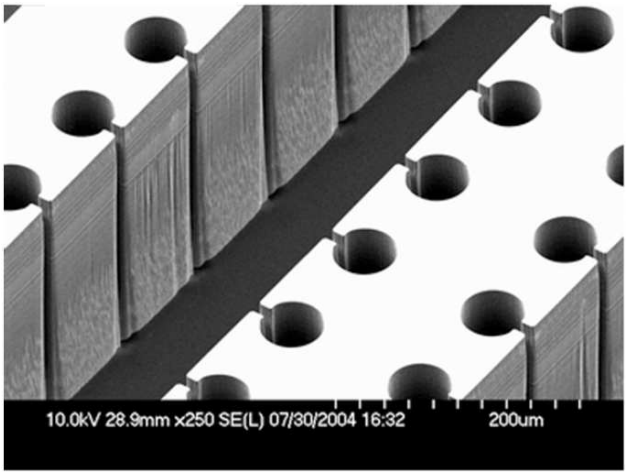

Figure 2.10: Channel wall with 50 μm reentrant cavities from Kuo and Peles [21].

angular cavities are shown below. Here, the triangular cavities have been removed from the walls, increasing the width of the channel at each cavity. The cavities are symmetrical in each channel, and staggered in adjacent channels. The enhanced wall heat sink showed heat transfer coefficients up to 9.8$\times$ higher than its plane walled counterparts. This included an increase in critical heat flux and lower wall superheat at the onset of nucleate boiling. Additionally, a reduction in pressure drop was observed in the triangular cavity microchannels which is likely a function of the larger hydraulic diameter. This was also accompanied by a reduction in flow instabilities.

2.2.4 Micropillars

In an effort to enhance heat transfer area, many authors have incorporated pin fins into microchannel devices [53–55] and shown increases in heat transfer performance, generally at the cost of an increase pressure drop. One such study from Krishnamurthy et. al. examined 100 μm diameter pin fins centered in 200 μm$\times$ 243 μm (width, depth) channels in which HFE7000 was used as the working fluid. Heat transfer performance from these devices was compared to plane microchannels of the same dimensions. Both single-phase and two-phase experiments were performed. Single-phase thermal resistance in the pin fin heat exchangers was significantly reduced relative to the plane walled channels, from 19.6 $\mathrm{K\,W^{-1}}$ to 11.8 $\mathrm{K\,W^{-1}}$. This performance increase was attributed to the increase in heat transfer area and increased mixing. The two-phase thermal

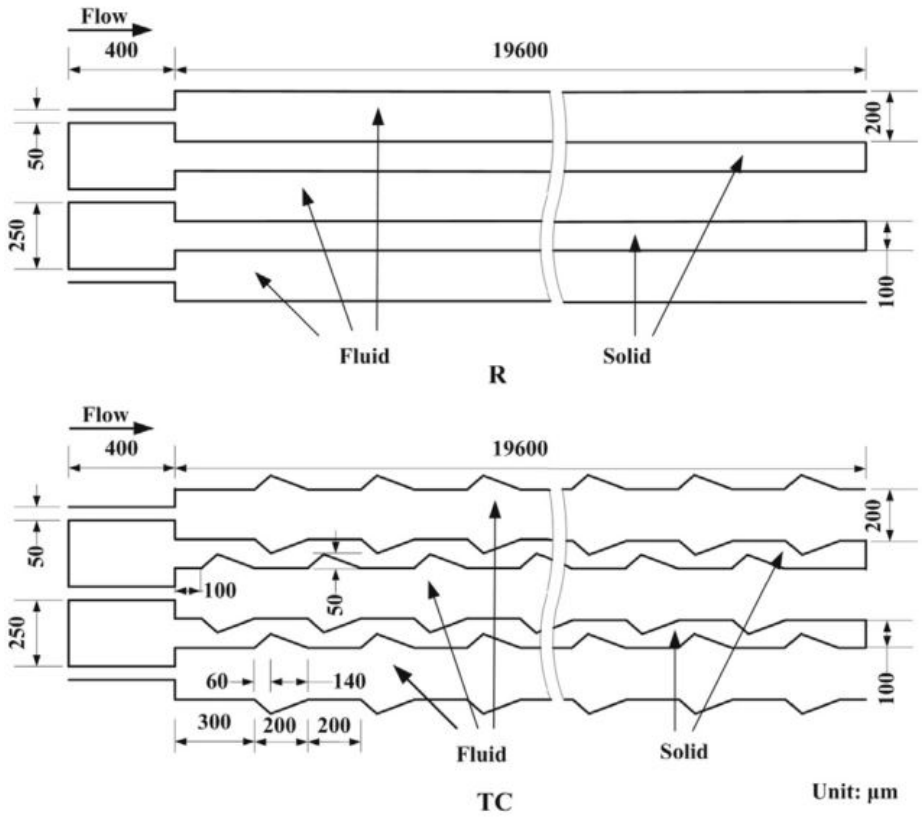

Figure 2.11: Schematic of plane walled (P) and triangular cavity (TC) microchannels from Li et. al. [52]

resistance was also lower in the pin fin heat exchangers when compared to the plain channels. However, the improvement was smaller in comparison to the single-phase test. The authors attribute this to a decreased fin efficiency with higher heat transfer coefficients. Flow visualization was performed and can be seen in Figure 2.12 where bubbly flow, slug flow, and annular flow are shown in Figure 2.12(a), 2.12(b) and 2.12(c) respectively. In the bubbly flow regime, at low heat fluxes, the bubbles nucleated and did not coalesce. As heat flux was increased, the bubbles began to interact after nucleating, causing larger bubbles in the bulk flow. However, these bubbles were still smaller than the pin diameter. In the next flow regime, these large bubbles further coalesced into slugs, which were intermittently sheared by the pins. Finally, in annular flow, vapor traveled along the center of the channel, with a liquid core along the channel walls. In this regime, bubble nucleation is suppressed.

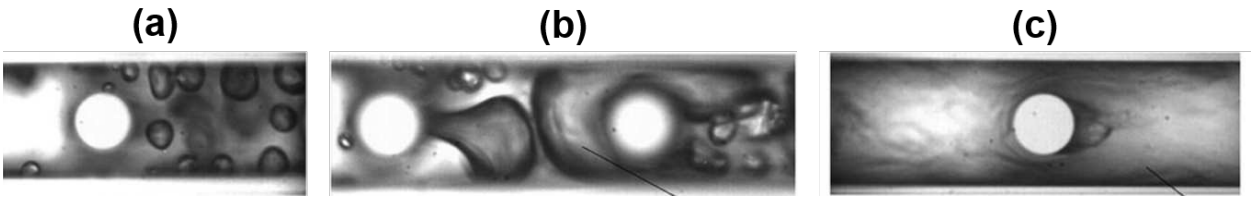

Figure 2.12: Micro pin fin flow regimes from Krishnamurthy et. al. [53] showing bubbly flow (a), slug flow (b) and annular flow (c)

2.2.5 Vapor Extraction

As critical heat flux decreases with thermodynamic vapor quality, there are obvious improvements to be gained by keeping vapor quality low. One method for achieving this is presented by Yu et. al. [56–58] in which vapor is extracted along the length of the channel as it is created. This is achieved through piranha pin fins which capture vapor as it is created upstream and channel it to a separate, unheated passage. Twelve devices were studied with varying geometries ranging from a plain mircochannel to a solid pin fin array. Piranha pin fins with varying numbers of pin inlets and reentrant cavities were investigated. Two packing densities were investigated and the pin fin geometry was dependent on the density. The high density fins have a nominal diameter of 150 μm and were 300 μm long. The larger, low density fins have a nominal diameter of 200 μm and were 400 μm long. All pin fins were created within a 2.4 mm wide 213 μm deep microchannel. An SEM image of the 150 μm diameter piranha pin fins are shown in Figure 2.13 with 1 opening and 3 reentrant cavities. All experiments were performed with HFE7000.

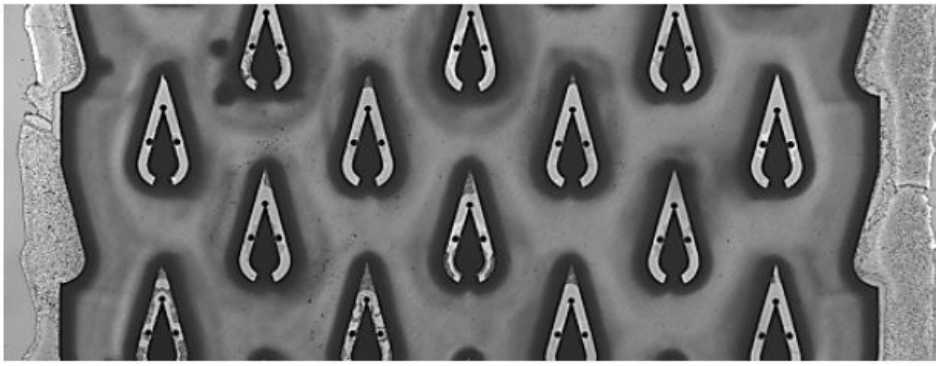

Figure 2.13: Microscope image of piranha pin fin array from Woodcock et. al. [56].

Yu et. al. found that pin fins with narrower openings achieved higher critical heat fluxes, likely because pressure drop and resulting instabilities were lower. Interestingly, convective heat transfer was found to be the dominant regime as heat transfer coefficients were found to be strongly dependent on mass flux and only very weakly dependent on heat flux.

2.3 Research Needs for Enhancement of Two-Phase Mircochannel Heat Exchangers

A review of the literature presents the physics of microchannel flow boiling and the behaviors that prevent the widespread use of this technology for the thermal management of high power laser diodes. Several methods of enhancing the performance and suppressing undesirable behaviors are also presented. Although two-phase microchannel heat exchangers offer several advantages, e.g. reduced flow rates and thermal resistance, several behaviors prevent their widespread use for high heat flux electronics. The high heat transfer coefficients present in two-phase flow, combined with the small hydraulic diameters of the channels, can cause bubbles to form explosively and expand in the upstream direction. This causes flow oscillations and non-uniform flow between channels. Both of these can lead to premature dryout. The temperature spikes associated with dryout will damage laser diode bars. Even with instabilities suppressed, dryout can still occur at high vapor qualities and heat fluxes. Several studies have shown that texturing of the channel walls with reentrant or triangular cavities increases critical heat flux and reduces flow instabilities. Inlet restrictions also reduce flow instabilities. However, none of the above studies cover channel diameters below 100 $\mu\mathrm{m}$. Table 2.1 lists the method of enhancement, hydraulic diameter, working fluid, and reduced pressure for the studies enumerated above.

Recently, a two-phase heat exchanger that contained an array of 125 parallel 45 $\mu\mathrm{m}\times$ 200 $\mu\mathrm{m}$ (width, height) channels was presented that used R134a as the working fluid and dissipated heat loads up to 1.1 $\mathrm{kW\,cm^{-2}}$. Using these small diameter channels, low thermal resistance goals were met [2]. Bevis et. al. demonstrated that 5 mm long channels centered over the heater could dissipate up to 1.1 $\mathrm{kW\,cm^{-2}}$ while maintaining the heater at 60°C. This value approached

Table 2.1: Comparison of flow boiling enhancement studies.

Researcher	Method	D_{h} [μm]	Working Fluid	P_{R}
Khanikar	CNT	715	Water	5.1×10^{-3}
Pranoto	CNT	1.12×10^{5}	Water	4.6×10^{-3}
Kuo and Peles	Cavities	227	Water	4.6×10^{-3}
Li	Cavities	200	Acetone	2.2×10^{-2}
Krishnamurthy	Micropillars	219	HFE7000	0.10

critical heat flux, but this was not studied directly. A further reduction in thermal resistance and an increase in critical heat flux within this form factor would be useful. This reveals the need for further research in the following areas:

- Featuring of channel walls in small channels ($D_{\mathrm{h}} < 200\mu\mathrm{m}$)
- Flow boiling enhancement with high pressure refrigerant
- Computational model that explains the behavior of heat exchangers with enhancement

2.4 Specific Aims of Present Study

The literature review shows a lack of studies that investigate flow boiling enhancement in small diameter channels with a high pressure refrigerant used as the working fluid. This study aims to fill this gap with four specific goals:

- Compare the thermal resistance of 2 area enhancement patterns to plane walled channels.
- Compare the critical heat flux of these area enhanced heat exchangers to plane walled channels.
- Use a computational model to explain the performance of each heat exchanger design.
- Expand the computational model to predict the performance of alternate geometries and make a recommendation for the optimal enhancement pattern.

Completion of these goals will improve the performance of two-phase microchannel heat exchangers and expand their usability. With more reliable heat exchangers, laser diodes can be run more efficiently and at higher powers.

Chapter 3: Experimental Setup

Custom test sections were fabricated to achieve the goals of this study. Three test section designs, one plane walled and two with area enhancement, are used in this study and their construction and design is described in section 3.1.1 and 3.1.2, respectively. To characterize the performance of each test section, a custom fluid loop is used. Design and operation of this facility is described in section 3.2.

3.1 Test Section Description

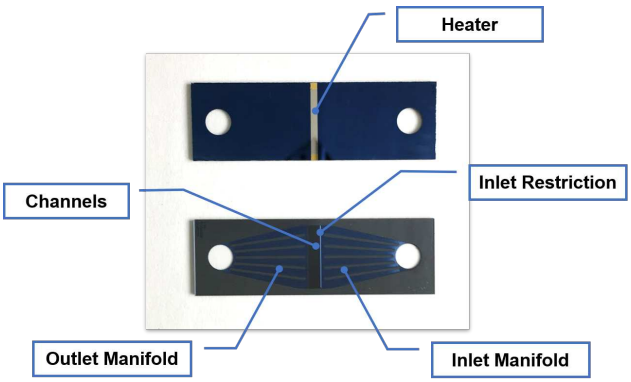

Figure 3.1: Front and back of test section. Shows location of heater, inlet and outlet ports, channel array and inlet restrictions.

The microchannel test sections, which were fabricated at Lawrence Livermore National Lab, are shown in Figure 3.1. The test section contains 125 parallel microchannels etched into a silicon wafer and sealed with clear, borosilicate glass. As shown in Figure 3.1, fluid enters from the right and is distributed across the channel array by 5 support ribs. Before entering the channels, the fluid passes through a narrow inlet restriction to promote even flow distribution and reduce backflow, as described in the section 2.2.1. The fluid then exits the channels and is guided to the outlet.

To simulate the heat load of a diode bar, heat is added through a thin film heater deposited on the backside of the test piece in the center of the channels. This resistive platinum heater has the same footprint as a typical laser diode: 10 mm long and 1 mm wide. The platinum is deposited 610 nm thick to provide a resistance of 8.5 Ω.

The precise manufacturing required to fabricate these small features requires microelectromechanical system (MEMS) manufacturing techniques. These processes will be discussed in the following section.

3.1.1 Test Section Fabrication

The tests pieces are etched into 500 μm thick silicon wafers. 8 test sections can be etched into a single 100 mm diameter wafer at once. This section describes the MEMS processing techniques that are used to fabricate the test sections. A brief overview of the fabrication process will be provided in this paragraph, and then more details about each step will be provided in the following paragraphs. The steps to produce a test section are as follows: 1) clean and prepare silicon wafers, 2) mask sections of the wafer that will be protected from etching, 3) etch areas that are not covered by mask, 4) bond borosilicate glass cap to wafers, 5) deposit thin film heater onto wafers, and 6) dice wafer into individual test sections. A brief summary of these steps is presented here. An in depth of description of the process can be found from Bevis e.t al. [2].

First, the silicon wafers and glass are exposed to the RCA cleaning regimen to prepare silicon wafers for high temperature processing steps by removing organic contaminants and particles. The wafers are bathed in a mixture of deionized water, ammonia and hydrogen peroxide at elevated temperatures, typically 80°C [59]. While this step removes particulate mater from the surface, it also leaves a thin (10 Å) silicon dioxide layer on the wafer surface. Additionally, a small degree of metallic contamination takes place. Next, the wafers are dipped in aqueous hydrofluoric acid at 25°C for 15 seconds to remove the oxide layer. Finally, the wafers are dipped in a solution of deionized water, aqueous hydrochloric acid and hydrogen peroxide to strip away the metallic contaminates. This step also produces a thin passivization layer that protects the surface from further contamination.

After the RCA clean, the wafers are ready for the etching process. The parts are etched twice: first to create the channel features and manifolds, and then again to create the inlet and outlet through-holes. A mask is used to protect sections of the wafer that are not to be etched. The mask is made of a photo-resist polymer that is coated onto the entire surface of the wafer, parts of which

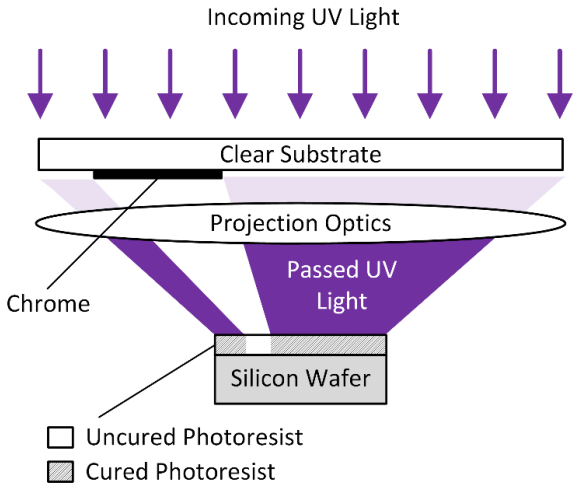

Figure 3.2: Selective curing of photo-resist polymer with UV light [2]

are cured using UV light. Figure 3.2 shows the UV light passing through the clear substrate which has chrome deposited on the surface to selectively block the light. Because the chrome image is 5 to 10$\times$ larger that the final product, the UV light is focused through the projection optics and onto the surface of the photo-resist. Finally, the uncured photo-resist polymer is removed, and the surface of the silicon wafer is exposed for the etching process.

The steps in the Deep Reactive Ion Etch (DRIE) process used to produce the test pieces are shown in Figure 3.3. The alternation between etching processes and surface passivization allows the creation of etched features with high aspect ratios. This yields a high surface area to volume ratio for the test sections. The steps in this process are described in this paragraph. First, as discussed above and shown in Figure 3.3(a), the photo-resist polymer mask is selectively cured and the uncured mask is removed. Next, shown in Figure 3.3(b), the unmasked area is exposed to etchant, a low pressure sulfur hexafluoride (SF_6) that is excited to a plasma state and directed in a beam towards the wafer surface. This removes silicon by ionizing particles on the surface of the silicon so that they can be removed by the vacuum pump. This process produces an isotropic etch; that is, material is removed normal to the exposed surface. Because of this, each etching step does not produce vertical walls, but instead undercuts slightly. However, because the SF_6 ions are being directing at the wafer, the etch is biased in the direction of the floor. This also has the effect that

etch depth is affected by the amount of access the SF_6 ions have to the feature floor; that is, more restricted features are etched more slowly that open areas. After each etching step, the freshly etched walls of the part are coated in a photo-resist polymer passivization layer (C_4F_8) as shown in Figure 3.3(c), and the etch process is repeated, shown in Figure 3.3(d). Etch and passivization processes are alternated until the desired feature depth has been achieved [59].

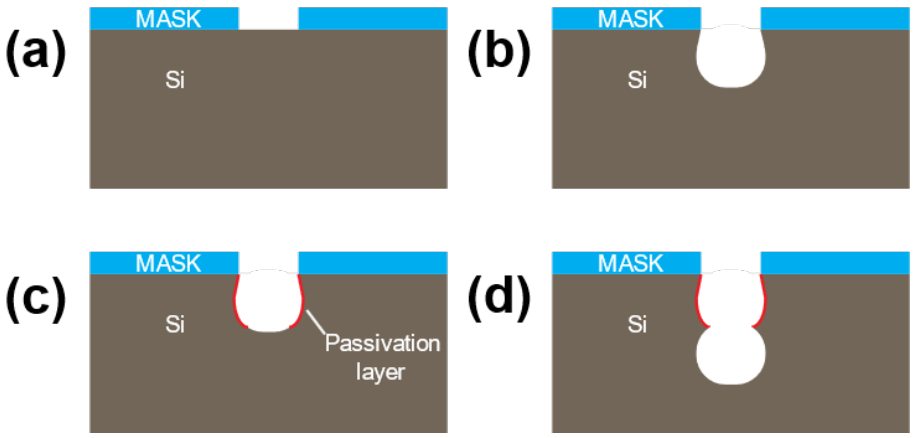

Figure 3.3: Deep Reactive Ion Etch (DRIE) process showing isotropic etching and resultant scalloping

The nature of the alternating etch and passivization processes creates an interesting scalloping pattern vertically along the channel walls. This produces a slight increase in heat transfer area as compared to straight vertical walls. This effect can be seen in Figure 3.4. The rough channel ends in this image are the result of cutting a test section for imaging and are not representative of test sections that are used in this study. The periodicity of this scalloping behavior will be combined with a vertical etch pattern into the channel walls and will be discussed in the subsequent section.

The DRIE process occurs in two discrete steps. First the flow features such as the channels, inlet restrictions and inlet and outlet manifolds are etched until the depth of the channels measures 200 μm. Next, a separate mask is applied and the inlet and outlet holes are etched through the remainder of the silicon wafer.

After etching is complete, the silicon wafers are bonded to the borosilicate glass cap to create a fluidic seal. This is done with an anodic bonding process designed for silicon and glass known

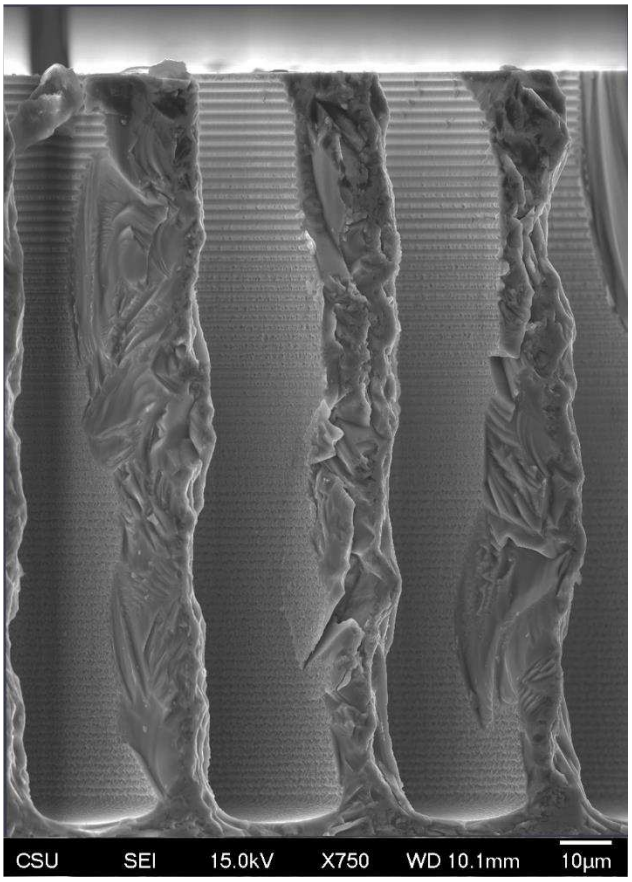

Figure 3.4: Dimetric view of channel walls showing scalloping resulting from DRIE processes.

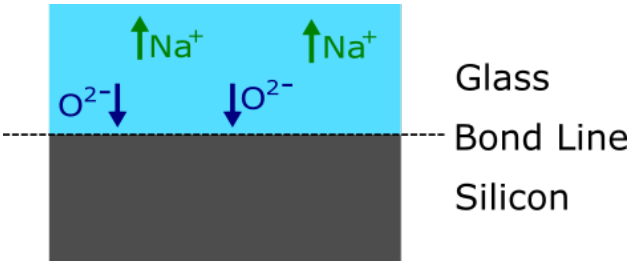

Figure 3.5: Diffusion of Na^{+} and O^{2-} ions to form bond

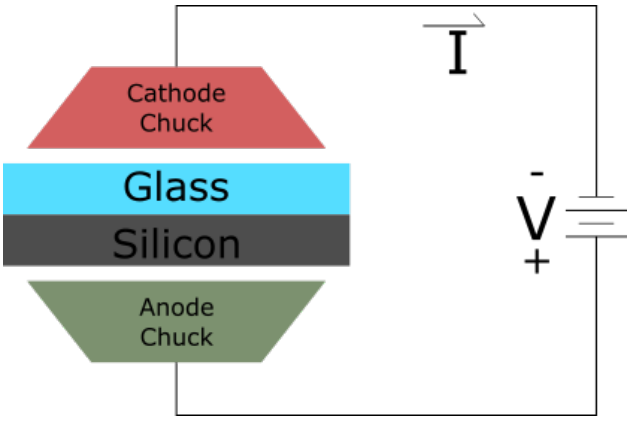

Figure 3.6: Schematic of silicon and glass wafers in bonding chucks with applied voltage

as field assisted bonding. This process creates a bond that can have a higher strength (10 MPa - 20 MPa) than the fracture strength of the glass cap. The bond is achieved by separating the glass (NaO_2) into positive sodium ions (Na^+) and negative oxygen ions (O^{2-}). The oxygen ions migrate the to the silicon-glass interface where they form a thin silicon oxide (SiO_2) layer that constitutes the bond. This process is shown in Figure 3.5. The steps in the anodic bonding process are discussed in the remainder of this paragraph. First, the wafers undergo another round of RCA clean to remove any remaining photoresist and passivization polymer. While anodic bonding is relatively tolerant of contamination, good contact between the glass and silicon is necessary for a strong bond. The clean silicon wafer and glass are then brought into mechanical contact between two bonding chucks and raised to a temperature between 200°C and 500°C, below the transition temperature of the glass. Next, a large voltage potential is applied at the bonding chucks, between 300 V and 700 V as shown in 3.6. This drives the positive sodium ions (Na^+) to the top side of the glass, away from the bond surface, and the oxygen ions (O^{2-}) towards the bond plane. Because the silicon wafer is an inert anode, no ions drift out of the material and no volume change is experienced. Conversely, the glass wafer undergoes a small volume change from the loss of the O^{2-} ions. Finally the bonded wafers are slowly returned to room temperature. Cooling time depends on the level of coefficient of thermal expansion (CTE) mismatch between the glass and silicon used. Typically the entire bond process lasts between 5 minutes and 20 minutes [59].

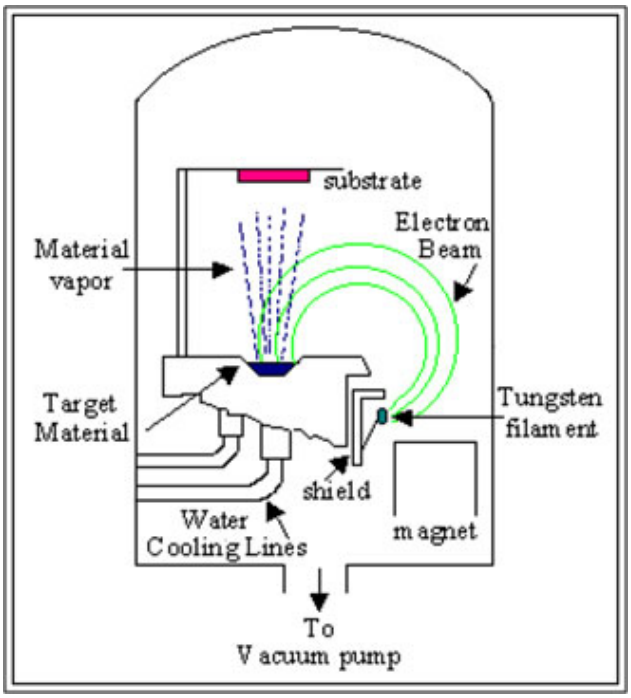

Figure 3.7: Evaporation physical metal deposition [3]

After the test pieces are bonded, the surrogate heaters are deposited on the silicon, opposite the channels. This is done through a process of physical vapor deposition (PVD), shown in Figure 3.7. Here, the metal is heated with an electron beam to the point of vaporization. This vapor is then directed toward the silicon wafer which has been partially covered in a mask. The mask used in this step is a machined direct contact mask that lies directly on the silicon surface. The heater is deposited in several layers with two distinct masks. First, to promote bonding, titanium, which bonds well to both silicon and platinum, is deposited with a footprint of 1 mm$\times$ 10 mm, 10 nm thick. Then, platinum, which constitutes the bulk of the heating element, is deposited using the same mask, this time 200 μm thick. Then, the copper contact pads are deposited with a second mask at either end of the heater, again sandwiched in titanium to promote adhesion and nickle to prevent corrosion [59]. Finally, the wafers are ready to be diced into individual parts on a diamond saw.

3.1.2 Test Piece Feature Details

This section describes, in detail, the test piece layout and values for all feature sizes. Each test piece measures 12 mm wide$\times$ 38 mm long and is 1 mm thick. For this study, based on prior work, the channel length has been reduced from the 5 mm demonstrated by Bevis et. al. to 2 mm [2, 15]. Each channel is 40 μm wide and separated by 40 μm thick fins. At the inlet to each channel there is a flow restriction as described by Kos et. al. This restriction is 15 μm wide and 150 μm long. A solid model cutaway of the channels, including the inlet restriction can be seen in Figure 3.8 with the flow direction indicated.

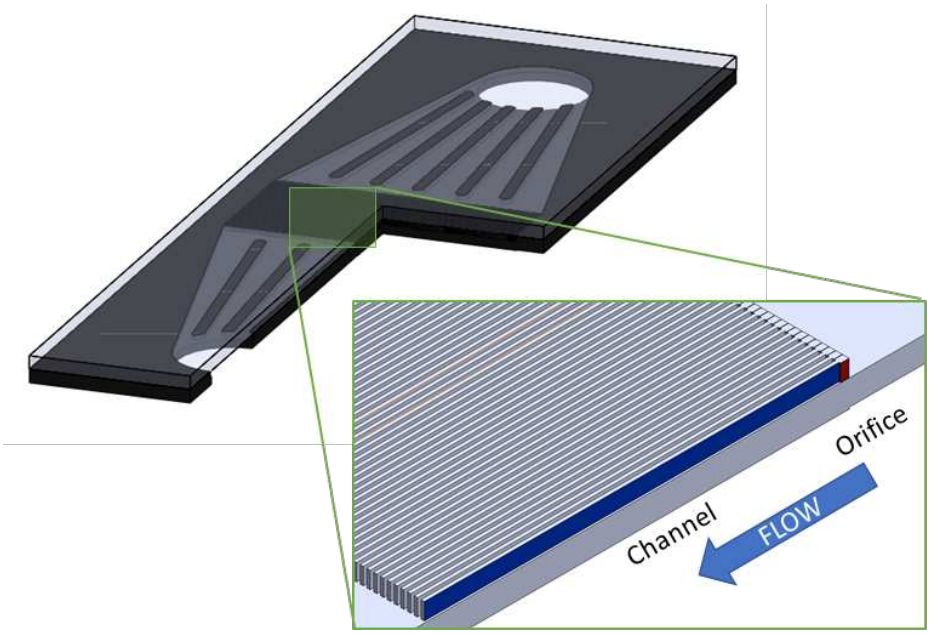

Figure 3.8: Cutaway of test section showing channel wall in blue and inlet restriction in red.

These features are shown in further depth in Figure 3.9. It should be noted that because of the etch effects discussed in 3.1.1, the channels were etched more quickly than the more restrictive orifice and therefore have different depths. Table 3.1 lists targeted feature size.

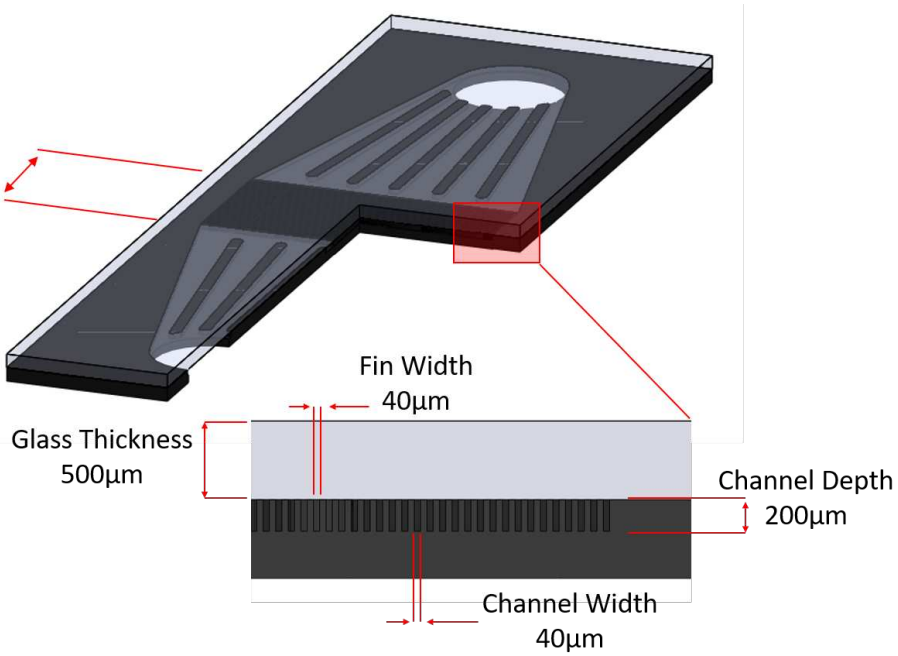

Figure 3.9: Cutaway of test section channels showing dimensions of channels, fins, glass cap and floor thickness.

Table 3.1: Test section feature size, targeted and measured.

Feature	Design Size $[\mu m]$
Orifice Width	15
Orifice Length	150
Orifice Depth	200
Channel Length	2000
Channel Depth	200
Channel Width	40
Fin Width	40

3.1.3 Pyramid Pattern

The focus of the present study is to test the efficacy of heat transfer enhancement through a patterning scheme on the vertical walls of a silicon microchannel heat exchanger. A 45° sawtooth pattern was chosen because it is a simple way to increase heat transfer area on the channel walls. Many patterns are available that would further increase area such as a larger angle or curved walls. These patterns may be investigated in a further study, but this pattern offers a good starting point. To measure the effect of the enhancement, unaltered microchannel heat exchangers will be compared to two heat exchanger designs that have been etched to produce a sawtooth pattern along the walls, which, when combined with the scalloping effect described in 3.1.1, creates a pyramid structure. The two enhanced test section designs differ in the periodicity of the sawtooth pattern. The first, from here on called the 3μm design, has a feature height of 3μm and a peak to peak distance of 6μm. The second design, the 6μm design, doubles the feature height to 6μm and the peak to peak distance to 12μm. The dimensions of these features are shown for the 3μm design in Figure 3.10. These feature sizes are exactly doubled for the 6μm part.

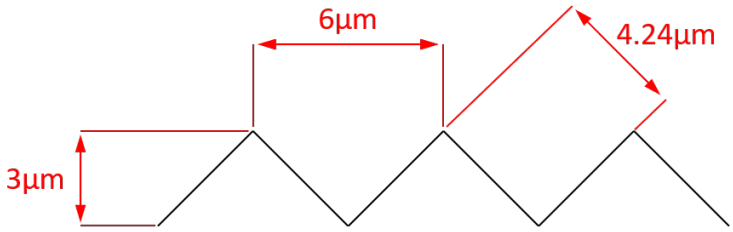

Figure 3.10: Dimension of 3 μm sawtooth design extruded vertically into channel walls. All feature sizes are doubled for the 6 μm design

An SEM image of the channel walls can be seen in Figure 3.11. One final note is the superposition of the area enhancement pattern over the plane walled design. The sawtooth pattern is designed so that the average channel diameter remains the same so the unaltered wall would run through the center of each sawtooth feature. The patterns are shown from above for comparison in Figure 3.12.

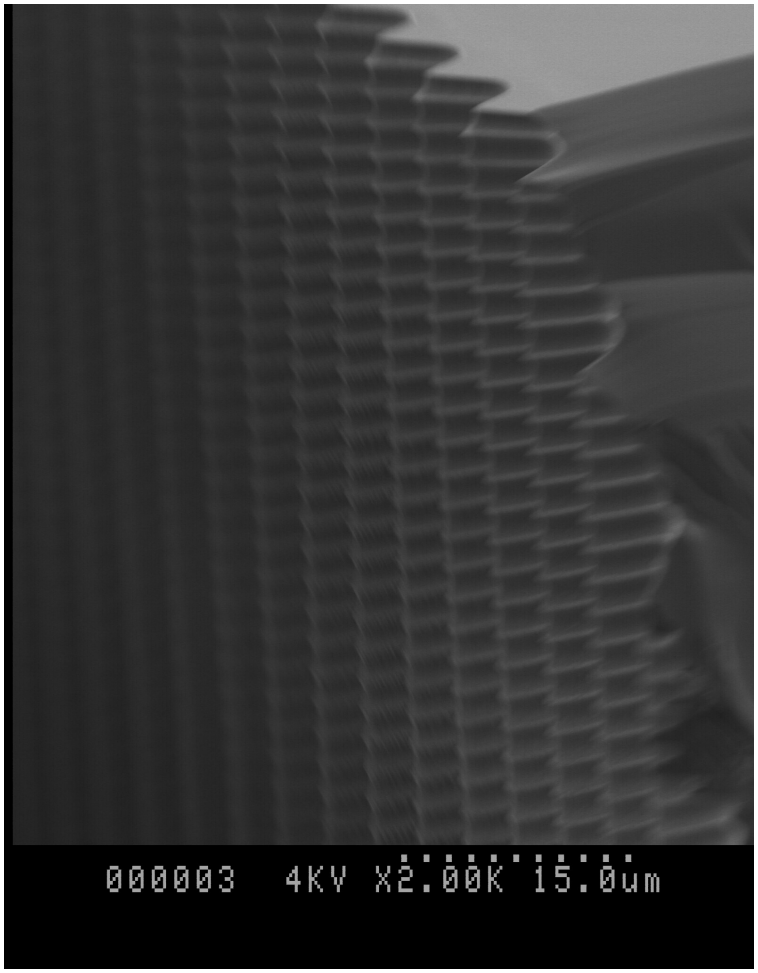

Figure 3.11: SEM image of the channel wall of a pyramid part. The 3 μm design is shown.

3.2 Test Facility Description

3.2.1 Fluid Loop Control and Measurement

A custom test facility, shown in Figure 3.13 was designed and manufactured, along with data acquisition software, to precisely control and measure fluid properties through the test section described above. The facility was designed so that test sections with varying geometries could be used interchangeably without affecting the measurement devices. As shown in the flow diagram in Figure 3.14, the working fluid, R134a, is driven through the fluid loop by a positive displacement gear pump (Cole-Parmer GA-T32) that is magnetically coupled to a variable speed drive (Cole-Parmer wu-75211-10). Mass flow is set by adjusting the speed of the drive and is measured with a Coriolis

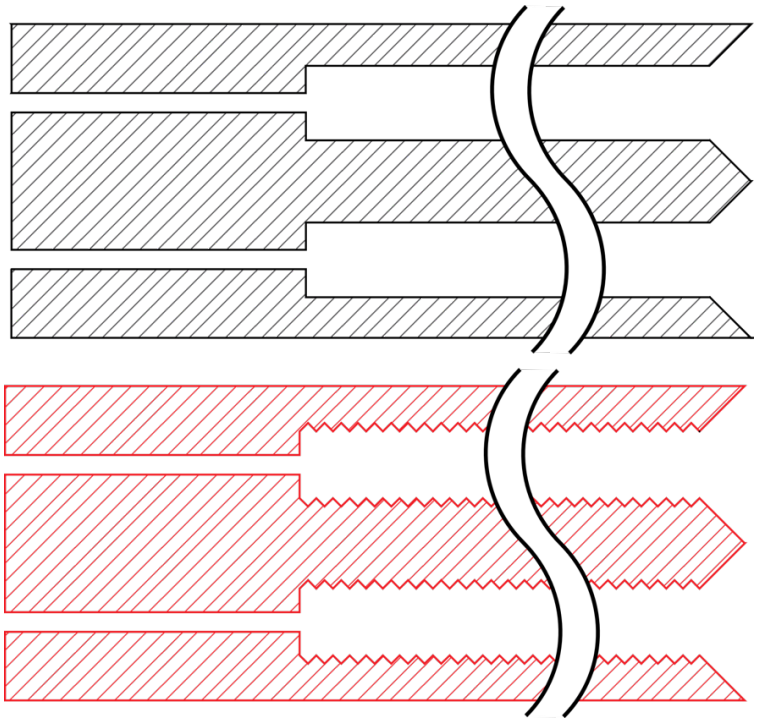

Figure 3.12: Comparison of the sawtooth pattern (red) to the plane walled pattern (black). The sawtooth pattern is drawn so that the average channel width is constant

mass flow meter (Rheonik RHM015) that is placed between the gear pump and test section. Fluid pressure is controlled by a compressed gas driven hydraulic accumulator (Humbolt HM-415A) that tees into the fluid loop downstream of the gear pump. Absolute fluid pressure is measured directly upstream and downstream of the test section (Omega PX409-100DWUI), and differential pressure across the test section is measured at the same locations (Omega MMA100C1P2CF0T4A6). Temperature is controlled with a secondary ethylene-glycol loop that is connected to a chiller (Thermofisher M150LR-CP55) that couples with the primary fluid loop through 2 compact plate heat exchangers (Koolance HXP-193). Inlet temperature is controlled by setting the temperature of the ethylene-glycol coolant and adjusting a needle valve in the secondary coolant loop that controls the portion of coolant from the chiller that flows to each heat exchanger. The heat exchanger downstream of the test section ensures that fluid entering the gear pump is fully condensed and the heat exchanger upstream of the test section is used to set the fluid temperature entering the test section. Fluid temperature is measured at several points along the fluid loop, notably, directly upstream and downstream of the test section using pipe process type-K thermocouples (Omega TC-K-NPT-UG-

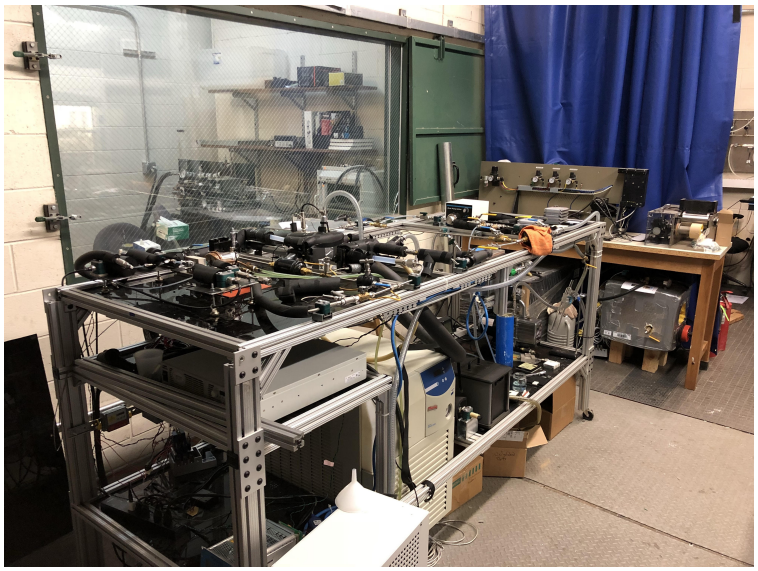

Figure 3.13: Image of custom designed heat transfer test facility. The test section interface is closest to the viewer and the gear pump lies at the back.

72). Additionally, several measurements of the ambient condition are made to characterize heat lost to the surroundings, notably the test section interface manifold temperature and the ambient temperature and pressure. Parasitic heat loss to the environment is quantified in Section E.

Input power to the test section is provided by a variable power supply (Insek SPS-606). To calculate the input power, the applied voltage is measured across the test section and a current is calculated from the voltage drop across a high precision, 0.1 Ω, shunt resistor (Ohm Labs CS-10). A full list of the equipment used in the construction of the test facility can be found in appendix A.

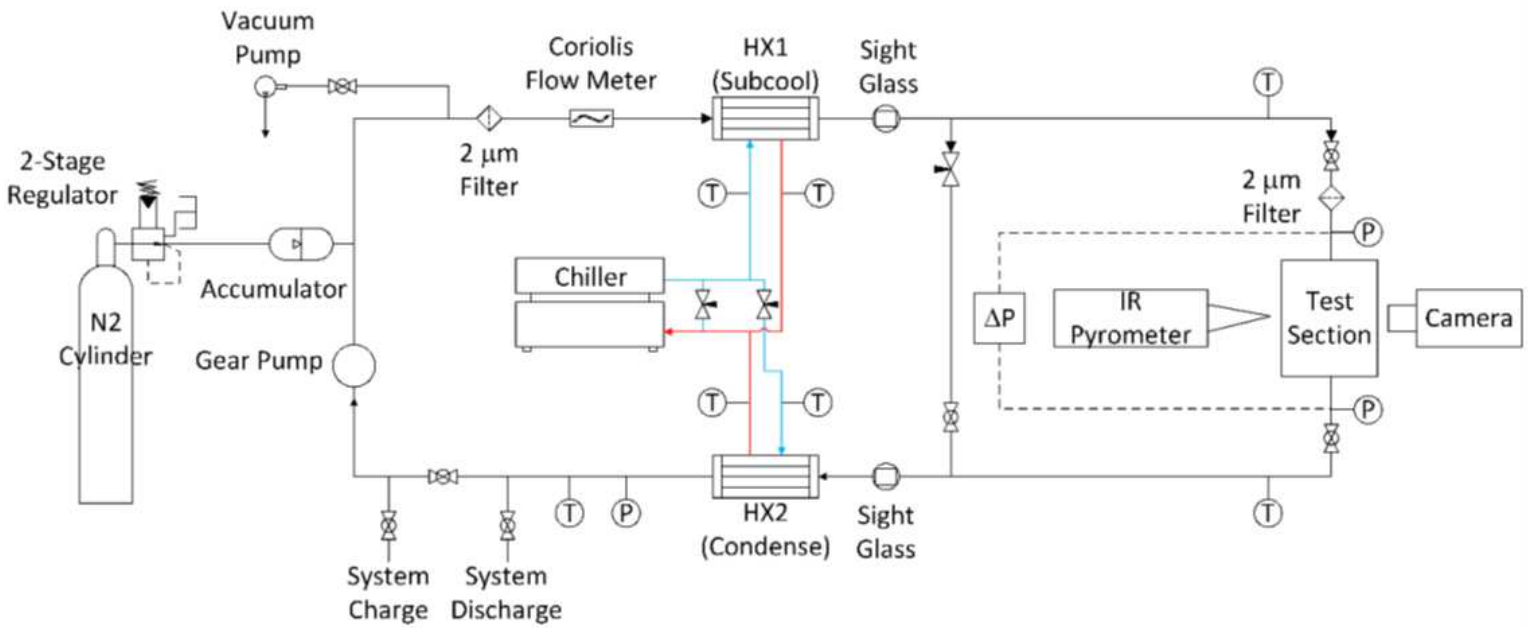

Figure 3.14: A flow diagram of the custom heat transfer test facility showing the location of the fluid property measurements relative to the test section.

3.2.2 Test Section Surface Temperature Measurement

To characterize the efficacy of the microchannel heat exchangers, a temperature profile on the backside of the heat exchanger is measured using an infrared pyrometer (MicroEpsilon CTL-CF1-C8) on a two-axis stage. This profile will also allow comparison to the analytical mode. Because of the high heat loads being applied to the test sections, the temperature profile within the silicon changes rapidly with location. For this reason, as well as the spacial constraints, a high fidelity temperature profile cannot be obtained from thermocouples. Additionally, the pyrometer allows rapid test section changes without removing and reattaching thermocouples. To increase the emissivity of the test sections, the backside, upstream and downstream of the heater, is coated in high temperature black paint. While the pyrometer controller allows the user to define the emissivity of the surface being measured, a correction for the emissivity of the test section is applied later in the data acquisition system software. To characterize the emissivity of the test section, a painted test section was placed in a furnace along with a high accuracy standard thermistor (Fluke5642-P) and a calibration curve was generated. At this time, a sensitivity study was also performed to determine if viewing angle, distance, environmental temperature or pyrometer temperature affected the pyrometer's performance. It was found that the pyrometer was largely insensitive to these variables (variance < 0.07 $^{\circ}\mathrm{C}^2$), excluding the temperature of the pyrometer. For this reason, an additional chiller has been coupled with a copper coil heat exchanger to maintain the surface temperature of the pyrometer at a constant 20$^{\circ}\mathrm{C}$. The pyrometer on the two axis stage, along with the copper coil heat exchanger, is shown in 3.15. More information on the calibration of the pyrometer can be found in appendix B.

3.2.3 Test Section Interface

An interface manifold was designed and fabricated to allow test section installation without permanent electronic or fluidic connections. This connection was also designed to minimize thermal communication with the environment, and enable measurement and visualization of the test

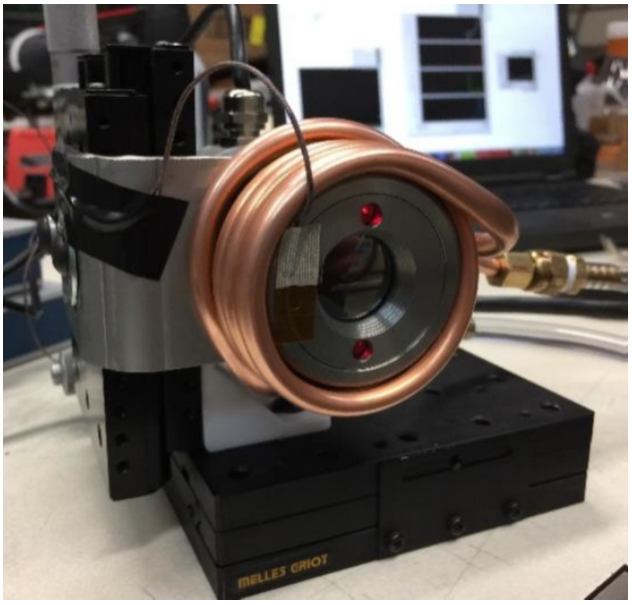

Figure 3.15: Pyrometer on 2-axis stage. Shown with a copper cooling coil that maintains a constant surface temperature.

section. This interface manifold is shown with a test piece installed and electrical harness connected in Figure 3.16.

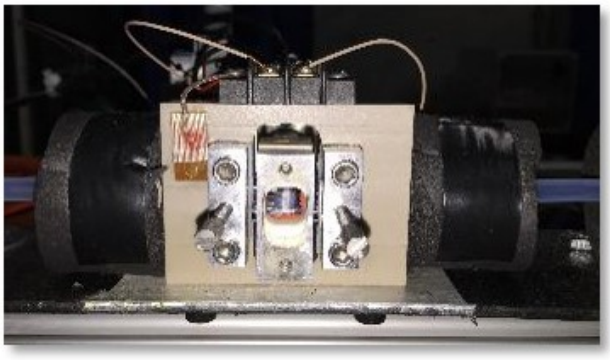

Figure 3.16: Test section shown in the PEEK interface manifold with the electrical contact harness attached.

An electrical harness was designed to make an electrical connection to the heater without requiring permanent soldering. An exploded view of this design is shown in Figure 3.17. To insulate the part and reduce thermal communication with the surroundings, the harness was manufactured from ceramic with low thermal conductivity. Finally, the electrical harness was designed to leave the microchannels on the front open for visualization and leave access for the pyrometer on the

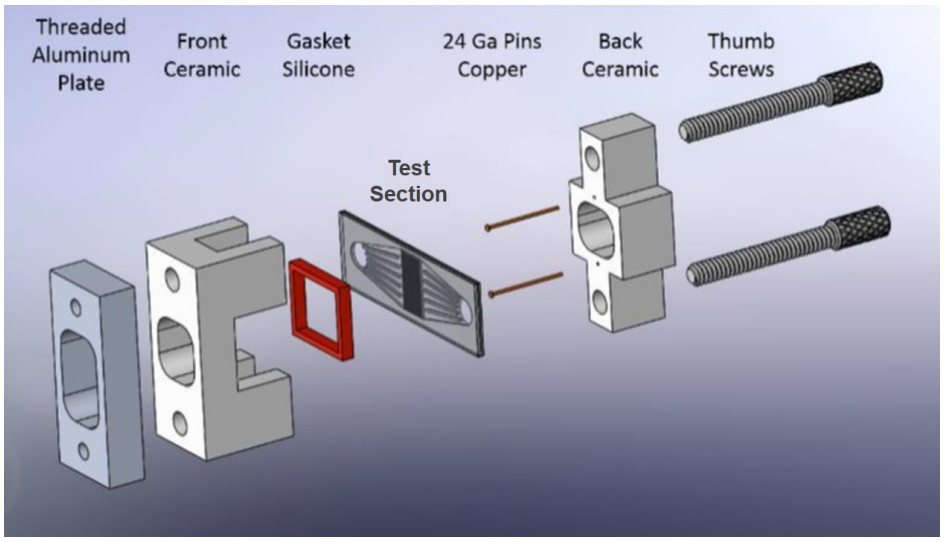

Figure 3.17: Solid model showing an exploded view of the test section being installed in the ceramic wiring harness.

back. For installation, the test section is seated in the front ceramic piece, on top of the silicone gasket. The copper pins in the back ceramic piece are aligned with the heater contact pads and brought into contact with the thumb screws.

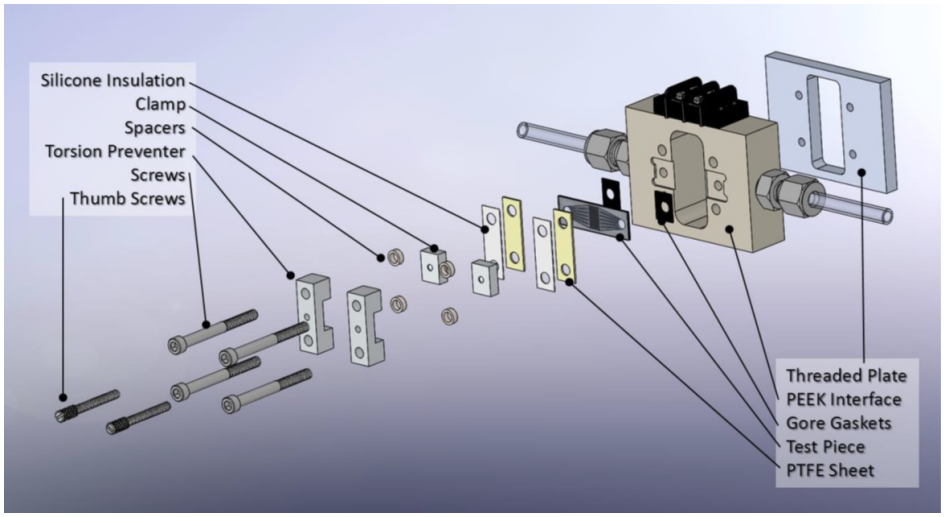

Figure 3.18: Solid model showing an exploded view of the test section being installed into the interface manifold

After the test section is installed in the electrical contact harness, it can be installed in the interface manifold. An exploded view of the test section interface assembly is shown in Figure

3.18. To create a fluidic seal, the test section is installed over Gore gaskets. Special care must be taken during installation, because silicon is very brittle and if any bending forces are applied to the test section, it may fracture. To avoid applying uneven pressure during installation, the force required to create a seal is applied by clamps that are able to rotate as they are tightened. Silicone insulation and a PTFE sheet evenly distribute the clamping force and hold the test section in place before the clamps are tightened using the thumb screws.

With the test section installed in the test facility, characterization of their heat transfer performance can begin. The methods used during testing are explained in the following section.

3.3 Test Matrix

To characterize the efficacy of heat transfer enhancement schemes, test sections with two area enhancement schemes are compared to tests sections without any additional area enhancement. To reduce the chance that differences in performance arise from differences in individual parts, an average of 3 different test sections of each geometry is presented. All inlet conditions remain constant for each test, so a direct comparison of the test section's performance can be made. These values can be seen in Table 3.2 and were chosen because they keep the max heater temperature near 60°C which is an operating condition for laser diode bars. The standard deviations for this study's tests are also listed. The test procedure is as follows. First, the inlet conditions shown in Table 3.2 are set. Then, peak diode temperature was varied over a range, starting at 40°C, and increasing in 5°C increments until critical heat flux was reached. Critical heat flux was marked when a minor increase in input power resulted in a dramatic increase in the test section temperature, accompanied with a drop in mass flow rate. At this time, a protection circuit breaks the interlock to the power supply and power is disconnected from the test section.

When results are shown from the test described above, it will be important to know if the differences seen during testing are significant. The uncertainty of each measurement is calculated as described in the following section.

Table 3.2: Testing inlet conditions, constant across each test.

Condition	Set Value	S_{x}
$\dot{m}[\mathrm{g\,min^{-1}}]]$	50	0.52
$T_{\mathrm{in}}[^{\circ}\mathrm{C}]]$	15	0.57
P_{in} [kPa]	582.6	2.69

3.4 Uncertainty

For this study, all experimental results are shown with error bars to represent uncertainty. This section briefly explains the method for determining uncertainty and summarizes the findings. A full derivation, as well as an example calculation can be found in Appendix C.

The error calculated for this study represents a 95 percent confidence interval and, because the data shown is an average of several tests, the total uncertainty is calculated as the superpostition of bias error and random sampling error. The formula for total measurement uncertainty U is presented in equation 3.1 where B is the total bias error and P is the total random error.

$$U = \sqrt{B^2 + P^2} \tag{3.1}$$

Several of the experimental values presented in this work are measured directly. For example, fluid pressure in the system is measured using pressure transducers. In this case, total uncertainty is simply the error of the sensor combined with the spread observed between trials. In other cases, such as dissipated power, the value cannot be measured directly and must be derived from multiple measured values. In this case, the uncertainty of each measurement must be taken into account.

The maximum and average calculated values of uncertainty of uncertainty that are shown graphically later in this work are presented in table 3.3.

To understand the behavior of the test sections described above, a computational model is necessary. This model is described in detail in the following section.

Table 3.3: Maximum and average calculated uncertainties for measured values shown graphically

Variable	$U_{\max}$	$U_{\mathrm{a}}vg$
$P[W]$	2.3	1.0
$T_{\mathrm{surf}}[^{\circ}\mathrm{C}]]$	0.74	0.68
ΔP [kPa]	5.38	2.48

Chapter 4: Thermal FEA Model

The data collected as described in the previous section will allow a direct performance comparison between the parts. However, to draw conclusions about the mechanism through which an improvement is observed, more information is necessary. The behavior of the plain walled and enhanced area components will be modeled to understand heat transfer in the part as well as local heat transfer coefficients and fluid properties within the channel. A thermal FEA model used due to the interdependence of the heat transfer and fluid properties within the part and is described in detail in the following section.

4.1 Computational Model

Numerical models that simulate bubble dynamics in two-phase flow are computationally expensive and the required computational power to solve microchannel flow is not widely available. For this reason, the conjugate FEA model as described by Burk et. al. [15] is used in this study to determine heat spreading, local heat flux and local heat transfer coefficients. This is done by coupling COMSOL Multiphysics with MATLAB. COMSOL makes several calculations which must be solved iteratively because they are interdependent. Local heat transfer coefficients are calculated using correlations. A fluid temperature profile is found by combining heat transfer data with a fluid pressure profile. A temperature map of the silicon part is generated and heat fluxes are calculated. Once a solution has been found, the data is exported to MATLAB which is used to calculated the fluid pressure profile. This profile is written to a data file that can be read by COMSOL on the next iteration. The following sections detail the development of this model including the definition of the solid geometry, application of boundary conditions, calculation of the fluid profile and calculation of heat transfer coefficients.

4.1.1 Geometry

Measurements laterally across the test section heater taken during the experiments show similar performance between channels ($\pm$ 0.3°C). Therefore, the modeling domain can be reduced to a half channel. To avoid the computational cost associated with two-phase flow, only the solid

domain is modeled and the fluid is represented as a local heat transfer coefficient referenced to a local bulk fluid temperature. Using the plane walled parts as a reference, a survey of heat transfer coefficient correlations available in the literature is made to determine the suitability of each correlation for this application by comparing temperature profiles from the model to those collected during testing. Once a suitable correlation is identified, the model is modified mathematically to reflect the differences in the area enhanced parts. The development of the half channel geometry from the test piece is shown in Figure 4.1. Here the outline of the half channel geometry is shown in red on the bottom right. In this geometry, the inlet restriction and inlet and outlet manifolds are removed. The glass cap is modeled as an adiabatic boundary condition, which is justified in Section 4.1.2. The fluid domain, shown in light gray, is modeled as a boundary condition, and therefore removed from the domain.

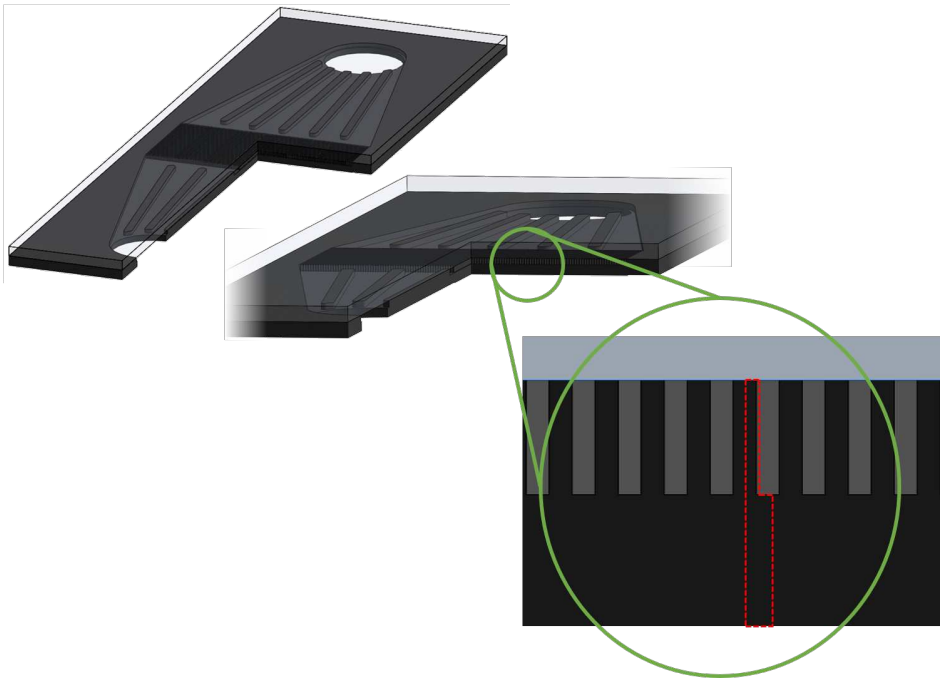

Figure 4.1: Development of the half channel geometry taken from the test section.

Extruding the outline shown in red in Figure 4.1 lengthwise along the channel creates the repeating half channel geometry. This solid domain can be seen in Figure 4.2. The bottom of

the model is divided into 3 sections with the heater section in the middle bounded by 2 adiabatic sections.

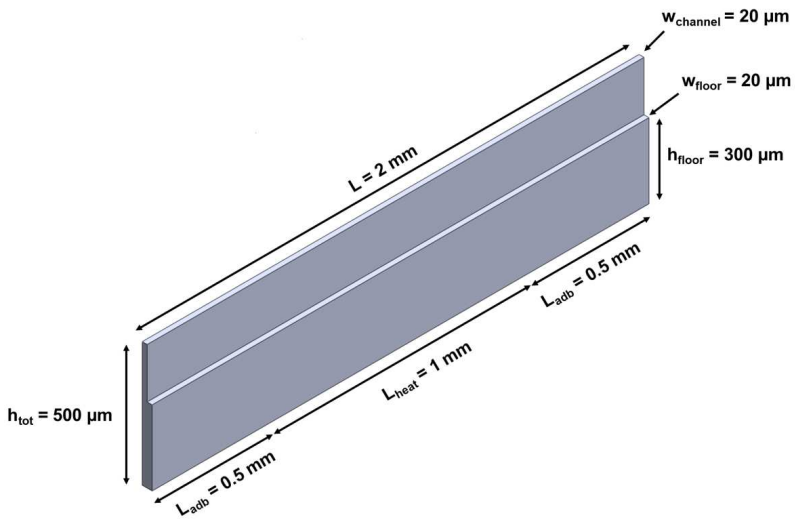

Figure 4.2: Solid domain of numerical model

4.1.2 Boundary Conditions

The half channel geometry described in section 4.1.1 is shown with boundary conditions applied in Figure 4.3. Shown in orange, a uniform heat flux condition is used to represent to the heat load from the heater. Heat flux is calculated by dividing the total heat input into the test section by two times the number of channels and then by the area of the half channel heater. A heat transfer coefficient coefficient mapped to a local fluid temperature is applied to the solid fluid interface, shown in green. A detailed discussion of the method used to determine the fluid temperature profile is given in Section 4.2.2. An explanation of the correlations used to find local heat transfer coefficients is given in Section 4.2.3. The heat transfer coefficient is calculated locally for each element and includes consideration of both single-phase and two-phase heat transfer coefficients. The remaining boundary conditions are assumed to be adiabatic. A brief justification of the adiabatic assumptions follows in the remainder of this section.

The symmetry planes, the 2 sliced vertical silicon walls, can be assumed to be adiabatic because the temperature at any point on each side of the symmetry plane will be equal so no heat is transferred across the plane. The upstream and downstream vertical walls are set to adiabatic because the area available for heat transfer in the channels is roughly 6 times larger than the prime surface area upstream and downstream of the channels. Similarly, the fin tip and the area surrounding the heater have a much higher thermal resistance than the channels. This is demonstrated by calculating the thermal resistances of each.

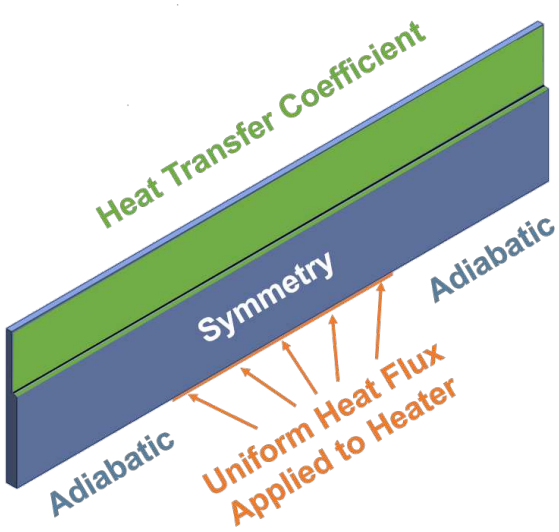

Figure 4.3: Solid domain in model with adiabatic boundary conditions shown in green

Beginning with the adiabatic fin tip condition, a resistance network is shown in Figure 4.4. This will be used to compare the relative heat flow into the working fluid with the heat lost to ambient air. Each of the thermal resistances shown is a series combination of a conduction resistance and convection resistance given by equation 4.1 through equation 4.3.

$$R_{\mathrm{th,i}} = R_{\mathrm{cond,i}} + R_{\mathrm{conv,i}} \tag{4.1}$$

$$R_{\mathrm{cond,i}} = \frac{L_{\mathrm{i}}}{k_{\mathrm{i}} \cdot A_{\mathrm{i}}} \tag{4.2}$$

$$R_{\text{conv,i}} = \frac{1}{h_{\text{i}} \cdot A_{\text{i}}} \tag{4.3}$$

Using the dimensions given above, assuming a high natural convection heater transfer coefficient of 20 $\mathrm{W\,m^{-2}K^{-1}}$, a thermal conductivity for borosilicate of 1.14 $\mathrm{W\,m^{-1}K^{-1}}$ and normalizing for area, the thermal resistance to the surrounding air is found:

$$\begin{aligned} R_{\text{cap,A}} &= \frac{500 \times 10^{-6}}{1.14 \cdot 1} + \frac{1}{20} \\ R_{\text{cap,A}} &= 0.05[\mathrm{m^2\,K\,W^{-1}}] \end{aligned} \tag{4.4}$$

Similarly, the thermal resistance to the fluid is found using a conservative estimate for h_{tp} of 1000 $\mathrm{W\,m^{-2}K^{-1}}$ and a thermal conductivity for the silicon of 130 $\mathrm{W\,m^{-1}\,K^{-1}}$. Equation 4.5 shows that the thermal resistance through the glass is 50 times larger than the thermal resistance through the fin, even assuming a low two-phase heat transfer coefficient and high natural convection coefficient. This effect is multiplied when it is considered that the fluid temperature is at least 5°C colder than the ambient air. This means that there is a larger temperature difference between the fin tip and fluid than between the fin tip and ambient air.

$$\begin{aligned} R_{\text{channel,A}} &= \frac{20 \times 10^{-6}}{130 \cdot 1} + \frac{1}{1000} \\ R_{\text{channel,A}} &= 0.001[\mathrm{m^2\,K\,W^{-1}}] \end{aligned} \tag{4.5}$$

4.1.3 Meshing

Discretizing the problem is of key importance to the computational model and because of the high temperature and heat flux gradients, a sufficiently fine mesh is required to accurately capture heat transfer behavior. However, this precision comes at the cost of computation time, which is already high. This section will first describe the construction of the mesh and then explain the method used to determine appropriate element size.

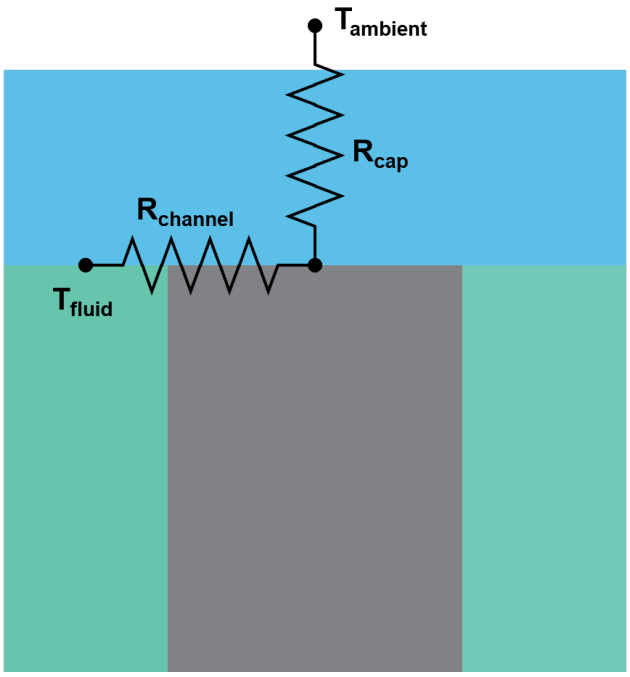

Figure 4.4: Thermal resistance diagram starting at the top center of a fin and ending in the working fluid and ambient air.

4.1.3.1 Mesh Characteristics

For this study, the rectilinear nature of the the half channel geometry lends itself well to a quad element mesh structure. To create the mesh, rectangular elements are created on the inlet face of the half channel geometry and then extruded along the fluid flow direction. Then these extrusions were subdivided along the flow direction to create the mesh elements. The mesh is divided into two regions of high and low resolution because it is supposed that the temperature and heat flux gradients directly over the heater are larger than those in the inlet and outlet region, . The area over the heater as well as 0.25 mm upstream and downstream have a finer mesh than the 0.25 mm regions at the inlet and outlet. The regions of finer mesh are shown in blue in Figure 4.5 and the face mesh extruded through the flow direction is shown to the right. Defining the mesh size this way leaves three element sizes that must be set: the length division in the high refinement region, the low refinement inlet/outlet region, and the face size on the inlet face. These sizes are determined in the following section.

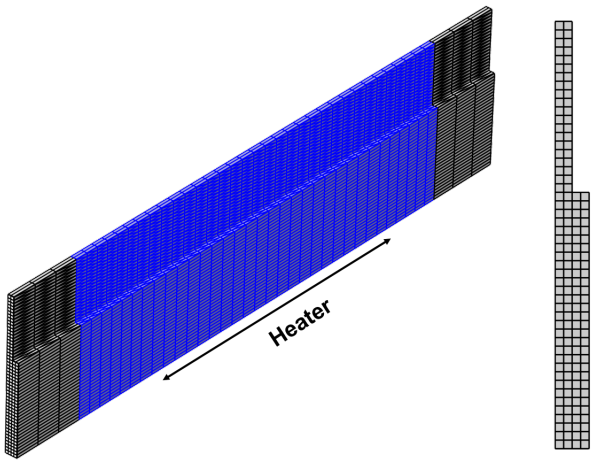

Figure 4.5: Mesh division showing the area of higher refinement in blue.

4.1.3.2 Mesh Sensitivity

The goal of the mesh sensitivity study is to reduce computation time while maintaining fidelity. Because this study is ultimately concerned with the temperature of the surrogate diode heater, average heater temperature is used as the metric to determine convergence. As mentioned above, 3 lengths must be found to fully define the mesh: element length in the high resolution region, element length in the low resolution region, and element face size on the inlet face. Each parameter is evaluated individually and then when convergence is reached, that value is used to create the mesh for the next study. This process is iterated through to find correct values. In the mesh settings, element sizes are defined as a function of model variables, in this case channel length, L_{c}, and fin width, w_{f}. For the mesh sensitivity study, element size was varied within the bounds shown in Table 4.1.

Table 4.1: Range of element sizes for mesh sensitivity study.

Element Definition	**Definition Range**	**Range [μm]**
High Resolution	$\frac{L_{\mathrm{c}}}{25} - \frac{L_{\mathrm{c}}}{46}$	80 -43.5
Low Resolution	$\frac{L_{\mathrm{c}}}{5} - \frac{L_{\mathrm{c}}}{25}$	400-80
Face	$\frac{w_{\mathrm{f}}}{2} - \frac{w_{\mathrm{f}}}{8}$	20-5

The results of this study are shown in Figure 4.6 where heater temperature is plotted against number of divisions for clarity. Here, convergence is shown by the near vertical line where an increase in the mesh resolution yielded a change of less than 0.1°C. The final element lengths used were 49 μm for the high resolution region, 100 μm for the low resolution region and 10 μm for the face sizing.

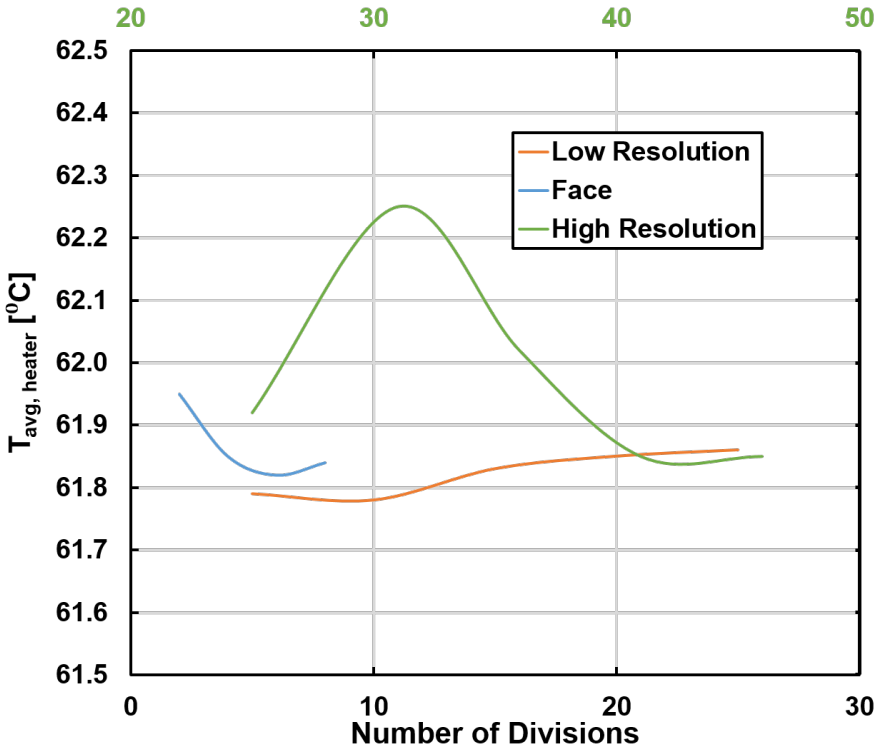

Figure 4.6: Results of mesh sensitivity study shown as a function of number of divisions of characteristic length.

4.1.4 Modification for Area Enhancement

Two characteristics distinguish the area enhanced parts from the plane walled parts. First, the area enhancement increases the contact area at the fluid-wall interface which results in a reduction in heat flux at the surface, but also increased area available for heat transfer. Because reducing the mesh element size to encapsulate individual surface features would increase the computational time, these affects are captured in local heat transfer behavior. To model the increase in available

heat transfer area, the local heat transfer coefficient is scaled by the area enhancement factor as shown in equation 4.6:

$$\begin{aligned} Q &= h \times A_{\text{enhanced}} \times \Delta T \\ &= h \times F_{\text{ae}} \times A' \times \Delta T \end{aligned} \tag{4.6}$$

where *A'* is the plane walled area, *h* is the heat transfer coefficient and F_{ae} is the area enhancement factor. F_{ae} is simply the change in area over a plane walled part.

Similarly, local heat flux is affected at the fluid wall interface by the area enhancement. This must be accounted for because it affects the rate of nucleate boiling and is accounted for as shown in equation 4.7:

$$q''_{\text{actual}} = \frac{q''_{\text{calc}}}{F_{\text{ae}}} \tag{4.7}$$

where q''_{actual} is the physical heat flux at the fluid wall interface and q''_{calc} is the heat flux calculated in the plane walled model.

Finally, surface roughness has an effect on two-phase heat transfer in that cavities on the surface wall interface act as active nucleation sites. Increasing the number of these sites reduces the wall superheat required to form vapor bubbles. The nucleate boiling term of the Bertsch correlation accounts for a larger number of nucleation sites by incorporating a peak surface roughness factor. Peak surface roughness, R_{p}, is measured in micrometers as described in ISO standard 4287. In this study, the peak surface roughness factor is 3 μm or 6 μm, corresponding the to feature height.

4.2 Model Inputs

For this study, each of the 16 data points gathered are input into the FEA model described above to evaluate the differences in performance. To assess the accuracy of the modeling approach, model inputs are entered as the data is gathered, rather than the target values. For example, the actual mass flow rate recorded in the test is used instead of the target mass flow rate, $\dot{m} = 50\text{g}\,\text{min}^{-1}$.

4.2.1 Determination of Inlet Pressure

As described in section 3.2.1, the fluid pressure is not measured directly at the channel inlet and outlet, but rather upstream and downstream of the test section interface. For this reason, local fluid pressure must be calculated before it can be transferred to the model. The method used in this study has been adapted from Burk et. al [60]. A brief explanation of this method is described in this section. A detailed list of the equations used can be found in Appendix D.

Fluid pressure at the channel inlet is determined by calculating the pressure drops across individual components between the upstream and downstream pressure transducers, as shown in Figure 4.7, using correlations.. Points 1-6 occur in piping and fittings. Between points 7 and 15, the fluid is in the machined PEEK manifold. Between 16 and 23 the fluid is the test section, with the channel inlet and outlet at 19 and 20, respectively. The machined PEEK and piping network is mirrored at the test section outlet.

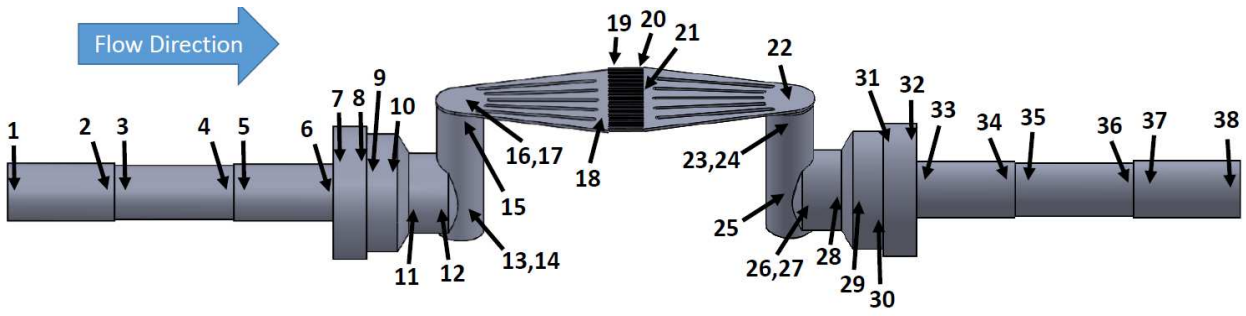

Figure 4.7: Fluid path between pressure transducers. Upstream pressure is at point 1 and downstream pressure transducer is at point 38

The nature of the DRIE manufacturing process further complicates this calculation. As described in 3.1.1, less restrictive features are etched preferentially over narrow features. In the test sections used in this study, the inlet restrictions at the mouth of each channel are much narrower than any other feature. Additionally, the middle of the orifice is less available to the etchant than the inlet and outlet. The resultant geometry is represented in Figure 4.8.The height of the orifice

floor, as well as the entrance and exit angles, cannot be determined without destructive inspection of the test sections.

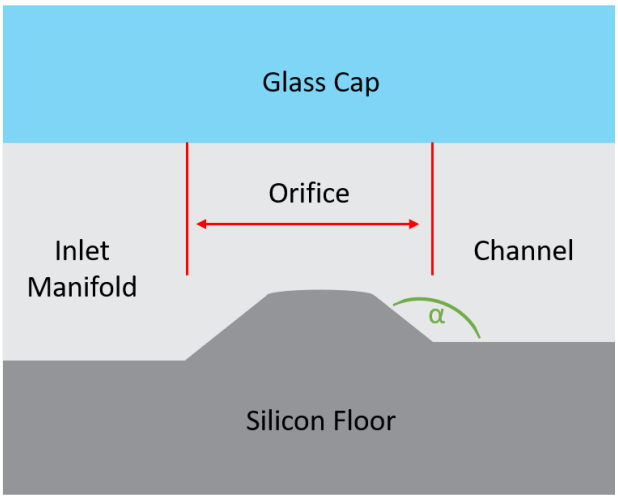

Figure 4.8: Representation of the feature size at the inlet restriction due to anisotropic etching of smaller features. The angle α and floor height in the orifice are unknown.

An example of a destructive test which was done for a different geometry with a longer channel and orifice is shown in Figure 4.9. For this test, the channel was filled with epoxy and then sliced along the midsection. Here the channel depth is 200 μm. The orifice is etched to a smaller depth and the approach angle from the inlet manifold and channel floor are not equal.

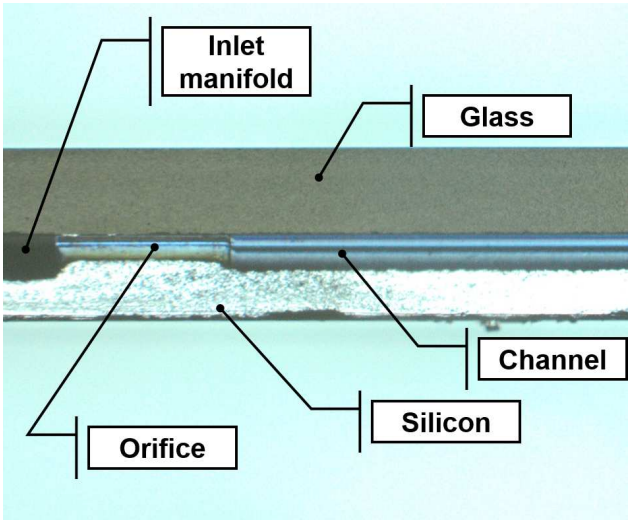

Figure 4.9: Cross section of inlet restriction achieved through destructive testing.

To overcome these limitations, the pressure drop across the orifice is calculated from single-phase pressure drop data taken at identical inlet conditions to those used during two-phase testing. This pressure drop can then be added to the other upstream pressure drops and the sum can be subtracted from the upstream pressure transducer. This is represented numerically in equation 4.8.

$$P_{\text{in,channel}} = P_1 - \sum_{\text{i}=1}^{17} \Delta P_{\text{i}} - \Delta P_{\text{orifice}} \tag{4.8}$$

The pressure drop across the orifice is described in equation 4.9 where $\Delta P_{1,38}$ is the pressure drop measured during the single-phase experiments, and $\Delta P_{1,18}$ and $\Delta P_{19,38}$ are the pressure drops upstream and downstream of the orifice that can be accounted for using standard pressure drop correlations.

$$\Delta P_{\text{orifice}} = \Delta P_{1,38} - \Delta P_{1,18} - \Delta P_{19,38} \tag{4.9}$$

Each pressure drop shown in Figure 4.7 is shown in Table 4.2 where each feature is paired with either a minor or major flow loss calculation. These are shown with a sample calculation for one of the cases, though because inlet conditions for each test match closely, the values are similar for each case.

These results are shown graphically in Figure 4.10 where both static and total pressure are shown. The plot demonstrates that dynamic pressure losses are generally small except in cases where the fluid is accelerated as is seen in the channels as well as inlet and outlet manifold. By design, pressure drop through the inlet restriction dominates the total pressure drop across the part.

With the orifice pressure calculated, the calculation to find $\sum_{\text{i}=1}^{18} \Delta P_{\text{i}}$ is repeated for each of the two-phase test cases and $\Delta P_{\text{orifice}}$ is then added back in to find $P_{\text{inlet,channel}}$. This is shown in equation 4.10.

$$P_{\text{inlet,channel}} = P_1 - \Delta P_{1,18} - \Delta P_{\text{orifice}} \tag{4.10}$$

4.2.2 Fluid Profile

The temperature profile in the channel itself depends on two factors depending on its local state. In the single-phase region, heat added to the fluid is absorbed in the form of sensible heating. In the

Table 4.2: Pressure losses by type.

Number	Description	Δ P [Pa]	Number	Description	Δ P [Pa]
1-2	Frictional Losses	0.2	19-20	Frictional Losses	1786.0
2-3	Sudden Contraction	<0.1	20-21	Sudden Expansion	86.2
3-4	Frictional Losses	0.9	21-22	Frictional Losses	300.3
4-5	Sudden Expansion	<0.1	22-23	90 ° Bend	218.8
5-6	Frictional Losses	0.2	23-24	Sudden Expansion	330.7
6-7	Sudden Expansion	0.6	24-25	Frictional Losses	0.2
7-8	Frictional Losses	<0.1	25-26	90 ° Bend	1.3
8-9	Sudden Contraction	<0.1	26-27	Sudden Expansion	0.8
9-10	Frictional Losses	<0.1	27-28	Frictional Losses	<0.1
10-11	Gradual Contraction	0.06	28-29	Gradual Contraction	<0.1
11-12	Frictional Losses	0.1	28-29	Frictional Losses	<0.1
12-13	Sudden Contraction	0.6	30-31	Sudden Expansion	<0.1
13-14	90 ° Bend	1.31	31-32	Frictional Losses	<0.1
14-15	Frictional Losses	0.20	32-33	Sudden Contraction	0.4
15-16	Sudden Contraction	167.3	33-34	Frictional Losses	0.2
16-17	90 ° Bend	218.8	34-35	Sudden Contraction	<0.1
17-18	Frictional Losses	300.3	35-36	Frictional Losses	0.9
18-19	Orifice	—	36-37	Sudden Expansion	<0.1
			37-38	Frictional Losses	0.1
$\sum_{i=1}^{18} \Delta P_i$ = 689 Pa			$\sum_{i=18}^{38} \Delta P_i$ = 2727 Pa		

two-phase region, heat is absorbed by the latent heat of vaporization, meaning that the fluid does not change temperature. However, as the two-phase mixture travels down the channel, the bulk pressure drops, both from frictional and accelerational effects. In response, the fluid temperature drops to the saturation temperature at the new bulk pressure. Therefore, two independent variables are needed to define the fluid's thermodynamic state. In the single-phase region, where these are independent, temperature and pressure can be used. In the two-phase region, where temperature and pressure are dependent on each other, a third parameter is needed. The following calculations use vapor quality. Each of the variables described below are interdependent and must be calculated using an iterative method. With the exception of those relating to the fluid pressure profile, all calculations are performed internally in COMSOL.

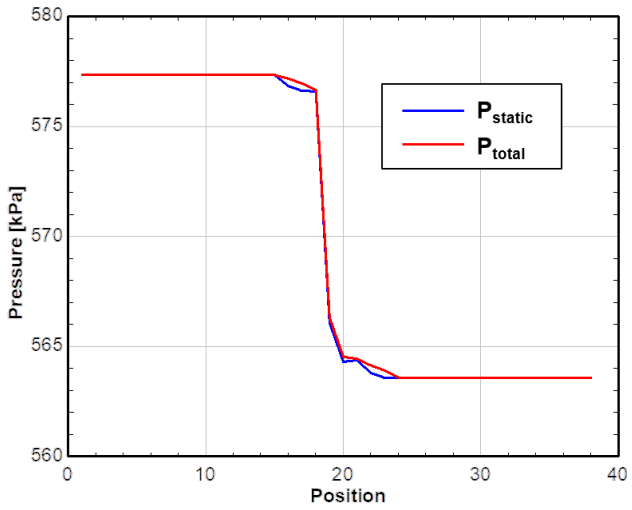

Figure 4.10: Single-phase pressure drop through test section and test section interface.

The discussion of generating the fluid profile will begin with the calculation of the pressure profile. However, this calculation assumes many values calculated in COMSOL are already known such as the transition location and the vapor quality profile in the two-phase region. In practice, a guess of the pressure profile must be made to begin the iteration process. This solution method is shown graphically in Figure 4.11. During the solution process, MATLAB performs the calculations described below and then writes the generated pressure profile to a data file that COMSOL can then interpret.

The single-phase and two-phase pressure are calculated separately. Both correlations come from Lee and Garimella [61] and were developed from data sets with channel sizes down to 160 μm. Although the channels used in this study fall outside of this range, there are no suitable correlations for smaller channels. The formula for single-phase pressure drop is shown in equation 4.11:

$$\Delta P_{\mathrm{sp}} = \frac{1}{2} G^2 v_{\mathrm{l}} f_{\mathrm{sp}} L_{\mathrm{sp}} \tag{4.11}$$

where L_{sp} is the length of the single-phase region, which is calculated in COMSOL. The single-phase friction factor is calculated using a correlation developed by Shah and London [62] shown in equation 4.12.

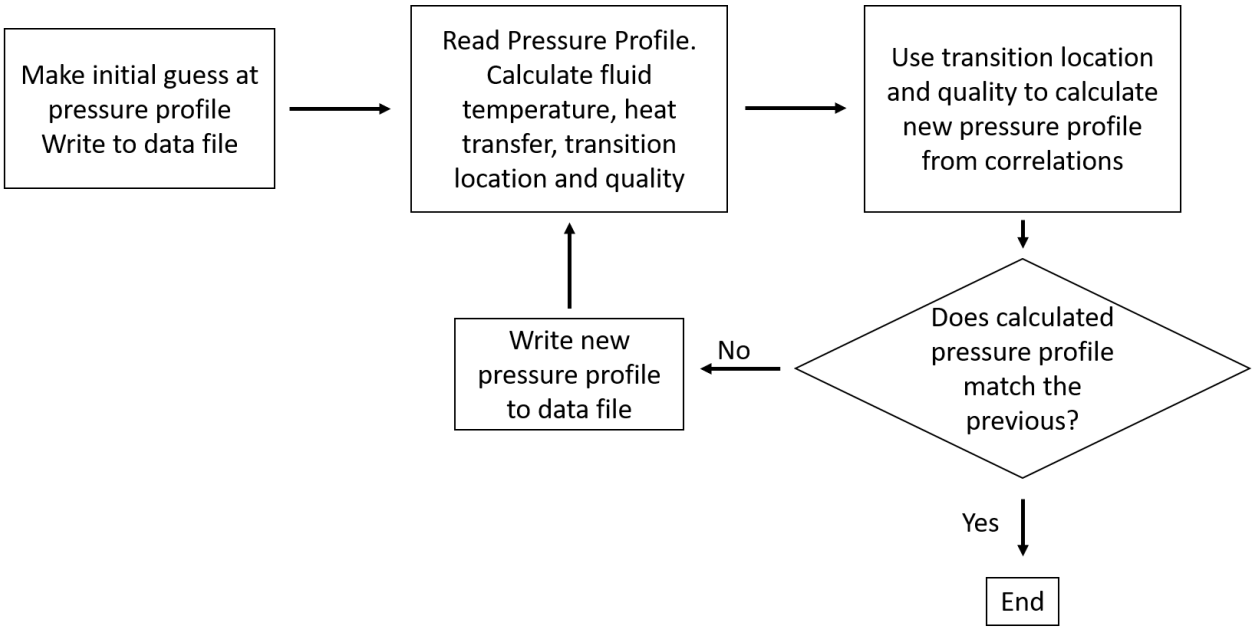

Figure 4.11: Iterative method for calculating the bulk fluid pressure profile by linking COMSOL with MATLAB

$$f_{\mathrm{sp}} = \frac{96}{Re_{\mathrm{l}}}(1 - 1.3553\beta + 1.9567\beta^2 - 1.7012\beta^3 + 0.9564\beta^4 - 0.2537\beta^5 \tag{4.12}$$

where β is the channel aspect ratio.

The correlations used to calculate pressure drop in the two-phase region are shown in equation 4.13 through equation 4.19.

$$\Delta P_{\mathrm{tp}} = \Delta P_{\mathrm{tp,f}} + \Delta P_{\mathrm{tp},\alpha} \tag{4.13}$$

$$\frac{\Delta P_{\mathrm{tp,f}}}{L_{\mathrm{tp}}} = \frac{1}{x}\int_0^x 2\phi^2 f G^2 \frac{(1-x)^2}{\rho_{\mathrm{l}} D_{\mathrm{h}}} dx \tag{4.14}$$

$$\phi = \sqrt{1 + \frac{C}{X_{\mathrm{vv}}} + \frac{1}{X_{\mathrm{vv}}}} \tag{4.15}$$

$$C = 2566 G^{0.5466} D_{\mathrm{h}}^{0.8819}(1 - e^{-319 D_{\mathrm{h}}}) \tag{4.16}$$

$$X_{\mathrm{vv}} = \left(\frac{\mu_{\mathrm{l}}}{\mu_{\mathrm{v}}}\right)^{1/2}\left(\frac{1-x}{x}\right)^{1/2}\left(\frac{\rho_{\mathrm{v}}}{\rho_{\mathrm{l}}}\right)^{1/2} \tag{4.17}$$

$$\Delta P_{\mathrm{tp},\alpha} = \frac{G^2}{\rho_{\mathrm{l}}}\left[\frac{x^2}{\alpha_{\mathrm{o}}(\frac{\rho_{\mathrm{l}}}{\rho_{\mathrm{v}}}} + \frac{(1-x)^2}{1-\alpha_(o)} - 1\right] \tag{4.18}$$

$$\alpha_{\mathrm{o}} = \left[1 + \left(\frac{1-x}{x}\right)\left(\frac{\rho_{\mathrm{l}}}{\rho_{\mathrm{v}}}\right)^{2/3}\right] \tag{4.19}$$

where X_{vv} given in equation 4.17 is the dimensionless Lockhart-Marteninelli parameter for laminar liquid-laminar vapor flow and α_{o}, given in equation 4.19, is the Zivi void fraction which is a measure of what portion of the channel cross section is occupied by liquid. These equations are solved and generate a pressure profile similar to the one shown in Figure 4.12. Here the single-phase to two-phase transition occurs near $x = 0.25\mathrm{mm}$. The single-phase pressure drop is lower than the two-phase pressure drop, because the fluid is moving faster in the two-phase region.

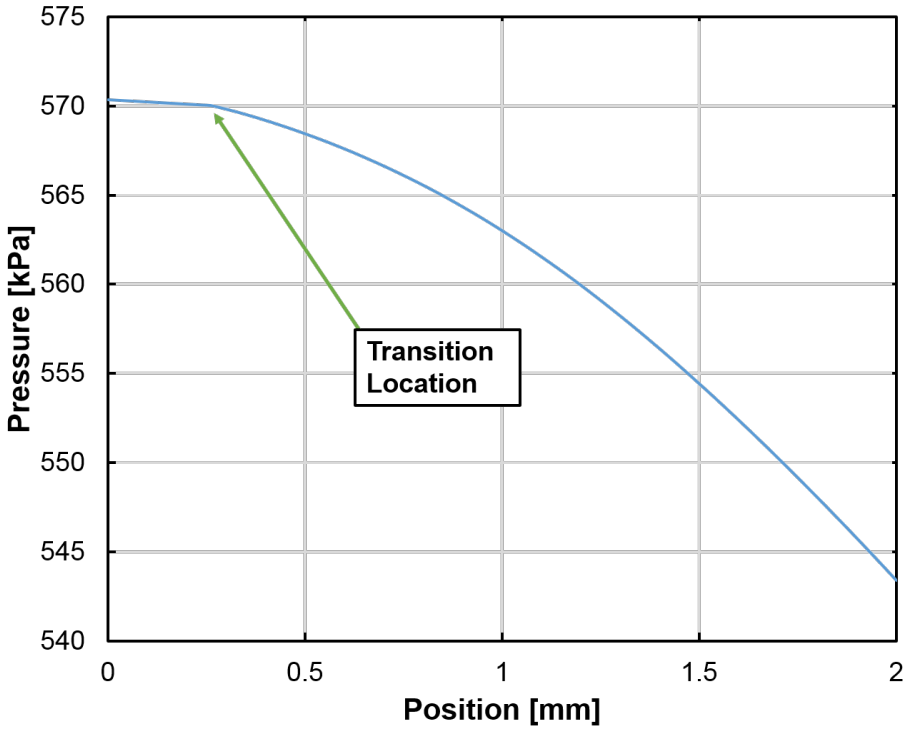

Figure 4.12: Example bulk fluid pressure profile through channel. The transition location from single-phase to two-phase fluid is shown at the inflection point.

Using the fluid pressure profile described above, COMSOL can proceed with the calculations to determine the bulk fluid temperature. As described above, in the single-phase region, fluid temperature is controlled by sensible heating. To calculate this temperature rise, the heat flux at the fluid-wall interface is integrated at each y location along the flow path and the following

equation is used:

$$\Delta T_{1,2} = \frac{\int_1^2 \dot{Q}(y)}{C \times \dot{m}} \tag{4.20}$$

where $\int_1^2 \dot{Q}(y)$ is the total integrated heat flux from location 1 to 2 along the y axis, $\dot{m}$ is the mass flow rate and C is the specific heat.

After the transition to a two-phase mixture, the fluids' temperature tracks the saturation temperature, which is a function of pressure. Because temperature and pressure are no longer independent variables in the two-phase mixture, enthalpy is now tracked as shown in equation 4.21:

$$\Delta i_{1,2} = \frac{\int_1^2 \dot{Q}(y)}{\dot{m}} \tag{4.21}$$

where the enthalpy of the mixture, *i*, is calculated as the quality weighted average:

$$\Delta i_{\text{mixture}} = (1 - x) i_{\text{l}} + x i_{\text{v}} \tag{4.22}$$

in which enthalpy for both the liquid and vapor phase are a function of temperature. Equation 4.21 and equation 4.22 can be combined to track the change in quality for a two-phase mixture as follows:

$$x_2 = \frac{\frac{\int_1^2 \dot{Q}}{\dot{m}} + (1 - x_1) i_{\text{l},1} + x_1 i_{\text{v},1} - i_{\text{l},2}}{i_{\text{v},2} - i_{\text{l},2}} \tag{4.23}$$

To find the transition location, a variable is created to track the fluid without a change in phase. This is compared to the profile of the fluid saturation temperature at the bulk pressure. The location where these variables meet is the transition location. The fluid temperature profile is created as a step function that follows the sensible heating temperature line to the left of the transition location and the saturation temperature line the the right. An example of this is shown in Figure 4.13 where T_{myth} is the fluid that does not undergo a phase change and T_{sat} is the saturation temperature profile.

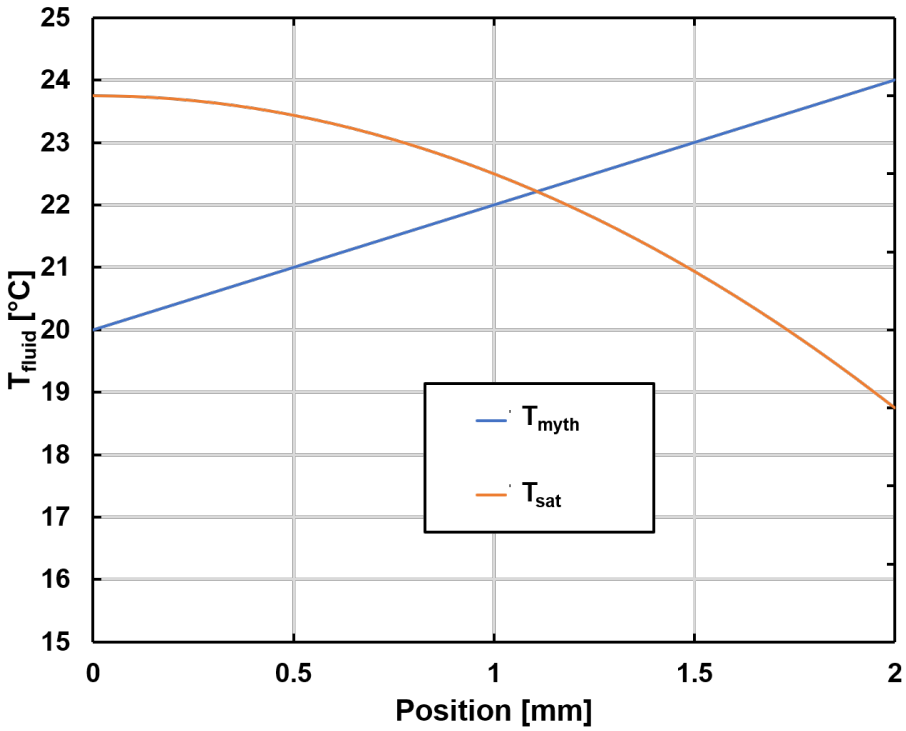

Figure 4.13: Superposition of the sensible heating temperature profile and the saturation temperature profile used to create the fluid bulk temperature profile.

4.2.3 Heat Transfer Coefficient Correlations

With the local fluid state fully defined, the heat transfer coefficients at the solid-fluid interface can be found. The heat transfer coefficients at the solid-fluid interface were calculated using correlations from the literature. Because of the very small hydraulic diameter of the channels in this study, and the high heat fluxes, no available correlations fully cover the range of conditions experienced during testing. For this reason, a survey of four two-phase heat transfer coefficient correlations was made to determine the suitability of each. This survey was performed on data gathered from the plane walled parts and the best performing correlation was modified to model the area enhanced parts.

4.2.3.1 Single-Phase Heat Transfer Coefficient

During tests, the working fluid enters the channel subcooled by around 3 W to avoid flashing, so each model contains a short single-phase region near the inlet. The correlation for single-phase

heat transfer coefficient comes from Cooper et. al. [63] which was developed based on a large data set presented by Shah and London [62]. Kim and Mudawar [64] showed this correlation to have good agreement with the data they surveyed. The single-phase heat transfer coefficient for the thermally developing laminar region is given by equation 4.24.

$$Nu_{\mathrm{x}} = \left\{ \left[1.54 \Big(\frac{L_{\mathrm{sp}}}{Re_{\mathrm{sp}} Pr_{\mathrm{l}} D_{\mathrm{h}}} \Big)^{-0.33} \right]^4 + Nu_3^4 \right\}^{1/4} \tag{4.24}$$

where Nu_3 is given as:

$$Nu_3 = 8.235\big(1 - 1.833\beta + 3.767\beta^2 - 5.814\beta^3 + 5.361\beta^4 - 2.0\beta^5\big) \tag{4.25}$$

No survey of single-phase heat transfer coefficients is performed in this study because this value has only a minor impact on the modeling results. In general, the single-phase heat transfer coefficient is at least an order of magnitude lower than the two-phase heat transfer coefficient. For example, the calculated single-phase heat transfer coefficient from a represented case presented in Figure 5.5 is 1.2 $\mathrm{kW\,m^{-2}K^{-1}}$. In contrast the peak two-phase heat transfer coefficient is 9.7 $\mathrm{kW\,m^{-2}K^{-1}}$.

4.2.3.2 Agostini and Bontemps

Agostini and Bontemps developed a correlation for R134a in 2.01 mm aluminum rectangular channels. 11 parallel channels were oriented vertically, with mass fluxes ranging from 90 $\mathrm{kg\,m^{-2}s^{-1}}$ to 295 $\mathrm{kg\,m^{-2}s^{-1}}$. Data was collected over a full range of vapor qualities allowing them to generate a correlation for heat transfer coefficient on either side of dryout. This is shown in equation 4.26 and 4.27 for below and above the critical vapor quality, respectively.

$$h_{\mathrm{tp}} = 28 \cdot q''^{2/3} \cdot \dot{m}^{-0.26} \cdot x^{-0.10} \quad for\ x < 0.43 \tag{4.26}$$

$$h_{\mathrm{tp}} = 28 \cdot q''^{2/3} \cdot \dot{m}^{-0.64} \cdot x^{-2.08} \quad for\ x > 0.43 \tag{4.27}$$

4.2.3.3 Bertsch

This correlation developed by Stefan Bertsch at Purdue comes from a database of 14 studies covering 12 working fluids containing 3899 data points [65]. This data covers channel hydraulic diameters between 0.16 mm to 2.92 mm which give confinement numbers between 0.3 to 4.0. Mass flux ranges from 20 $\mathrm{kg\,m^{-2}s^{-1}}$, heat flux ranges from 0.4 $\mathrm{W\,cm^{-2}}$ to 115 $\mathrm{W\,cm^{-2}}$ and all vapor qualities are contained. The majority of channels surveyed are arranged horizontally.

The two-phase heat transfer coefficient given here is represented as the superposition of nucleate boiling and convective boiling. The nucleate boiling term is accompanied by a suppression factor, S, and the convective boiling term is multiplied by an enhancement factor, F, as shown in equation 4.28.

$$h_{\mathrm{tp}} = S \cdot h_{\mathrm{nb}} + F \cdot h_{\mathrm{cb}} \tag{4.28}$$

It is reasoned that there should no suppression in nucleate boiling in a saturated liquid such that $S_{\mathrm{x=0}} = 1$. Similarly, in a saturated vapor, no nucleate boiling can occur and $S_{\mathrm{x=1}} = 0$. Therefore, the supression factor S is given as:

$$S = (1 - x) \tag{4.29}$$

In previous work by Berstch et. al., it was shown that in very small channels, which are nucleate boiling dominated, a correlation for saturated pool boiling showed better agreement than any of the flow boiling equations surveyed [66]. The correlation from Cooper et. al. [18] is used as the nucleate boiling term, h_{nb} in equation 4.28:

$$h_{\mathrm{nb}} = 55 \cdot P_{\mathrm{r}}^{0.12-0.2 \cdot log_{10} R_{\mathrm{p}}} \cdot \left(- log_{10} P_{\mathrm{r}} \right)^{-0.55} \cdot M^{-05} \cdot \left(q'' \right)^{0.67} \tag{4.30}$$

where P_{r} is the reduced pressure, M is the molecular mass, and q'' is the local heat flux. R_{p} is the peak surface roughness, in $\mu\mathrm{m}$ given by ISO standard 4287.

The convective boiling term, h_{cb}, in equation 4.28 is a function of transport and fluid properties, weighted by vapor quality and shown in equation 4.31:

$$h_{\mathrm{cb}} = (1-x)\cdot h_{\mathrm{cb,l}} + x \cdot h_{\mathrm{cb,v}} \tag{4.31}$$

where $h_{\mathrm{cb,i}}$ for the liquid and vapor phase is given as:

$$h_{\mathrm{cb,i}} = \left(3.66 + \frac{0.0668 \cdot \frac{D_{\mathrm{h}}}{L} \cdot Re \cdot Pr}{1 + 0.04 \cdot \left[\frac{D_{\mathrm{h}}}{L} \cdot Re \cdot Pr\right]^{2/3}}\right) \cdot \frac{k_{\mathrm{i}}}{D_{\mathrm{h}}} \tag{4.32}$$

Finally, the enhancement factor, F, can be found from a curve fit of the data and is given as:

$$F = \left[1 + 80 \cdot (x^2 - x^6) \cdot e^{-0.6Co}\right] \tag{4.33}$$

4.2.3.4 Kim and Mudawar

The Kim and Mudawar was widest ranging correlation surveyed in in this study [67]. The database used to develop this correlation contains 12,974 data points from 37 sources. 18 working fluids are included: 16 refrigerants, water and CO_2. Channel hydraulic diameters range from 0.16 mm to 6.5 mm. Mass flux ranges from 19 $\mathrm{kg\,m^{-2}s^{-1}}$ to 1608 $\mathrm{kg\,m^{-2}s^{-1}}$ and all vapor qualities are covered. Again, the total two-phase heat transfer coefficient is described as the superposition of nucleate boiling, h_{nb}, and convective boiling, h_{cb}, shown in equation 4.34 although the superposition is done differently as shown in equation 4.34.

$$h_{\mathrm{tp}} = \left(h_{\mathrm{nb}}^2 + h_{\mathrm{cb}}^2\right)^{0.5} \tag{4.34}$$

The nucleate and convective boiling terms come from curve fits and are given in equation 4.35 and equation 4.35 respectively.

$$h_{\mathrm{nb}} = \left[2345\left(Bo\frac{P_{\mathrm{H}}}{P_{\mathrm{F}}}\right)^{0.70} P_{\mathrm{r}}^{0.38}\left(1-x\right)^{-0.51}\right]\left(0.023 Re_{\mathrm{f}}^{0.8} Pr_{\mathrm{f}}^{0.4}\frac{k_{\mathrm{f}}}{D_{\mathrm{h}}}\right) \tag{4.35}$$

$$h_{\mathrm{cb}} = \left[5.2\left(Bo\frac{P_{\mathrm{H}}}{P_{\mathrm{F}}}\right)^{0.08} We_{\mathrm{fo}}^{-0.54} + 3.5\left(\frac{1}{X_{\mathrm{tt}}}\right)^{0.94}\left(\frac{\rho_{\mathrm{v}}}{\rho_{\mathrm{l}}}\right)^{0.25}\right]\left(0.023 Re_{\mathrm{f}}^{0.8} Pr_{\mathrm{f}}^{0.4}\frac{k_{\mathrm{f}}}{D_{\mathrm{h}}}\right. \tag{4.36}$$

where the Bo, P_{r}, Re_{l}, We_{fo}, and X_{tt} are the boiling number, reduced pressure, liquid Reynolds number, fluid only Weber number, and turbelent-turbulent Lockhart-Martinelli parameter, respectively. The boiling number, Weber number and Martinelli parameter are defined in equation 4.37:

$$\begin{aligned} Bo &= \frac{q''_{\mathrm{H}}}{G h_{\mathrm{fg}}} \\ We_{\mathrm{fo}} &= \frac{G^2 D_{\mathrm{h}}}{\rho_{\mathrm{l}} \sigma} \\ X_{\mathrm{tt}} &= \left(\frac{\mu_{\mathrm{l}}}{\mu_{\mathrm{v}}}\right)^{0.1} \left(\frac{1-x}{x}\right)^{0.9} \left(\frac{\rho_{\mathrm{v}}}{\rho_{\mathrm{l}}}\right)^{0.5} \end{aligned} \tag{4.37}$$

where, q'' is the effective heat flux, averaged over the heated perimeter, P_{H} is the heated perimeter and P_{F} is the wetted perimeter. In the present study, P_{H} represents only the silicon area, so $P_{\mathrm{H}} = 2 \cdot h_{\text{channel}} + w_{\text{channel}}$ whereas P_{F} includes the glass cap, so $P_{\mathrm{F}} = 2 \cdot h_{\text{channel}} + 2 \cdot w_{\text{channel}}$.

Finally, it should be noted that this correlation is developed for vapor qualities below x_{di}, the vapor quality at which dryout incipience occurs. A separate correlation is used to predict x_{di} [32] but because it does not include inlet restrictions and is not relevant in the current work.

4.2.3.5 Lazerek and Black

The Lazerek and Black correlation was developed for saturated boiling of R-113 in vertical 3.1 mm diameter steel tubes [68]. Vapor qualities were included up to x_{di}, which occurred at a maximum of 0.89. A correlation for dryout incipience accompanies the heat transfer coefficient correlation. Mass fluxes range between 125 $\mathrm{kg\,m^{-2}s^{-1}}$ - 750 $\mathrm{kg\,m^{-2}s^{-1}}$ and wall heat fluxes range from 9.31 $\mathrm{Wcm^{-2}}$ - 33.6 $\mathrm{Wcm^{-2}}$. The correlation, which does not separate nucleate and convective boiling regimes is given in equation 4.38. It is interesting to note that this heat transfer coefficient is both dependent on local heat flux and mass flow rate.

$$Nu = 30 \cdot Re^{0.875} \cdot Bo^{0.714} \tag{4.38}$$

Each of the correlations above relies heavily on fluid properties to determine heat transfer coefficients. Determination of the relevant fluid properties is described in the following section.

4.2.4 Thermophysical Properties

Correct determination of fluid properties is critical for the correct use of the heat transfer coefficient and pressure drop correlations in this model. All properties used in this study are relatively insensitive to changes in pressure over the small pressure range experienced through the channels. For this reason, variables are interpolated based on temperature from files for saturated liquid and vapor R134a. In total 7 properties are needed for the correlations mentioned above, 5 of which must be found for both the liquid and vapor phase. The necessary properties are viscosity ($\mu_{\mathrm{l,v}}$, $\mathrm{kg\,m^{-1}s^{-1}}$), conductivity ($k_{\mathrm{l,v}}$, $\mathrm{Wm^{-1}K^{-1}}$), density ($\rho_{\mathrm{l,v}}$, $\mathrm{kg\,m^{-3}}$), Prandtl number ($Pr_{\mathrm{l,v}}$, -), enthalpy ($i_{\mathrm{l,v}}$, $\mathrm{kJ\,kg^{-1}}$), enthalpy of vaporization (i_{fg}, $\mathrm{kJ\,kg^{-1}}$), and surface tension (σ, $\mathrm{Nm^{-1}}$).

These properties are derived from the fundamental equation of state for R134a presented by R. Tiller-Roth and H.D. Baehr [69]. For this derivation, specific enthalpy and entropy are set to 0 $\mathrm{kJ\,kg^{-1}}$ and 0 $\mathrm{kJ\,kg^{-1}K^{-1}}$ at -40°C . Liquid and vapor conductivity are calculated from a correlation using a relation from Huber and Laesecke at NIST [70]. Similarly, liquid phase conductivity is taken from a correlation from Assael and Dalaouti [71].

These equations are accessed using Engineering Equation Solver (EES) and the properties are then written to data files as a function of temperature from 273.15 K to 373.15 K in 2 K increments. All values are found at the saturation line as this reflects the conditions seen within the channel. Once these data files have been generated, COMSOL performs an linear interpolation to find each of the properties listed above for a given temperature.

Finally, the last property that must be found is the conductivity of silicon. For simplicity, this calculated directly in COMSOL using the two piece linear curve fit given in equation 4.39 where the conductivity is given in $\mathrm{Wm^{-1}K^{-1}}$.

$$k_{\mathrm{si}}(T) = \begin{cases} -0.8603 \cdot T + 406.08 & for\ 273\,[\mathrm{K}] < T < 300\,[\mathrm{K}] \\ -0.4918 \cdot T + 295.54 & for\ 300\,[\mathrm{K}] < T < 373\,[\mathrm{K}] \end{cases} \tag{4.39}$$

This concludes the description of the computational model. With the methods described above, local heat flux and heat spreading seen during the experiments can be quantified. The following section first presents the experimental data, and then the findings from the computational model.

Chapter 5: Results and Discussion

Chapter 3 described the experimental data collection procedure and chapter 4 explained the computational model used to interpret this data. These findings are presented here in 3 main parts. First in Section 5.1, the results from the experiments are presented. This includes thermal resistance, critical heat flux, and pressure drop. Next, in Section 5.2, the inputs from the test data are fed into the computational model to evaluate the differences. The results of the modeling showed 5.5°C deviation from the Bertsch correlation, so a modification to the correlation is presented in Section 5.3. Next, heat transfer coefficients and heat spreading are quantified in Section 5.4 and Section 5.5, respectively. Finally, predictions are made for alternate geometries using the model in Section 5.6.

5.1 Experimental Results

5.1.1 Heat Transfer Performance

Three tests were performed for one plain walled and two area enhanced designs (total of nine tests). The test sections were swept through a range of maximum heater temperatures with constant inlet conditions beginning at 40°C and increasing in 5°C increments until critical heat flux was observed. The heat transfer performance of the three designs are shown graphically in Figure 5.1. The error bars in this figure show total uncertainty, U, as was calculated in section 3.4. This is done for each point except the two points highlighted in green. These points are where only a single data point was taken as the other two test sections in these series reached critical heat flux at the next highest heater temperature and heat input. For these two points, only bias uncertainty is shown. If these two points are ignored, a clear improvement in the onset of critical heat flux, and therefore quality at dryout incipience, is seen with the area enhanced parts.

Additionally, some difference is seen in the thermal resistance between the different test sections. On average a 36% reduction in thermal resistance is seen in the 6 μm area enhanced parts as compared to the plane walled parts. However, the 3 μm test sections, which have the same 41% area enhancement, show only a 4% reduction in thermal resistance which, as shown by the error

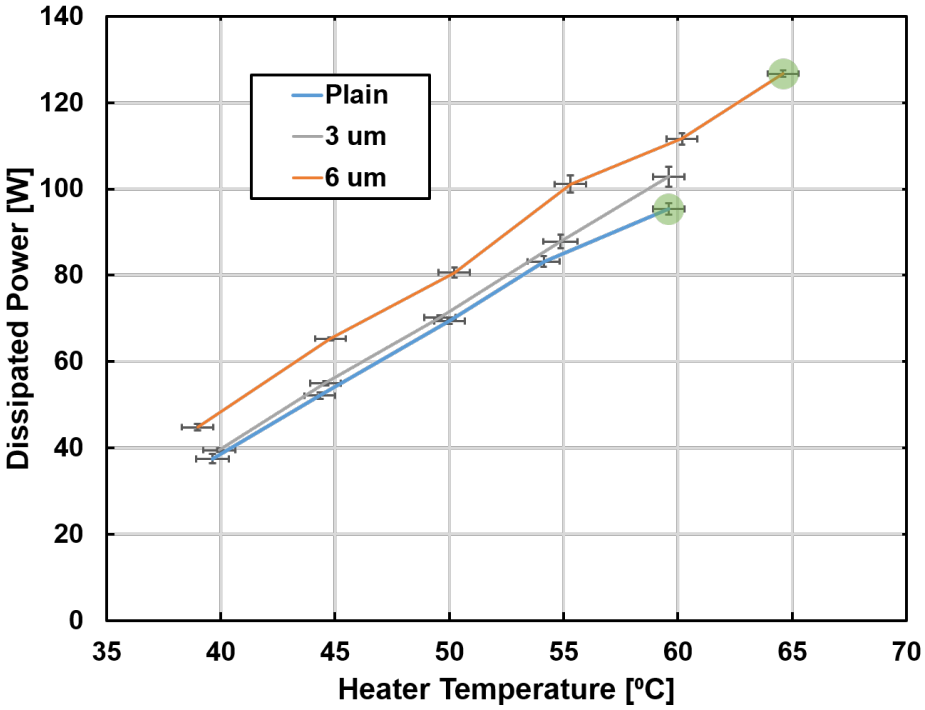

Figure 5.1: Dissipated power as a function of maximum heater temperature for plane walled parts and 2 schemes of area enhanced parts. Data shown highlighted in green represents only a single data point.

bars, is not a significant difference. This seems to be counter intuitive and will be investigated further.

5.1.2 Pressure Drop

Pressure drop as a function of input heater power is shown in Figure 5.2. Interestingly, the data groups differently when compared to Figure 5.1. On average, the serrated parts show a 25% and 29% increase in pressure drop at each power for the 3 μm and 6 μm test sections, respectively. As shown by the error bars in Figure 5.1, the difference in pressure drop performance between the two area enhanced parts is not significant. The difference in pressure drop between the plane walled parts and area enhanced parts likely is caused by a reduction in hydraulic diameter from the sawtooth features, which protrude slightly into the flow. The single-phase flow in the channels is highly laminar ($Re = 263$) because of the small hydraulic diameter. Therefore, it is unlikely

that surface roughness is affecting the pressure drop as the fluid is stationary along the walls. The surface roughness may cause more turbulent flow in the two-phase regime.

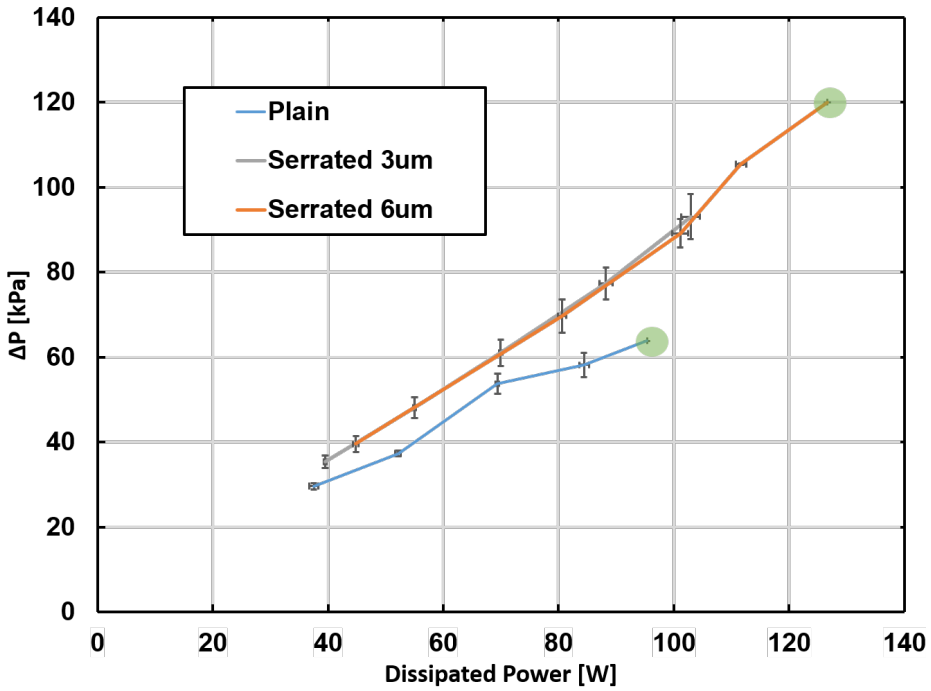

Figure 5.2: Pressure drop across the interface manifold as a function of applied power for plane walled parts and 2 schemes of area enhanced parts. Data shown highlighted in green represents only a single data point.

It may be argued that the increase in pressure drop for the area enhanced parts results in an artificially reduced thermal resistance. The logic for this argument is that the increased pressure drop through the test section results in a lower pressure over the heater for the same inlet conditions. This in turns, leads to a lower temperature for the two-phase mixture over the heater. However, when comparing both the thermal resistance and pressure drop results, it is clear that this effect is negligible. Both the 3 μm and 6 μm test sections have nearly pressure drop results. However, the performance increase is only observed in the 6 μm test sections. For example, linear interpolation can be used to examine an 80 W heat input case. For this heat input condition, it is expected that the plain walled parts will yield an 8.25 psi pressure drop and 53.3 °C heater temperature. The 3 μm test sections are expected to show an increased pressure drop of 10.16 psi but have a similar thermal

resistance with a 52.8 °C heater temperature. For the 6 μm test section, a nearly identical pressure drop of 10.0 psi is expected; however, the heater temperature is reduced to 49.9 °C. Furthermore, the increase in pressure drop can account for at most a 0.66 °C reduction in saturation temperature, which, when taken into account, still yields a significant reduction in thermal resistance.

5.2 Determination of Conjugate Heat Transfer Performance

To understand the reason for the performance differences, the data shown in section 5 is input into the model described in section 4.1. After the model converged, the temperatures along the backside were compared to the data gathered from the pyrometer to asses the accuracy of each heat transfer coefficient correlation. This was done for each of the plane walled cases and as an example, the 55°C case is shown in Figure 5.3.

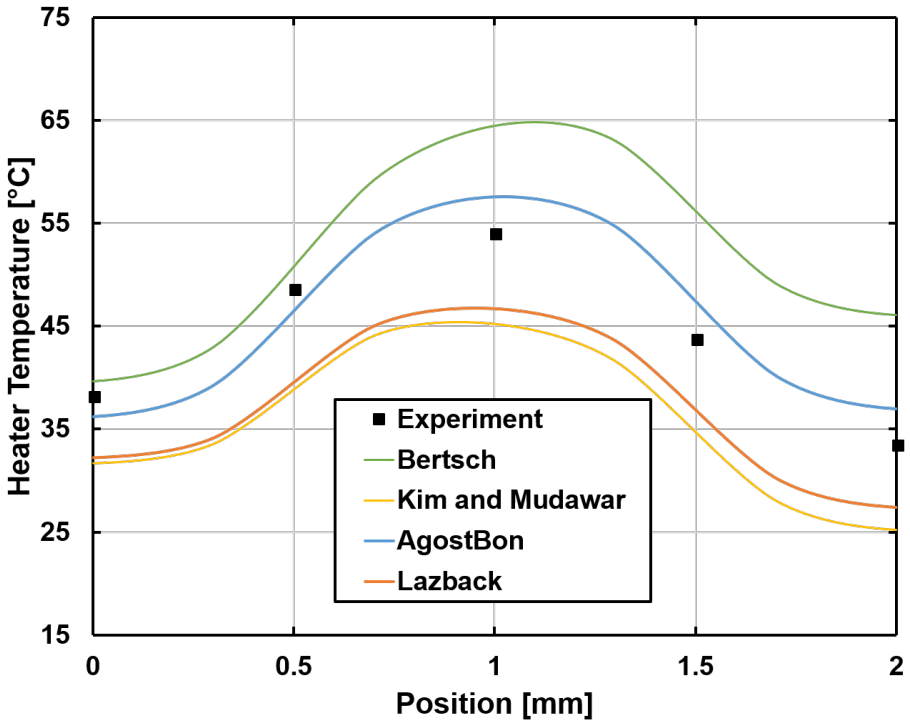

Figure 5.3: Comparison of the four heat transfer coefficients to the collected data for the plane walled 55°C heater case.

To quantify the reliability of each correlation, the root mean square error ($RMSE$) is used which is defined in equation 5.1:

$$RMSE = \sqrt{\frac{\sum_{\mathrm{i}=1}^{N}(T_{\mathrm{i}} - \hat{T}_{\mathrm{i}})^2}{N}} \tag{5.1}$$

where $\hat{T}_{\mathrm{i}}$ is the experimental temperature and T_{i} is the model temperature at the same location. This is done for each experimentally measured heater temperature for each plane walled test sections. The average $RMSE$ for each correlation tested is shown in Table 5.1. The correlation from Agostini and Bontemps most closely matched the data, tending to slightly underpredict the heater temperature below the channel inlet and slightly overpredict below the channel outlet. However, because the Agostini and Bontemps correlation does not separate nucleate and convective boiling terms and does not include a roughness term, it offers little insight into the behavior of the test sections. A similar argument is made for the Lazarek and Black correlation, which undpredicts the heater temperature. For these reasons, the correlation presented by Bertsch was chosen for modification to model the area enhanced parts as described in section 4.1.

Table 5.1: Average RMSE for each heat transfer coefficient correlations used to predict the plane walled data.

Correlation	RMSE [°C]
Bertsch	5.1
Kim & Mudawar	8.6
Lazareck & Black	7.2
Agostini & Bontemps	3.0

Using the modifications to the heat transfer coefficients for the walls of the area enhanced parts, the remaining models were run using the Bertsch correlation. As described above, $RMSE$ is again calculated for each trial and is shown in Figure 5.4 plotted against the heat input. In general, as the heat input increases, the correlation becomes less predictive. In all cases, the correlation under-

predicts the two-phase heat transfer coefficient, so the backside temperature is overpredicted. In general, this affect is more pronounced at the outlet, suggesting that the single-phase heat transfer coefficient correlation is more reliable or that the Bertsch correlation is more predictive for these geometries at low vapor qualities. These ideas will be explored in the following section.

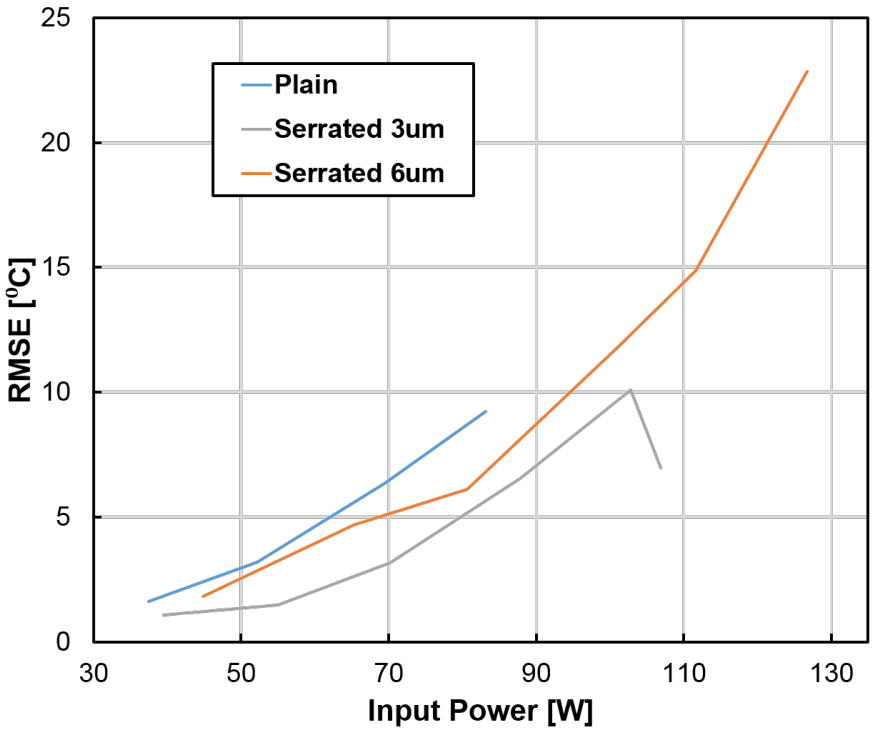

Figure 5.4: Root Mean Square Error ($RMSE$) for each trial using the Bertch correlation.

5.3 Modification to Bertsch Correlation

The inference that the two-phase heat transfer coefficient is undepredicted at high vapor qualities warrants exploration. First, it should be noted that in all cases, nucleate boiling is the dominant heat transfer mechanism. This is shown graphically in Figure 5.5 for the 55°C plain wall case. As is shown, the nucleate boiling term, h_{nb} can contribute up to 95 percent of the total two-phase heat transfer coefficient, h_{tp}. With this in mind, any modification aimed an increasing the acuracy of the Bertsch correlation in smaller channels should focus on the nucleate boiling term. For example, if a calculated total heat transfer coefficient, h_{tp} is 100 $\mathrm{kW\,m^{-2}K^{-1}}$ and the calculated

nucleate boiling term, h_{nb} is 90 $\mathrm{kW\,m^{-2}K^{-1}}$, to retrieve a measured heat transfer coefficient of 110 $\mathrm{kWm^{-2}K^{-1}}$, the nucleate boiling term needs to be increased by 11 percent. In contrast, the convective boiling term would need to be doubled.

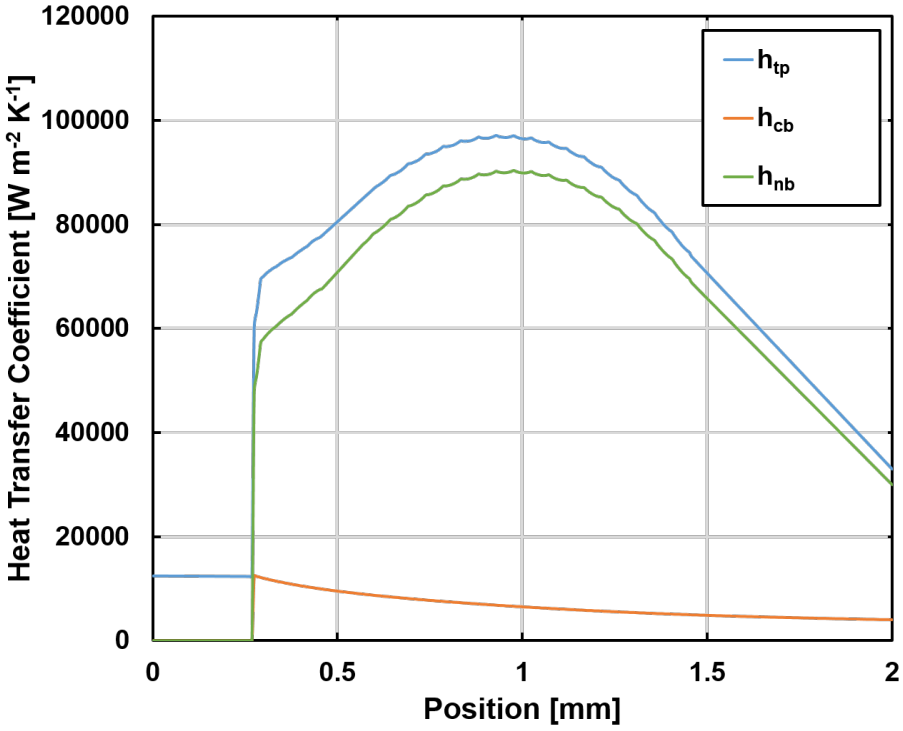

Figure 5.5: Contributions of nucleate boiling, h_{nb}, and convective boiling, h_{cb}, to the total two-phase heat transfer coefficient, h_{tp}, shown for the 55°C plane walled case.

As mentioned in Section 4.2.3, the Bertsch correlation multiplies a suppression factor, S, with the nucleate boiling term and an enhancement factor, F, with the convective boiling term as shown in equation 5.2.

$$h_{\mathrm{tp}} = S \cdot h_{\mathrm{nb}} + F \cdot h_{\mathrm{c}} \tag{5.2}$$

In the development of the correlation, first the nucleate boiling, h_{nb}, term is set using the correlation from Cooper [18]. Next, the suppression factor, S, is set using two boundary conditions at qualities $x = 0$ and $x = 1$, with the simplest interpolation between these points such that $S = (1 - x)$. Then, developing h_{cb} from fluid and transport properties, a curve fit is used to find

F. The interpolation for the suppression factor, S, is of particular interest. In an earlier study that tested the predictive performance of several correlations for two-phase heat transfer coefficients in microchannels, the Cooper correlation, which was developed for pool boiling, was found to be the most accurate. In this study, no suppression factor is used and it is noted that the heat transfer coefficient is underpredicted at low vapor qualities and overpredicted at high vapor qualities [66]. It is also noteworthy that the Bertsch study covered hydraulic diameters ranging from 0.16 mm to 2.1 mm and within this range, the Cooper correlation predicted data better for smaller channels. Based on the performance of the Cooper correlation without a suppression factor in small channels, an investigation of a new suppression factor is warranted for smaller channels. For this investigation, the suppression factor will retain the boundary conditions at $x = 0$ and $x = 1$ and seek to extend the range of vapor qualities over which nucleate boiling is present. The suggested form for the suppression factor is $S = 1 - x^{\lambda}$. To find the exponent, λ, each model is run with increasing whole number values and the $RMSE$ is logged. An example of this study is shown graphically in Figure 5.6 where only the plane walled parts are shown for clarity.

This process is repeated for each data point and the root mean square error is calculated for each exponent, λ, as is shown in Figure 5.7. When averaged together, error is minimized at $\lambda = 5$ where total average RMSE for all trials is reduced to 2.2°C from 5.5°C for $\lambda = 1$. Proceeding forward, all data presented from the model is gathered using this modified suppression factor.

5.4 Heat Transfer Coefficient and Local Heat Flux

By applying the modified Bertsch correlation, the heat transfer coefficients and heat flux values begin to explain the performance of the the area enhancements. Both area enhanced test sections had a 41% increase in area compared to the plane walled parts; however, this did not correspond to an equivalent decrease in thermal resistance. To explain this discrepancy, peak heat transfer coefficients for both the floor and wall are shown at each power level in Figure 5.8. In the plane walled parts, the maximum heat transfer coefficient at the channel floor is much higher than the maximum heat transfer coefficient that occurs on the channel wall. In contrast, the heat transfer

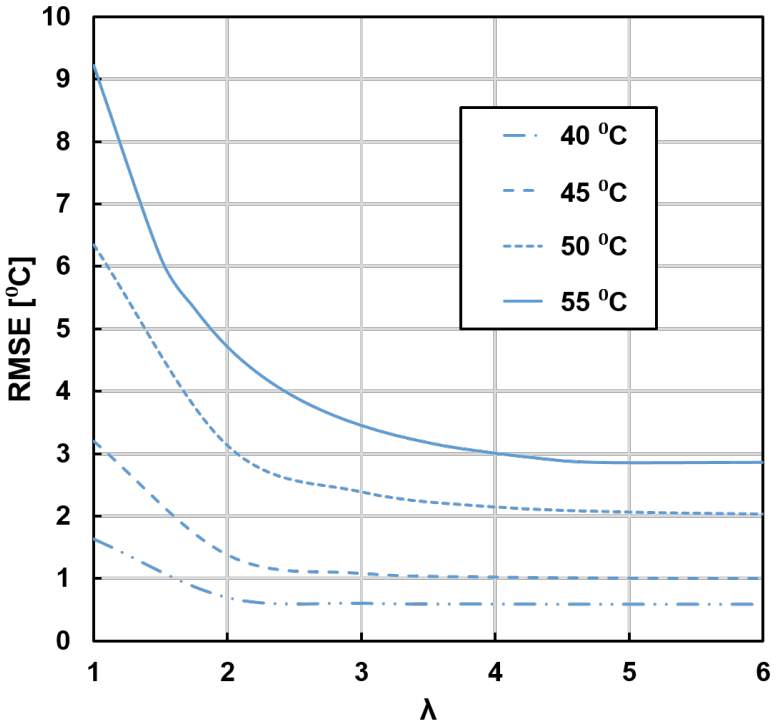

Figure 5.6: RMSE with modified supression factor where $S = 1 - x^{\lambda}$.

coefficient for the channel wall is increased for the area enhanced parts. This increase can be explained by the surface roughness parameter, Rp. One effect of the increased wall heat transfer was a decrease in the peak heat transfer coefficient seen at the channel floor.

To explain the reduction in heat transfer coefficient at the channel floor, local heat flux is examined. The peak heat flux for each data point is shown in Figure 5.9. As the available heat transfer area and heat transfer coefficient are increased at the wall, the thermal resistance of the fin is reduced and heat is preferentially distributed through the fin. Because nucleate boiling heat transfer coefficients are strongly dependent on local heat flux, this reduction of heat flux at the channel floor leads to a reduction in local heat transfer coefficient as seen in Figure 5.8.

5.5 Heat Spreading

In this study, the channels have been oversized relative to the heater to reduce the thermal resistance of the test sections by providing more area available for heat transfer. This section investigates if this extra area is being utilized effectively.

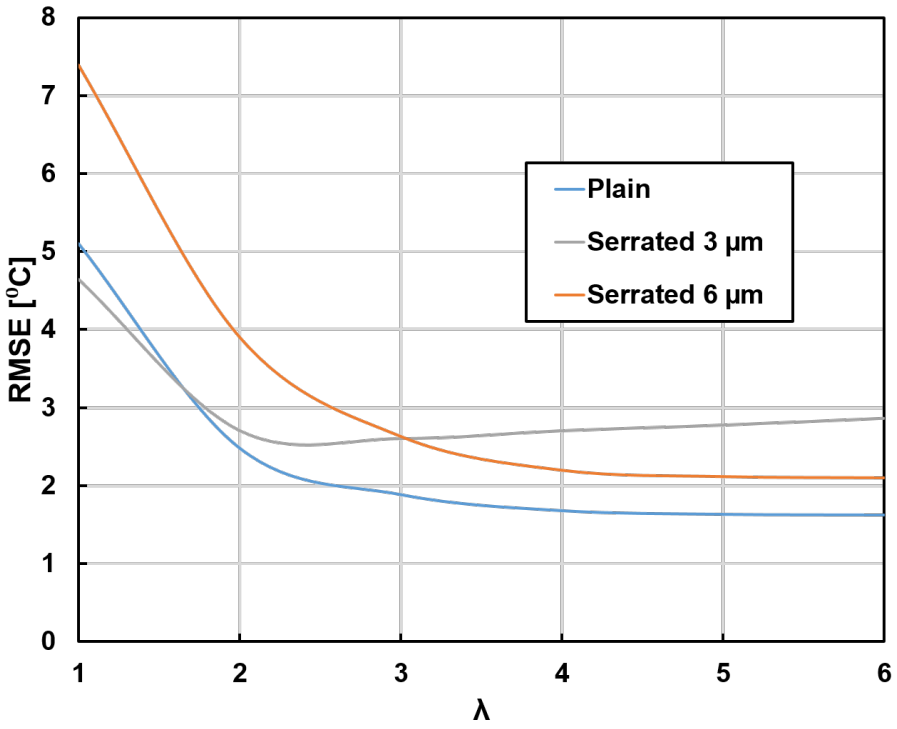

Figure 5.7: Average RMSE for each modified supression factor where $S = 1 - x^{\lambda}$.

To visualize heat spreading, the channel is separated into 3 sections: a 0.5 mm section upstream of the heater, the 1 mm section directly above the heater, and the 0.5 mm section downstream of the heater. By integrating the total surface heat flux at each location along the channel, total heat transfer in each section can be found. As an example, this is shown graphically for the 40°C and 55°C case in Figure 5.10. In this figure, the area directly above the heater is shown in light blue. Interestingly, there is almost no difference (6.2%) in heat spreading between these two extreme cases other than the single-phase to two-phase transition location, which occurs at the inflection point. This is typical of all the data. This is likely because peak heat transfer coefficients occur directly above the heater, whether they occur on the floor for the plane walled parts, or the wall for the area enhanced parts.

The same analysis is performed for all the models and the results for the lowest and highest power tested in each test section are summarized in Table 5.2. Interestingly, there is almost no difference in heat spreading as power is increased. The 6 μm parts did increase the amount of heat dissipated directly over the heater, which shows that the channels upstream and downstream of the

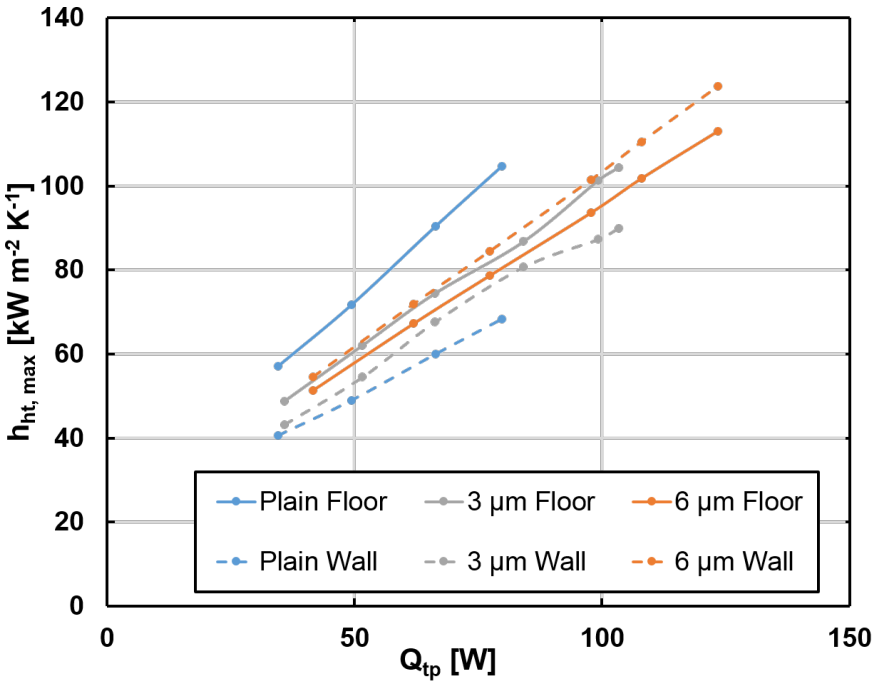

Figure 5.8: Maximum heat transfer coefficient at both the floor and wall for each data point.

heater are not being used effectively although it is not clear how this could be fixed. Heat is not easily dissipated upstream of the heater because that region is largely single-phase and therefore has a higher thermal resistance. Similarly, downstream of the heater, high vapor qualities and lower local heat flux reduce the two-phase heat transfer coefficient. A study on the effect of inlet subcooling magnitude is warranted so that the degree of subcooling can be reduced without inducing flashing.

Table 5.2: Percentage of total heat dissipated in each section.

Test	Upstream	Over Heater	Downstream
Plain 40°C	16.3	63.8	19.9
Plain 55°C	16.3	65.6	18.1
3 μm 40°C	17.2	63.5	19.3
3 μm 60°C	16.5	66.6	16.9
6 μm 40°C	15.5	65.7	18.8
6 μm 65°C	15.8	69.0	15.2

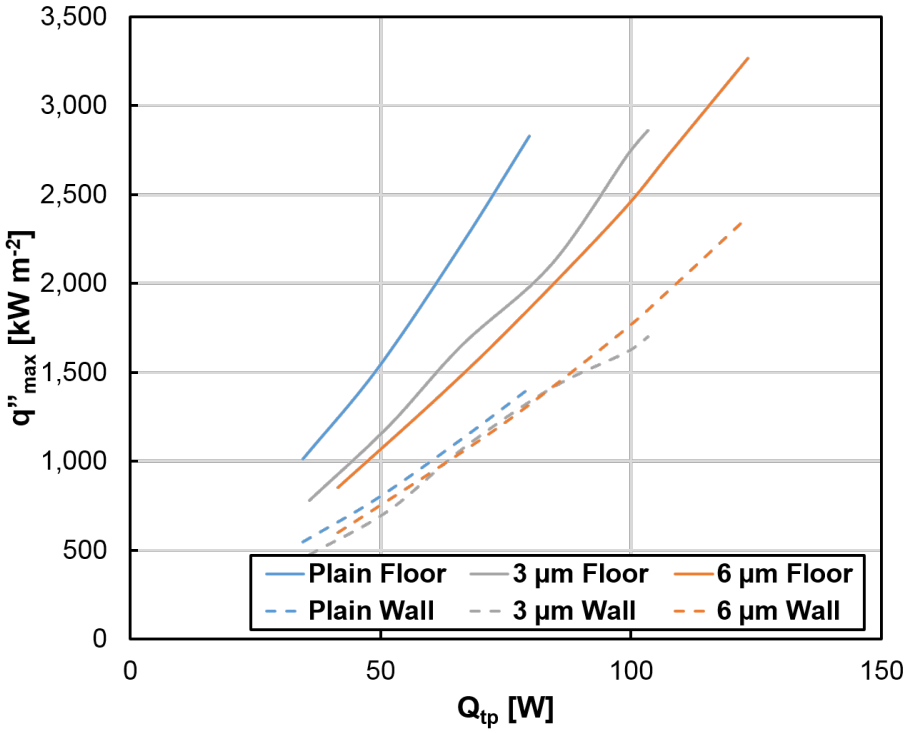

Figure 5.9: Maximum heat flux at the channel wall and channel floor.

5.6 Predictions for Alternate Geometries

Because a significant performance improvement is seen with the 6 μm parts, and to a lesser degree with the 3 μm parts, a parametric study to find the optimal geometry is of interest. For this study, two parameters are investigated: surface roughness and area enhancement factor. Surface roughness was chosen as the first variable in this study due to the significant performance improvements as shown above. The feature height parameter acts as a proxy for the surface roughness. As the features are introduced to the walls and floor, the heat transfer surface area is enhanced. Thus, the area enhancement factor was a logical second parameter for this study. The area enhancement factor is controlled by setting the angle of the sawtooth pattern, α as shown in Figure 5.11.

For this study, the sawtooth angle was varied from 15° to 75° in 15° increments. This corresponds to area enhancements ranging from 1.04 to 3.86. Similarly, surface roughness, R_{p}, was varied from 1 μm to 12 μm in increments of 1 μm. The tests were performed with identical inlet and boundary conditions as shown in Table 5.3. These conditions are given at the channel inlet, not

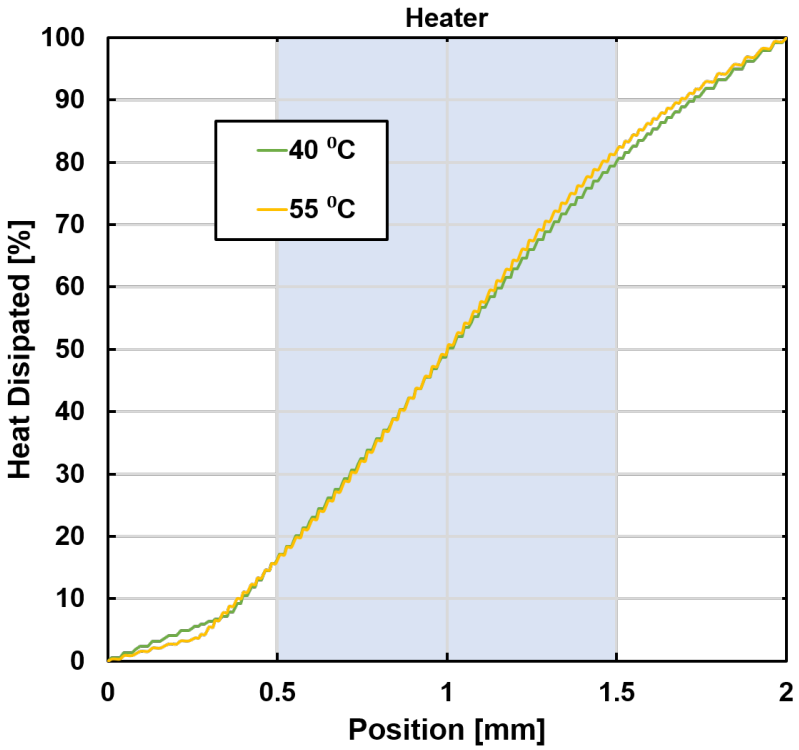

Figure 5.10: Integrated heat flux along the flow bath for the 40°C and 55°C plane walled cases.

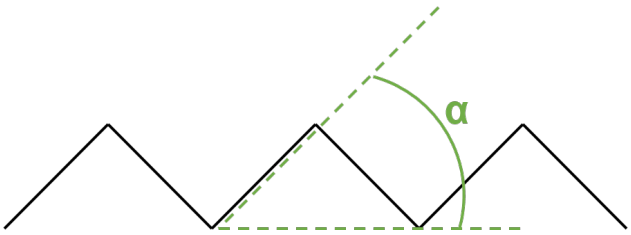

Figure 5.11: Definition of sawtooth angle which controls the area enhancement factor.

the pressure tap upstream of the channel orifice. For comparison, they are shown with the average inlet conditions from testing. Heat input from testing is not shown because it was varied for each test. The heat input, Q_{heater}, and mass flow rate, $\dot{m}$, are given for the entire test section; they are reduced to a per channel basis in the model. These conditions correspond to 3.3 W of subcooling.

The average heater temperature is extracted to compare the performance of the each geometry and the results of this analysis are shown graphically in Figure 5.12. Some interesting insights can be gained from this study. First, additional area enhancement decreases the thermal resistance of the test sections, even with small roughness factors. This is not the same inference that is

Table 5.3: Inlet conditions for geometry optimization study.

Parameter	Study Value [mixed]	Experimental Value [mixed]
$P_{\text{in}}[kPa]$	566.0	568.5
$T_{\text{in}}[^{\circ}C]$	16.85	16.91
$\dot{m}[gmin^{-1}]$	50	50.2
$Q_{\text{heater}}[W]$	100	–

made from looking at the data presented and modeled in section 5, where it appears that the 3 μm parts have no reduction in thermal resistance compared to the plane walled test section. This discrepancy can be accounted for by slight differences in the inlet subcooling for each test. When the inlet subcooling is averaged across all tests for both the plane walled and 3 μm test sections, the plane walled parts have an average of 0.63 W less subcooling than the 3 μm parts. The 6 μm parts fall very close to the total average of 3.38 W. This increase in subcooling leads to a larger single-phase region, where the heat transfer coefficients are lower. However, more subcooling yields a lower outlet vapor quality for the same power input, which affects critical heat flux.

Next, from this study, it is shown that to reduce the thermal resistance of the test sections, both surface roughness and area enhancement factor should be increased as much as possible. This study only covers surface roughness up to 12 μm because that is the upper limit of roughness covered in the data set on which the Cooper correlation is based.

Next, because it appears there is some pressure drop cost associated with the introduction of the sawtooth pattern as shown in section 5, pressure drop is added to this study. Pressure drop through the plane walled part was calculated to be 31.0 kPa, and generally, pressure drop increased with both area enhancement and surface roughness R_{p}. The maximum pressure drop was found to occur in the 75° area enhanced parts with 12 μm feature height and was calculated to be 34.8 kPa. These pressure drop results are overlaid onto the optimization chart and shown in Figure 5.13.

It is important to note that these values do not correspond to the pressure drop measured in the test facility described in chapter 3 or even the full pressure drop through the test piece. This is because the majority of the pressure drop through the part comes from the inlet restriction (see

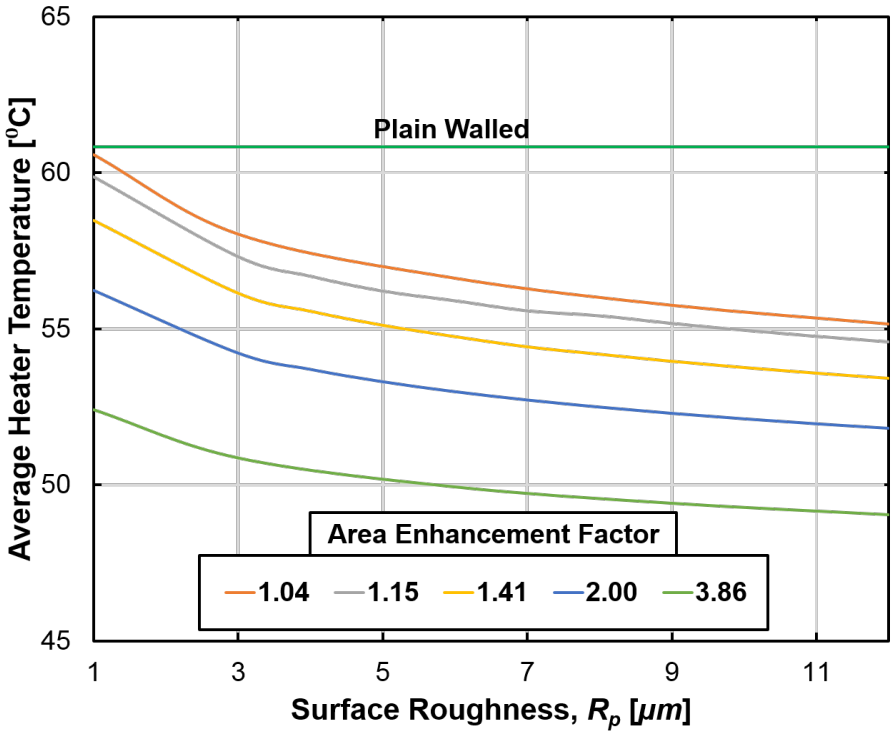

Figure 5.12: Average heater temperature shown as a function of surface roughness, R_{p} and area enhancement factor.

Figure 4.10) and the pressure drop measured in the facility includes the flow path upstream and downstream of the test section.

It is also interesting to examine the calculated pressure drops for the 45° area enhanced test sections with surface roughnesses of 3 μm and 6 μm as these correspond to the test physical test sections examined in section 5. The 3 μm and 6 μm test sections had calculated pressure drops 0.83 kPa and 1.52 kPai higher than the plane walled parts, respectively. The difference between the 3 μm and 6 μm calculated pressure drop falls within the bias uncertainty of the differential pressure transducer (0.028 kPa), so some difference should have been seen in the pressure drop data presented it section 5. The reason for the similarity shown there likely stems from slight differences in inlet subcooling.

Based on the data presented above as well as the findings from the data analysis, several conclusions can be drawn. There are also gaps in the current work that should be addressed. These will be presented in the following section.

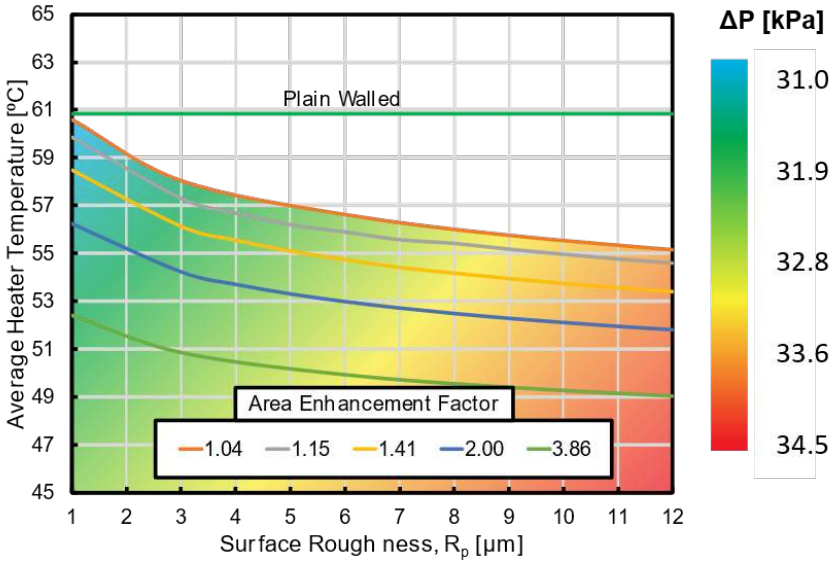

Figure 5.13: Optimization study as shown in Figure 5.12 with lines of constant pressure included.

Chapter 6: Summary and Recommendations

The current study is part of a multi-year project aimed at creating state of the art heat exchangers for laser diode arrays. By introducing effective thermal management strategies, laser diodes can be packaged with smaller pitches and operated at higher powers, both of which increase brightness. In these packages, heat fluxes can exceed 1 $\mathrm{kW\,cm^{-2}}$ and volumetric heat generation can exceed 10 $\mathrm{kW\,cm^{-3}}$. Current state of the art thermal management strategies employ single-phase microchannel heat sinks which absorb heat through sensible temperature rise. This has several drawbacks, including large thermal resistances and high fluid flow rates. Utilizing a two-phase fluid removes heat with a lower driving temperature difference and requires lower flow rates. These heat sinks have been shown to be viable in previous works but still face practical limitations. No prior investigations have shown surface structuring enhancement in microchannels with hydraulic diameters below 200 $\mu\mathrm{m}$ and none use high pressure refrigerants.

This study presents a novel surface enhancement scheme that increases the area available for heat transfer by 41% in a high aspect ratio (5:1), 67 $\mu\mathrm{m}$ hydraulic diameter microchannel array subjected to heat fluxes up to 1.3 $\mathrm{kW\,cm^{-2}}$. Test sections with 2 area enhancement schemes were compared to plain wall test sections under steady state conditions. The two area enhancement patterns differed only in feature height and pitch, the first with a 3 $\mu\mathrm{m}$ height and 6 $\mu\mathrm{m}$ pitch and the second with a 6 $\mu\mathrm{m}$ height and 12 $\mu\mathrm{m}$ pitch. The test sections measured 12 mm$\times$ 38 mm and contained 125 parallel 2 mm channels. The inlet to each channel contained a 15 $\mu\mathrm{m}$ wide$\times$ 150 $\mu\mathrm{m}$ long inlet restriction to promote flow stability. The heat load from the diode was simulated by a 1 mm wide$\times$ 10 mm long platinum joule heater.

The performance of the test sections were characterized with R134a in a custom test facility that allowed measurement and control of fluid temperature, pressure and mass flow rate. During each test, inlet conditions were set using a positive displacement gear pump, an accumulator and two heat exchangers coupled to a secondary coolant loop. Keeping the inlet conditions constant, power to the heater was increased to set the average heater temperature which was increased in 5$^{\circ}\mathrm{C}$

increments until critical heat flux was reached. A 17% decrease in thermal resistance is reported for the 6 μm test sections and both enhanced test sections achieved an increase in critical heat flux.

The experimental data was then input into a novel thermal FEA model to determine heat transfer behavior. This method, which models only the solid domain, solves for the temperature profile in a half channel geometry. To reduce the computational requirements of representing two-phase flow, the fluid is modeled as a local heat transfer coefficient referenced to a local fluid temperature. Several correlations available in the literature were surveyed and the correlation from Bertsch et. al. was the most robust. Using this correlation it was found that the performance difference could be accounted for surface roughness effects that promote bubble nucleation. The area enhancement effects were largely negated because the reduction in local heat flux led to lower heat transfer coefficients. Additionally, a modification is presented to the Bertsch correlation that indicates that nucleate boiling is present over a larger range of vapor qualities.

Finally, this model was used to survey alternate geometries. Sawtooth angles ranging from 15° to 75°, which correspond to area enhancements between 1.04× - 3.86×, were examined with feature heights between 1 μm and 12 μm. It was found that thermal resistance is decreased monotonically with increasing area enhancement and feature height with only a small increase in pressure drop.

6.1 Recommendations for Future Research

To further increase performance, better utilization of the channels upstream of the heater is required. To do this, a study of subcooling is needed. Both inlet temperature and mass flow should be varied to find the optimal degree of subcooling such that two-phase heat transfer is present over a larger portion of the channel. This cannot be done with the computational model because it does not capture flashing. The computational model predicts that greater area enhancements (steeper sawtooth angles) and larger feature sizes will further decrease thermal resistance. Particularly, an investigation of a 75°, 12 μm sawtooth pattern is warranted. It his predicted that this geometry will reduce thermal resistance of these already effective heat exchangers by 40% and verification of the

pressure drop prediction is necessary to ensure that operation is feasible. Because of the reduction in local heat flux, it is predicted that steeper sawtooth angles will also delay the onset of critical heat flux. Again, because the mode does not account for dryoutl, these suggested geometries should be tested to dryout incipience. Additionally, because because the DRIE etching process is not limited to etching straight lines, different area enhancement patterns, for example concave and convex teeth, can be tried. This will allow investigators to isolate the effect of number of nucleation sites from area enhancement factor, and pitch. Finally, it is likely that a poorly wetting fluid will separate from the nucleation sites more easily and frequently and have a beneficial effect of heat transfer rates.

References

[1] Matthias Pospiech and Sha Liu. Laser Diodes. (May), 2004.

[2] Taylor Bevis. *High Heat Flux Phase Change Thermal Management of Laser Diode Arrays*. Master, Colorado State University, 2016.

[3] Dler Adil Jameel. Thin Film Deposition Processes. 1(4):193–199, 2015.

[4] Xingsheng Liu, Wei Zhao, Lingling Xiong, and Hui Liu. *Packaging of High Power Semiconductor Lasers*. ir University of California, Santa Cruz, CA, 2015.

[5] Kuan-Yan Huang, Cheng-Kuo Su, Meng-Wei Lin, Yu-Chung Chiu, and Yen-Chieh Huang. Efficient 750-nm LED-pumped Nd:YAG laser. *Optics Express*, 24(11):12043, 2016.

[6] R Paschotta. Brightness, 2008.

[7] R Paschotta. Beam Radius, 2008.

[8] R Paschotta. Beam Divergence, 2008.

[9] R Paschotta. Beam Quality, 2008.

[10] Hagop Injeyan and Gregory Coddno. *High-Power Laser Handbook*. McGraw-Hill, 2001.

[11] C. Frevert, P. Crump, H. Wenzel, S. Knigge, F. Bugge, and G. Erbert. Efficiency optimization of high power diode lasers at low temperatures. *2013 Conference on Lasers and Electro-Optics Europe and International Quantum Electronics Conference, CLEO/Europe-IQEC 2013*, 791608(2011):824111, 2013.

[12] Michael Leers and Konstantin Boucke. Cooling approaches for high power diode laser bars. *Proceedings - Electronic Components and Technology Conference*, pages 1011–1016, 2008.

[13] J. A. Skidmore, B. L. Freitas, J. Crawford, J. Satariano, E. Utterback, L. DiMercurio, K. Cutter, and S. Sutton. Silicon monolithic microchannel-cooled laser diode array. *Applied Physics Letters*, 77(1):10–12, 2000.

[14] S. V. Sobhan and C. B. Garimella. *TRANSPORT IN MICROCHANNELS âĂŞ A CRITICAL REVIEW*. Begell House, 2003.

[15] Bryan Burk and Todd Bandhauer. Burk_et_al - IMECE 2017 - Final (1). In *ASME IMECE*, Tampa, Florida USA, 2017. ASME ICME.

[16] Robert Cole. Boiling Nucleation. *Advanced Heat Transfer*, 10:86–166, 1984.

[17] Cristiano Bigonha Tibiriçá and Gherhardt Ribatski. Flow patterns and bubble departure fundamental characteristics during flow boiling in microscale channels. 59:152–165, 2014.

[18] Cooper. Heat Flow Rates in Saturated Nucleate Pool Boiling-A Wide-Ranging Examination Using Reduced Properties 1 . *Advances in Heat Transfer*, 16:157–239, 1984.

[19] ISO. Geometrical Product Specifications (GPS) âĂŤ Surface texture: Profile method âĂŤ Terms, definitions and surface texture parameters, 1997.

[20] Y Y Hsu. On the Size Range of Active Nucleation Cavities on a Heating Surface. *Journal of Heat Transfer*, 84(3):207–213, 1962.

[21] C. J. Kuo and Y. Peles. Local measurement of flow boiling in structured surface microchannels. *International Journal of Heat and Mass Transfer*, 50(23-24):4513–4526, 2007.

[22] Satish G Kandlikar. History , Advances , and Challenges in Liquid Flow and Flow Boiling Heat Transfer in Microchannels : A Critical Review. *Journal of Heat Transfer*, 134, 2016.

[23] Tamanna Alam, Poh Seng Lee, and Christopher R. Yap. Investigation of flow boiling instabilities in silicon microgap heat sink. *Proceedings of the 2012 IEEE 14th Electronics Packaging Technology Conference, EPTC 2012*, pages 519–524, 2012.

[24] H. Y. Wu, Ping Cheng, and Hao Wang. Pressure drop and flow boiling instabilities in silicon microchannel heat sinks. *Journal of Micromechanics and Microengineering*, 16(10):2138–2146, 2006.

[25] Sung-min Kim and Issam Mudawar. International Journal of Heat and Mass Transfer Review of databases and predictive methods for heat transfer in condensing and boiling mini / micro-channel flows. *International Journal of Heat and Mass Transfer*, 77:627–652, 2014.

[26] S Szczukiewicz, M Magnini, and J R Thome. International Journal of Multiphase Flow Proposed models , ongoing experiments , and latest numerical simulations of microchannel two-phase flow boiling. *INTERNATIONAL JOURNAL OF MULTIPHASE FLOW*, 59:84–101, 2014.

[27] Jaeseon Lee and Issam Mudawar. Fluid flow and heat transfer characteristics of low temperature two-phase micro-channel heat sinks âĂŞ Part 2 . Subcooled boiling pressure drop and heat transfer. *International Journal of Heat and Mass Transfer*, 51:4327–4341, 2008.

[28] Y. Peles. Two-Phase Boiling Flow in Microchannels: Instabilities Issues and Flow Regime Mapping. In *ASME 2003 1st International Conference on Microchannels and Minichannels*, pages 559–566, Rochester, New York, USA,, 2003. ASME.

[29] G. Hetsroni, A. Mosyak, and Z. Segal. Nonuniform temperature distribution in electronic devices cooled by flow in parallel microchannels. *IEEE Transactions on Components and Packaging Technologies*, 24(1):16–23, 2001.

[30] Jung Eung Park, John R. Thome, and Bruno Michel. Effect of inlet orifice on saturated CHF and flow visualization in multi-microchannel heat sinks. *Annual IEEE Semiconductor Thermal Measurement and Management Symposium*, pages 1–8, 2009.

[31] Van P. Carey. *Liquid Vapor Phase Change Phenomena: An Introduction to the Thermophysics of Vaporization and Condensation Processes in Heat Transfer Equipment*. CRC Press, 2nd edition, 2007.

[32] Sung-min Kim and Issam Mudawar. International Journal of Heat and Mass Transfer Universal approach to predicting saturated flow boiling heat transfer in mini / micro-channels

âĂŞ Part I . Dryout incipience quality. *International Journal of Heat and Mass Transfer*, 64:1226–1238, 2013.

[33] S.S. Kutateladze and A.I. Leont'ev. Some applications of the asymptotic theory of the turbulent boundary layer. In *3rd Int. Heat Transfer Conf.*, pages 1–6, Chicago, Illinois, 1966.

[34] W. Hebel, W. Detavernier, and M. Decreton. A contribution to the hydrodynamics of boiling crisis in a forced flow of water. *Nucl. Eng. Des.*, 64:443–445, 1981.

[35] C.H. Lee and I. Mudawar. A mechanistic critical heat flux model for subcooled flow boiling based on local bulk flow conditions 14 (1988). *Int. J. Multiphase Flow*, 14:711–728., 1988.

[36] C.O. Cersey and I. Mudawar. Effects of heater length and orientation on the trigger mechanism for near-saturated flow boiling critical heat flux âĂŞ I. Photographic study and statistical characterization of the near-wall interfacial features. *Int. J. Heat Mass Transfe*, (38):629–641, 1995.

[37] X. Huo, L. Chen, Y. S. Tian, and T. G. Karayiannis. Flow boiling and flow regimes in small diameter tubes. *Applied Thermal Engineering*, 24(8-9):1225–1239, 2004.

[38] Stefan S Bertsch, Eckhard A Groll, and Suresh V Garimella. International Journal of Multiphase Flow Effects of heat flux , mass flux , vapor quality , and saturation temperature on flow boiling heat transfer in microchannels. *International Journal of Multiphase Flow*, 35(2):142–154, 2009.

[39] Stefan S Bertsch, Eckhard A Groll, and Suresh V Garimella. Refrigerant flow boiling heat transfer in parallel microchannels as a function of local vapor quality. *International Journal of Heat and Mass Transfer*, 51:4775–4787, 2008.

[40] Z. Liu and R.H.S. Winterton. A General Correlation for Saturated and Subcooled Flow Boiling in Tubes and Annuli, Based on a Nucleate Pool Boiling Equation. *International Journal of Heat and Mass Transfer1*, 34:2759–2766, 1991.

[41] K.E. Gungor and R.H.S. Winterton. A General CCorrelation for Flow Boiling in Tubes and Annuli. *International Journal of Heat and Mass Transfer1*, 29:351–358, 1986.

[42] D.M. Wambsganss, J.A. France, and T.N. Jendraejczyk. Boiling Heat Transfer in a Horizontal Small-Diameter Tube. *Journal of Heat Transfer1*, 115:963–972, 1993.

[43] Z.Y. Bao, D.F. Fletcher, and B.F. Haynes. No , Flow boiling heat transfer of Freon R11 and HCFC123 in narrow passages,. *International Journal of Heat and Mass Transfer2*, 43(3347-3358), 2000.

[44] G M Lazarek and S H Black. Evaporative heat transfer, pressure drop and critical heat flux in a small vertical tube with R-113. *International Journal of Heat and Mass Transfer*, 25:945–960, 1982.

[45] T N Tran, M W Wambsganss, and D M France. Small circular- and rectangular-channel boiling with two refrigerants. *International Journal of Multiphase Flow1*, 22(485-498), 1996.

[46] Y.Y. Yan and T.F. Lin. Evaporation heat transfer and pressure drop of refrigerant R-134a in a small pipe. *International Journal of Heat and Mass Transfer*, 41:4183–4194, 1998.

[47] V.V. Wadekar. Flow boiling of heptane in a plate-fin heat exchanger passage. *ASME HTD*, 201:1–6, 1992.

[48] Ali Kosar, Chih-Jung Kuo, and Yoav Peles. Suppression of Boiling Flow Oscillations in Parallel Microchannels by Inlet. *Journal*, 128(March 2006):251–260, 2006.

[49] Vikash Khanikar, Issam Mudawar, and Timothy Fisher. Flow boiling in a micro-channel coated with carbon nanotubes. *2008 11th Intersociety Conference on Thermal and Thermo-mechanical Phenomena in Electronic Systems*, pages 960–969, 2008.

[50] I Pranoto, C Yang, L X Zheng, K C Leong, and P K Chan. Flow Boiling Heat Transfer Enhancement from Carbon Nanotube- Enhanced Surfaces. *Defect and Diffusion Forum*, 348:20–26, 2014.

[51] Chih Jung Kuo, Ali KoÅ§ar, Yoav Peles, Steven Virost, Chandan Mishra, and Michael K. Jensen. Bubble dynamics during boiling in enhanced surface microchannels. *Journal of Microelectromechanical Systems*, 15(6):1514–1527, 2006.

[52] Yifan Li, Guodong Xia, Yuting Jia, Yue Cheng, and Jun Wang. Experimental investigation of flow boiling performance in microchannels with and without triangular cavities âĂŞ A comparative study. *International Journal of Heat and Mass Transfer*, 108:1511–1526, 2017.

[53] Santosh Krishnamurthy and Yoav Peles. Flow Boiling Heat Transfer on Micro Pin Fins Entrenched in a Microchannel. *Journal of Heat Transfer*, 132(4):041007, 2010.

[54] Bin He, Mengyao Wei, Sivanand Somasundaram, Chuan Seng Tan, and Evelyn N. Wang. Experiments on the ultrathin silicon vapor chamber for enhanced heat transfer performance. *Proceedings of the 15th InterSociety Conference on Thermal and Thermomechanical Phenomena in Electronic Systems, ITherm 2016*, pages 569–573, 2016.

[55] Steven A Isaacs. Two-Phase Flow and Heat Transfer in Pin-Fin Enhanced Micro-Gaps With Non-Uniform Heating. *Proceedings of the ASME 2013 4th International Conference on Micro/Nanoscale Heat and Mass Transfer*, pages 4–10, 2012.

[56] Corey Woodcock, Farzad Houshmand, Joel Plawsky, Michael Izenson, David Fogg, Roger Hill, Scott Phillips, and Yoav Peles. Piranha Pin-Fins (PPF): Voracious boiling heat transfer by vapor venting from microchannels -System calibration and single-phase fluid dynamics. *Thermomechanical Phenomena in Electronic Systems -Proceedings of the Intersociety Conference*, pages 282–289, 2014.

[57] Xiangfei Yu, Corey Woodcock, Yingying Wang, Joel Plawsky, and Yoav Peles. A Comparative Study on Flow Boiling in Microchannel With Piranha Pin Fin. *InterPACK/ICNMM 2015*, 138(November):V003T10A005–V003T10A005, 2015.

[58] X Yu, C Woodcock, J Plawsky, and Y Peles. International Journal of Heat and Mass Transfer An investigation of convective heat transfer in microchannel with Piranha Pin Fin. *International Journal of Heat and Mass Transfer*, 103:1125–1132, 2016.

[59] Stephen D. Senturia. *Microsystem Design*. Springer, New York, 1st edition, 2000.

[60] Bryan E. Burk. *A COMPUTATIONAL EXAMINATION OF CONJUGATE HEAT TRANSFER DURING MICROCHANNEL FLOW BOILING USING FINITE ELEMENT ANALYSIS*. Masters, Colorado State University, 2018.

[61] Poh-seng Lee and Suresh V Garimella. Saturated flow boiling heat transfer and pressure drop in silicon microchannel arrays. 51:789–806, 2008.

[62] R. K. Shah A. L. London. *Laminar Flow Forced Convection in Ducts*. Academic Press, 1st edition, 1978.

[63] David Copeland, Masud Behnia, and Wataru Nakayama. Manifold microchannel heat sinks: Isothermal analysis. *IEEE Transactions on Components Packaging and Manufacturing Technology Part A*, 20(2):96–102, 1997.

[64] Sung-min Kim and Issam Mudawar. International Journal of Heat and Mass Transfer Consolidated method to predicting pressure drop and heat transfer coefficient for both subcooled and saturated flow boiling in micro-channel heat sinks. *International Journal of Heat and Mass Transfer*, 55(13-14):3720–3731, 2012.

[65] Stefan S Bertsch, Eckhard A Groll, and Suresh V Garimella. International Journal of Heat and Mass Transfer A composite heat transfer correlation for saturated flow boiling in small channels. *International Journal of Heat and Mass Transfer*, 52(7-8):2110–2118, 2009.

[66] Stefan Bertsch and Eckhard A Groll. Review and Comparative Analysis of Studies on Saturated Flow Boiling in Small Channels ,. *CTRC Research Publications*, 2008.

[67] Sung-min Kim and Issam Mudawar. International Journal of Heat and Mass Transfer Universal approach to predicting saturated flow boiling heat transfer in mini / micro-channels âĂŞ Part II . Two-phase heat transfer coefficient. *International Journal of Heat and Mass Transfer*, 64:1239–1256, 2013.

[68] G M Lazarek and S H Black. EVAPORATIVE HEAT TRANSFER , PRESSURE DROP AND CRITICAL HEAT FLUX IN A SMALL VERTICAL TUBE WITH R-l 13. 25(7), 1982.

[69] R Tillner-Roth and H.D. Baehr. An International Standard Formulation for the Thermodynamic Properties of 1,1,1,2-Tetrafluoroethane (HFC-134a) for Temperatures from 170 K to 455 K and Pressures up to 70 MPa,. *Journal of Physical Chemistry*, 23(5), 1994.

[70] Marcia Huber, Arno Laesecke, and Richard Perkins. Correlation for Viscosity of R134a. *Industrial Engineering and Chemistry Research*, 2003.

[71] M.J. Assael, N.K. Dalaouti, A.A. Griva, and J.H. Dymond. Viscosity and Thermal Conductivity of Halogenated Methane and Ethane Refrigerants. *International Journal of Refrigeration*, 22:525–535, 1999.

[72] NIST TN 1297: Appendix B. Coverage Factors, 2015.

[73] S.W. Churchill. *Friction-factor equation spans all fluid flow regimes*. 1977.

[74] Fchart. Engineering Equation Solver, 2017.

[75] Crane Co. Flow of fluids through valves, fittings and pipes, 1979.

[76] F.W. Dittus and K.M. Boelter. Heat Transfer in Automobile Radiators of the Tubular Type. 12:3–22, 1985.

Appendix A: Equipment List

This section provides a full list of the equipment used in the construction of the test facility. The equipment is divided into two sections for clarity: devices such as flow control and power supply, and sensors.

Table A.1: Test facility equipment list.

Item	Description	Manufacturer	Part Number
Gear Pump Head (High Flow)	GA series - T32 gear set (0.092 ml/rev) PEEK	MicroPump	GA-T32
Gear Pump Console Drive	50-5000 rpm; A-Mount Console Drive	MicroPump	wu-75211-10
Accumulator	Air/Water Bladder Cylinder	Accumulators, Inc.	A1F5002BNP
Vacuum Pump	High Vacuum; 15 micron; 3 cfm	McMaster	4396K21
Chiller	Merlin M150LR w/ CP 55 pump, 3.5 kW cooling, 0.5 gal res	Thermofisher	M150LR-CP55
Heat Exchanger	Compact Plate Heat Exchanger	Koolance	HXP-193
Power Supply	DC Power Supply; 360W (60V/6A)	Instek	SPS-606

Table A.2: Test facility sensor list.

Item	Description	Manufacturer	Part Number
IR Pyrometer	Non-contact IR; Spot 0.9mm; Range 50-975C	MicroEpsilon	CTL-CF1-C8
Thermocouples	Type K; 0.5" length; Pipe process ungrounded	Omega	TC-K-NPT-UG-72
	Type T; 0.5" length; Pipe process ungrounded	Omega	TC-T-NPT-UG-72
	Type T; Surface mount adhesive backed	Omega	SA1XL-T
Flow Meter	Coriolis flow meter; 8-600g/min <0.5% accuracy	Rheonik	RHM015
	Coriolis flow transmitter; RS232 interface	Rheonik	RHE07
Pressure Transducers	0-50psia; 0.08% accuracy; 4-20 mA; 1/4" NPT	Omega	PX409-005AI
	0-100psia; 0.08% accuracy; 4-20 mA; 1/4" NPT	Omega	MMA100C1P3C0T4A6
	50 psid; 121degC max; 0.08% Accuracy	Omega	PX409-100DWUI
Shunt Resistor	10A, 1V, 0.1 ohm <0.01% accuracy	Ohm-Labs	CS-10
Data Aquisition System	4-slot USB Chassis	National Instruments	cDAQ-9174
	Thermocouple module; 16ch	National Instruments	NI 9214
	Analog current and voltage +/-10V; +/-21.5mA; 16ch	National Instruments	NI 9207
	Analog voltage +/-60V; 8ch	National Instruments	NI 9221

Appendix B: Calibration

All temperature measurement systems were calibrated to a high accuracy standard before the tests were completed. The pressure transducers, flow meter and data acquisition systems were provided with NIST traceable calibration records. The thermocouples and pyrometer were not calibrated from the manufacturer. To reduce bias error, these were calibrated against a Fluke 5615 platinum resistance device with an accuracy of $\pm$ 0.0012°C . The process thermocouples were calibrated in a PolyScience MX7L heated recirculating bath as described in section B.2. The pyrometer was calibrated in a oven as described in section B.1.

B.1 Pyrometer

A custom oven was constructed to calibrate the IR pyrometer. The test piece was installed in the wiring harness and kept at the same temperature as the high accuracy standard. During measurements, a window into the oven was briefly opened for the pyrometer to make a measurement. This setup can be seen in Figure B.1. Before test data could be collected to produce a calibration curve, a sensitivity study was performed to determine which factors influenced the pyrometer's readings. The parameters tested for in this study were angle relative to the test piece, distance from the test section, ambient lighting and surface temperature of the pyrometer. For the sensitivity study, the furnace was allowed to reach steady state and then the sliding door was opened for 5 seconds to collect data. A T-test and a analysis of variance test were performed to determine the significance of the results which are summarized in Table B.1.

From these results, both the analysis of variance and T-test determine that the deviation in test groups was not significant. This means that only a single calibration curve is needed if the surface temperature of the pyrometer is kept at 20°C . To accomplish this, a cooling jacket, coupled with a second chiller, is attached to the pyrometer face. This is shown in Figure B.2.

Once it was determined that a single calibration would be sufficient, a calibration curve was generated for four temperatures: 30.84°C , 65.95°C , 92.44°C , and 123.1 °C . These temperatures cover the range of surface temperatures expected during testing. The test section used in

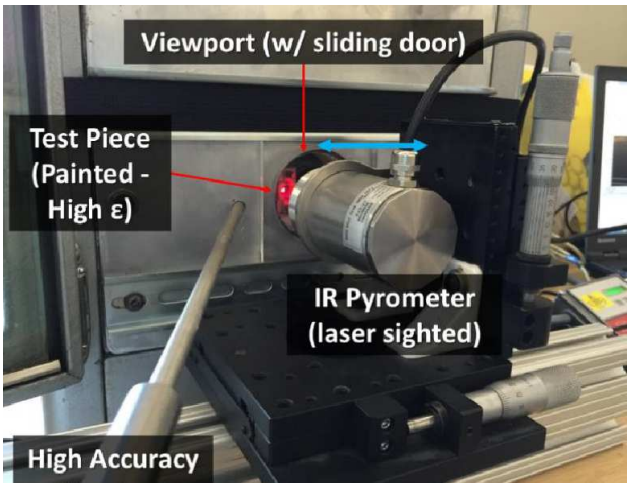

Figure B.1: View of pyrometer calibration oven with high accuracy standard

Table B.1: Statistical significance test for pyrometer under various conditions.

Description	N Data Points	Mean Difference	Deviation from Normal	Variance
Normal	9	1.036	0	0.037
Base Material	9	1.115	0.078	0.022
Close	4	1.196	0.159	0.023
Far	4	1.020	-0.016	0.007
Dark	5	1.102	0.066	0.062
Light	5	1.036	-0.001.	0.056
CW Angle (20°)	5	1.237	0.200	0.063
CW Angle (20°)	4	1.030	-0.007	0.018

the calibration was coated in high emisivity paint as done during testing. To reduce temperature fluctuations in the oven, the sliding door was kept open for the entire calibration. However, the cooling jacket kept the pyrometer's surface temperature at $20°\mathrm{C} \pm 0.29°\mathrm{C}$. Again, steady state was reached at each temperature and 100 data points were taken. The total bias error resulting from this calibration was $\pm\, 0.971°\mathrm{C}$. Because the calibration is done on the test piece in situ, no correction for emissivity or reflectivity is necessary. The test piece installed in the calibration oven is shown in Figure B.3.

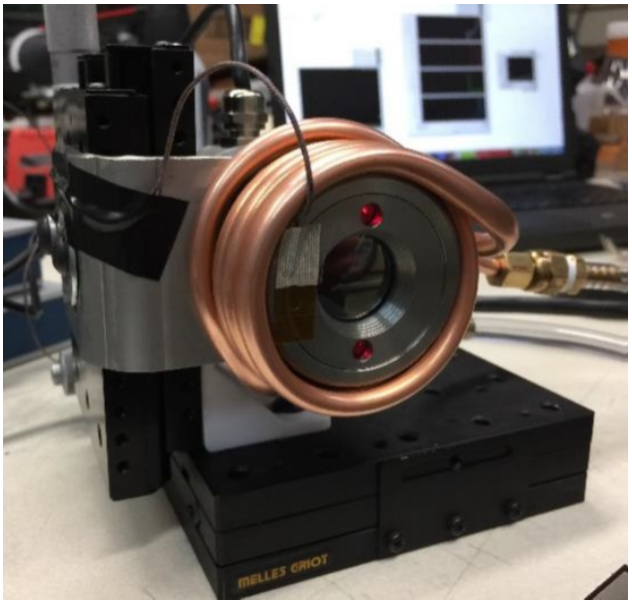

Figure B.2: Pyrometer cooling jacket to control surface temperature.

B.2 Thermocouples

All the thermocouples, both process and surface, were calibrated prior to use. The thermocouples were placed in contact with the Fluke RTD and placed in the calibration oven with the door closed. five temperature points were collected in the oven and 100 data points were taken at each temperature. The five set points were 40.92°C, 81.93°C, 134.9°C, 160.7°C, and 211.5°C. An additional calibration point was collected for the process thermocouples in the PolyScience oil bath at 5.0°C. This calibration achieved a total bias error of $\pm$ 0.233°C.

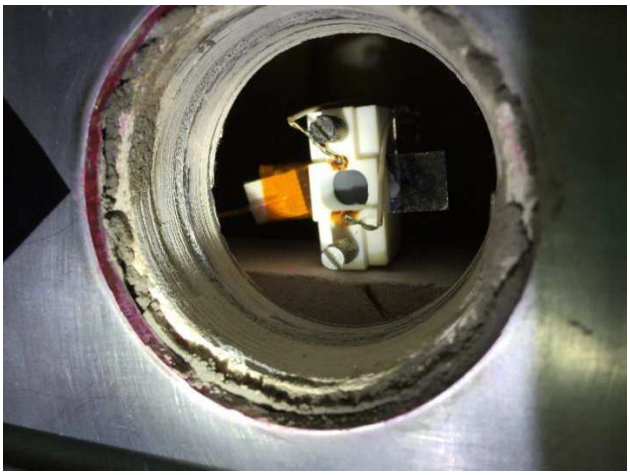

Figure B.3: Test section installed in electrical harness in calibration oven.

Appendix C: Uncertainty

For this study, all experimental results are shown with error bars to represent uncertainty. These error bars represent a 95 percent confidence interval and, because the data shown is an average of several tests, the total uncertainty is calculated as the superpostition of bias error and random sampling error. This section explains how these errors are calculated and provides an example calculation for a single data point on the thermal resistance chart presented later in section 5 where the uncertainty of the heater temperature and heater input power are shown. The formula for total measurement uncertainty *U* is presented in equation C.1 where *B* is the total bias error and *P* is the total random error.

$$U = \sqrt{B^2 + P^2} \tag{C.1}$$

The total bias error is a function of the uncertainty inherent in the sensors used. In this study, many of the sensors have been calibrated against a high accuracy standard and as a result have a lower uncertainty than the factory reported bias. The formula for total bias error is shown in equation C.2:

$$B = \sqrt{B_{\mathrm{cs}}^2 + (K \cdot SEE)^2} \tag{C.2}$$

In equation C.2, B_{cs} refers to the bias of the high accuracy standard used to calibrate the sensor, K is the Student T Coverage Factor found from coverage factor Table [72] and is found for a two-tailed confidence level of 95 percent. Finally, *SEE* is the standard error of estimation, which comes from the calibration and is given in equation C.3.

$$SEE = \sqrt{\frac{\sum_{\mathrm{i}=1}^{n} [Y_{\mathrm{i}} - X_{\mathrm{i}}]^2}{N - 2}} \tag{C.3}$$

where X_{i} is the sensor reading with the calibration applied and Y_{i} is the reading from the high accuracy standard.

Next, in order to complete equation C.1, the random sampling error is needed. This error comes from the differences between each test and, generally, as more experiments are performed, is reduced. The formula for *P* is shown in equation C.4:

$$P = K\frac{S_{\mathrm{x}}}{\sqrt{N}} \tag{C.4}$$

where *K* is again the two tailed, 95 percent confidence coverage factor, *N* is the total number of tests and S_{x} is the standard deviation shown in equation C.5:

$$S_{\mathrm{x}} = \Big[\frac{1}{N}\sum_{\mathrm{i}=1}^{N}(X_{\mathrm{i}} - \bar{X})^2\Big]^{1/2} \tag{C.5}$$

where X_{i} is the test value and $\bar{X}$ is the average value for all the tests.

Next, it is important to follow error propagation for values that are not measured directly. In this case, the heater input power is calculated from the applied voltage measured across the test section and the voltage drop across a high accuracy shunt resistor. Because of this, the uncertainty of the input power measurement depends on the uncertainty of both voltage measurements as well as the uncertainty in the resistance value of the shunt. Error propagation was tracked using Engineering Equation Solver and the formula is present in equation C.6 where uncertainty U_{y} is calculated for the value y, which is a function of x_1 through x_{n}:

$$U_{\mathrm{y}} = \sqrt{\sum_{\mathrm{i}=1}^{n}\Big(\frac{\partial y}{\partial x_{\mathrm{i}}}\Big)^2 U_{\mathrm{x_i}}^2} \tag{C.6}$$

where $\frac{\partial y}{\partial x_{\mathrm{i}}}$ is the partial differential of y with respect to x_{i}.

Following the presentation of the equations used to calculated uncertainty, an example calculation follows for the plane walled test section in which the target temperature was 55°C . The average values about which uncertainty are calculated are shown in Table C.1 which are taken from 3 separate tests.

Table C.1: Average values for heater temperature and input power for the 55°C plane walled case.

Heater Temperature [°C]	Input Power [*W*]
54.13	83.84

Starting with the heater temperature, which is measured using the calibrated infrared pyromter, the bias uncertainty for the heater temperature measurement can be found. The fluke thermistor used as the calibration standard has a published bias of B_{cs} = 0.0012°C. The calibration of the pyromter produced a calibration curve with a gain of 0.994 and an offset of 3.39. More information on the calibration of the pyrometer can be found in section B.1. While this is calculated for all data points to find the standard error of estimation, only 3 calibration points are shown in Table C.2 for clarity.

Table C.2: Pyrometer calibration used to calculated *SEE* for bias uncertainty.

Calibrated Standard [°C]	Raw Sensor [°C]	Corrected Sensor [°C]
30.76	26.49	29.74
65.15	65.15	65.97
91.61	91.61	91.55

From the data found presented Table C.2 the standard error of estimation from equation C.3 is found to be:

$$\begin{aligned} \sum_{\mathrm{i}=1}^{n}[Y_{\mathrm{i}} - X_{\mathrm{i}}]^2 &= 1.712^{\circ}\mathrm{C}] \\ SEE &= \sqrt{\frac{1.712}{1}} \\ SEE &= 1.31[^{\circ}\mathrm{C}] \end{aligned} \tag{C.7}$$

The actual standard error of estimation, which was calculated using more calibration points, was found to be 0.68°C . Now, using a *K* coverage factor of 1.96 for the large number of samples taken at each data point, the total bias error can be calculated as shown in C.8.

$$\begin{aligned} B &= \sqrt{B_{\text{cs}}^2 + (k \cdot SEE)^2} \\ B &= \sqrt{0.0012^2 + (1.96 \cdot 0.68)^2} \\ B &= 1.31[^{\circ}\text{C}] \end{aligned} \tag{C.8}$$

Next, the random error, P, is found for the heater temperature. A random error calculation will not be shown for input power as it is very similar. The 3 data points used to find the average are shown in Table C.3.

Table C.3: 3 heater temperature data points for the 55°C case.

Trial	Heater Temperature [°C]
1	52.81
2	54.67
3	54.89

Using the data presented in Table C.3, as well as a *K* coverage factor of 2.78 for a 95 percent confidence interval with only 3 data points, the random error, P is calculated in C.9. The standard deviation of this sample, S_{x}, is 0.94°C.

$$\begin{aligned} P &= K\frac{S_{\text{x}}}{\sqrt{N}} \\ P &= 2.78\frac{0.94}{3} \\ P &= 0.19^{\circ}\text{C}] \end{aligned} \tag{C.9}$$

Finally, using the values from C.8 and C.9, the total uncertainty can be calculated in C.10, where it is shown that the total uncertainty is almost equal to the bias uncertainty.

$$
\begin{aligned}
U &= \sqrt{B^2 + P^2} \\
U &= \sqrt{0.67^2 + 0.19^2} \\
U &= 1.34^{\circ}\mathrm{C}] \\
U_{\pm} &= 0.66[^{\circ}\mathrm{C}]
\end{aligned}
\tag{C.10}
$$

Next, an example calculation for the error propagation in input power is shown. The input power is calculated from the voltage drop across the device, and the voltage drop across an inline resistor with a known resistance as shown in equation C.11:

$$
\begin{aligned}
I &= \frac{V_{\text{shunt}}}{R_{\text{shunt}}} \\
Q_{\text{heater}} &= V_{\text{heater}} \cdot I \\
Q_{\text{heater}} &= \frac{V_{\text{shunt}}}{R_{\text{shunt}}} V_{\text{heater}}
\end{aligned}
\tag{C.11}
$$

where I is the current through both the shunt resistor and heater element, V_{shunt} is the voltage drop across the shunt resistor, R_{shunt} is the resitance of the shunt and V_{heater} is the voltage drop across the test piece. Because no calibration is performed for the data acquisition device reading V_{shunt} and V_{heater}, the manufacturer bias errors are used which are 0.52% and 0.26% of the value, respectively. Additionally, the resistance of the shunt is known within 0.01%. Taking the partial derivatives of Q_{heater} with respect to V_{shunt}, R_{shunt} and V_{heater} yields:

$$
\begin{aligned}
\frac{\partial Q_{\text{heater}}}{\partial V_{\text{shunt}}} &= \frac{1}{R_{\text{shunt}}} V_{\text{heater}} \\
\frac{\partial Q_{\text{heater}}}{\partial R_{\text{shunt}}} &= -\frac{V_{\text{shunt}}}{R_{\text{shunt}}^2} V_{\text{heater}} \\
\frac{\partial Q_{\text{heater}}}{\partial V_{\text{heater}}} &= \frac{V_{\text{shunt}}}{R_{\text{shunt}}}
\end{aligned}
\tag{C.12}
$$

Now, values can be input for each trial into equation C.12. Values for V_{shunt}, R_{shunt} and V_{heater} are shown for trial 1 in Table C.4.

These values are plugged into C.12 which yields the following:

Table C.4: Voltage and resistor values from the 55°C plane walled case to demonstrate error propagation.

V_{shunt} [V]	R_{shunt} [Ω]	V_{heater} [V]
0.304	0.1	27.36

$$\begin{aligned}
\frac{\partial Q_{\text{heater}}}{\partial V_{\text{shunt}}} &= \frac{1}{0.1} \cdot 27.36 \\
\frac{\partial Q_{\text{heater}}}{\partial V_{\text{shunt}}} &= 273.6[\text{A}] \\
\frac{\partial Q_{\text{heater}}}{\partial R_{\text{shunt}}} &= -\frac{0.304}{0.1^2} \cdot 27.36 \\
\frac{\partial Q_{\text{heater}}}{\partial R_{\text{shunt}}} &= -831.7[\frac{1}{\Omega^2}] \\
\frac{\partial Q_{\text{heater}}}{\partial V_{\text{heater}}} &= \frac{0.304}{0.1} \\
\frac{\partial Q_{\text{heater}}}{\partial V_{\text{heater}}} &= 3.04[\text{A}]
\end{aligned} \tag{C.13}$$

Next, these can be combined with the uncertainties for each measurement into equation C.6 to find the total bias uncertainty for the power measurement.

$$\begin{aligned}
U_{\text{power}} &= \sqrt{273.6^2 \cdot 0.0016^2 + (-831.7)^2 \cdot (1 \times 10^{-5})^2 + 3.04^2 \cdot 0.071^2} \\
U_{\text{power}} &= 0.49[\text{W}]
\end{aligned} \tag{C.14}$$

Finally, the total uncertainty can be added to this data point as T_{heater} = 54.12°C $\pm$ 0.66°C and Q_{heater} = 83.84 W $\pm$ 0.63 W. Note that the random error has been added into the input power uncertainty although this calculation is not shown.

Appendix D: Pressure Drop Equations Through Test Section

In this section, a detailed list of the equations used to determine channel inlet pressure is given. As mentioned in Section 4.2.1, single-phase pressure drop is calculated through the 23 discrete elements and then summed to find the pressure drop through the test section orifice. This in turn is used to find the channel inlet pressure during the two-phase tests.

For each section, total pressure drop is calculated as the sum of major (frictional) and minor losses as shown in Equation D.1.

$$\Delta P_{\text{total}} = \Delta P_{\text{friction}} + \Delta P_{\text{minor}} \tag{D.1}$$

Frictional losses are given in the standard form:

$$\Delta P_{\text{friction}} = \frac{1}{2}\rho v^2 f \frac{L}{D_{\text{h}}} \tag{D.2}$$

where f is the friction factor. For all sections with a circular cross-section, the friction factor is determined from the Churchill equation [73] given in equation D.3, where surface roughness, ϵ is assumed to be zero for all cases where it is unknown.

$$\begin{aligned} f &= \left[\left(\frac{8}{Re}\right)^{12} + \frac{1}{(A+B)^{3/2}}\right]^{-1/12} \\ A &= \left[2.457ln\left(\frac{1}{7/\text{Re}}\right)^{0.9} + .27\frac{\epsilon}{D_{\text{h}}})\right]^{16} \\ B &= \left[\frac{37530}{Re}\right]^{16} \end{aligned} \tag{D.3}$$

For pressure drop in the channels, the Shah and London friction factor, shown in equation D.4 is used because it was specifically designed for laminar flow in small channels.

$$f = \frac{96}{Re}\left[1 - 1.3553\beta + 1.9467\beta^2 - 1.7012\beta^3 + 0.9564\beta^4 - 0.2537\beta^5\right] \tag{D.4}$$

To calculate the minor loss coefficients, standard equations found in EES [74] are used. All minor losses in this calculation can be divided into five categories: sudden expansion, gradual expansion, miter bend, gradual contraction and sudden contraction. Formulations for these are defined in [75].

Appendix E: Parasitic Heat Losses

In this section, heat transfer to and from the surroundings is analyzed. As mentioned in chapter 3, there is roughly 4 ft. of insulated pipe between the upstream and downstream thermocouple. Because the fluid in this region is cooler than the lab space (15°C as compared to 23°C), heat from the room is transferred to the fluid. Likewise, because the test section temperature is raised up to 65°C, heat is transferred from the test section to the environment. However, because this transfer is driven by natural convection and the test facility is generally well insulated, these heat transfer rates may be small relative to the heat transfer rates within the test section. This section investigates if these losses are large enough to require consideration.

For this analysis, the test facility between the thermocouples is divided into 7 sections as shown in Figure E.1. Sections 1 and 7 are braided steel coated PTFE tubing insulated in Buna-N foam. Sections 2 and 6 are teflon sight tubes again insulated in foam. 3 and 5 constitute the peek manifold. Section 4 is the actual silicon test section. For this analysis the worst case scenario is analyzed in which the entire section is assumed to be at the highest heater temperature, 65°C .

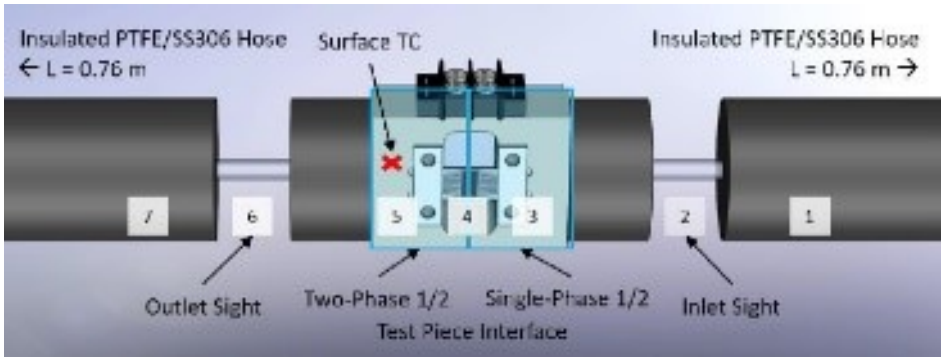

Figure E.1: Test section used for quantify heat loss.

A cross section of regions 1 and 7 is shown in Figure E.2. Because the thickness of the PTFE is not published, it is ignored and the entire thickness is assumed to be stainless steel. Stainless steel has a higher thermal conductivity which makes this a conservative assumption. The geometric parameters are listed in Table E.1.

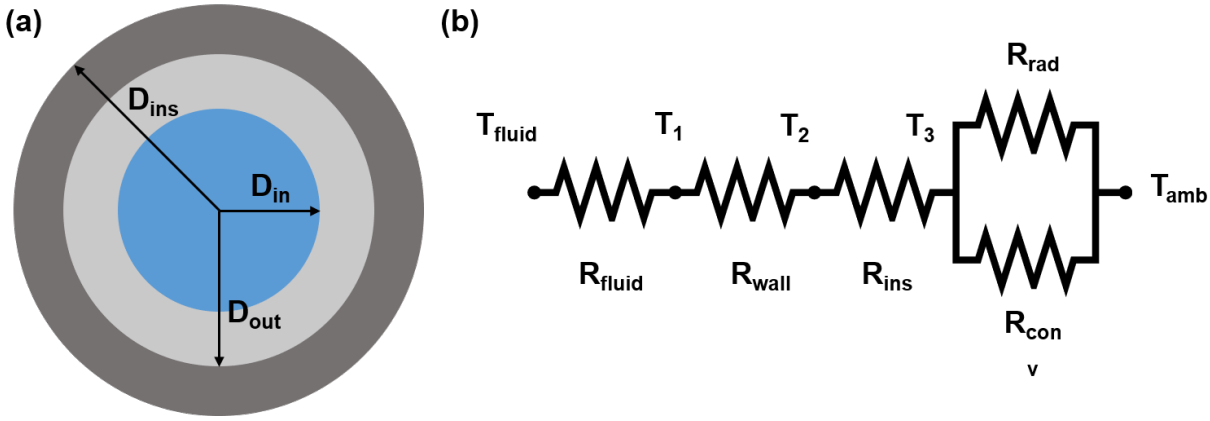

Figure E.2: Cross section of regions 1 and 7 with corresponding thermal resistance network

Table E.1: Region 1 and 7 geometric parameters.

Description	Label	Value [mm]
Inner Diamter	$D_{\text{in},1}$	6.4
Tubing Diameter	$D_{\text{out},1}$	9.5
Insulation Diameter	D_{ins}	47.6

Taking the thermal resistance network from Figure E.2, we get equation E.1.

$$R_{\text{th}} = R_{\text{fluid},1} + R_{\text{ss}} + R_{\text{ins}} + \frac{R_{\text{conv}} \cdot R_{\text{rad}}}{R_{\text{conv}} + R_{\text{rad}}} \tag{E.1}$$

First the convection resistance between the fluid is calculated using equation E.2.

$$R_{\text{fluid}} = \frac{1}{h_{\text{fluid}} A} \tag{E.2}$$

where h_{fluid} is calculated using the Dittus-Bolter Equation [76] in equation E.3 using properties for saturated R134a liquid and a mass flow rate of 50 $\mathrm{g min^{-1}}$.

$$\begin{aligned} h_{\text{fluid}} &= \left(\frac{k}{D}\right) = 0.023 Re^{4/5} Pr 2/5 \\ Re &= \frac{\rho u D}{mu} \\ &= \frac{1257[\mathrm{kg\,m^{-3}}]0.021[\mathrm{m\,s^{-1}}]0.00635[\mathrm{m}]}{0.000234[\mathrm{kg\,m^{-1}s^{-1}}]} \\ &= 723 \\ h_{\text{fluid}} &= \left(\frac{0.0897[\mathrm{W\,m^{-1}K^{-1}}]}{0.00635\mathrm{m}}\right) 0.023\big(723\big)^{(}4/5\big(3.53\big)^{2/5} \\ &= 104.3[\mathrm{W\,m^{-2}K^{-1}}] \end{aligned} \tag{E.3}$$

This can be plugged back into equation E.2 to calculate the thermal resistance between the fluid and tube wall as in equation E.4.

$$\begin{aligned} R_{\text{fluid}} &= \frac{1}{\big(104.3[\mathrm{W\,m^{-2}K^{-1}}]\big) \cdot \big(0.0152[m^2]\big)} \\ &= 0.6309[\mathrm{K\,W^{-1}}] \end{aligned} \tag{E.4}$$

Next, the conduction resistance through the stainless steel is calculated using the formula for radial conduction shown in equation E.5.

$$\begin{aligned} R_{\text{ss}} &= \frac{ln\left(\frac{D_{\text{out}}}{D_{\text{in}}}\right)}{2\pi\big(D_{\text{out}} - D_{\text{in}}\big)k} \\ &= \frac{ln\left(\frac{0.00953[\mathrm{m}]}{0.00635[\mathrm{m}]}\right)}{2\pi\big(0.00953[\mathrm{m}] - 0.00635[\mathrm{m}]\big)13.2[\mathrm{W\,m^{-1}K^{-1}}]} \end{aligned} \tag{E.5}$$

Similarly, using a thermal conductivity of 0.036 $\mathrm{W\,m^{-1}K^{-1}}$, the thermal resistance of the Buna-N foam is calculated to be R_{ins} = 186.7 $\mathrm{KW^{-1}}$. To calculate the thermal resistance to the air,

a correlation is used to find the natural convection heat transfer coefficient between the air and a horizontal cylinder [76] which is shown in equation E.6.

$$h = \left(\frac{k}{D}\right)\left[0.6 + \frac{0.387 \cdot Ra^{1/6}}{\left(1 + \left(\frac{0.559}{Pr}\right)^{9/16}\right)^{8/27}}\right]^2 \tag{E.6}$$

The Prandtl number for air at 23°C is 0.71 but it is more difficult to find the Rayleigh number which is given by equation E.7.

$$Ra = \frac{g\beta D^3\left(T_{\text{wall}} - T_{\text{amb}}\right)}{\nu\alpha} \tag{E.7}$$

This provides a difficulty because T_{wall} is unknown. Additionally, β is defined as $\frac{1}{T_{\text{wall}}}$ so that also cannot be found. This difficulty is overcome by solving the full heat transfer coefficient iteratively. In practice, this is done using Engineering Equation Solver but a guess and check method will be shown here for clarity. To start the guess and check method, a surface temperature of 294 K is used to calculate the Rayleigh number and heat transfer coefficient. Once the total heat transfer is calculated, the surface temperature of the Buna-N is checked and can be readjusted if necessary. The calculation proceeds in equation E.8.

$$\begin{aligned} Ra &= \frac{9.81[\mathrm{m\,s^{-2}}]\frac{1}{294[\mathrm{K}]}\left(0.0476[\mathrm{m}]\right)^3\left(294[\mathrm{K}] - 295.4[\mathrm{K}]\right)}{\left(1.63 \times 10^{-5}[\mathrm{m^2 s^{-1}}]\right)\left(2.31 \times 10^{-5}[\mathrm{m^2 s^{-1}}]\right)} \\ &= 9.06 \times 10^3 \end{aligned} \tag{E.8}$$

This gives the natural convection heat transfer coefficient in equation E.9.

$$\begin{aligned} h &= \left(\frac{0.026[\mathrm{W\,m^{-2}K^{-1}}]}{0.0476[\mathrm{m}]}\right)\left[0.6 + \frac{0.387 \cdot 9006^{1/6}}{\left(1 + \left(\frac{0.559}{0.71}\right)^{9/16}\right)^{8/27}}\right]^2 \\ &= 2.33[\mathrm{W\,m^{-2}K^{-1}}] \end{aligned} \tag{E.9}$$

Using an outer area, A = 0.114 m^2 the convective thermal resistance between the air and the insulation can be calculated to be R_{ins} = 3.77 KW^{-1}.

The last thermal resistance to be calculated for sections 1 and 7 is the radiation resistance. This again is calculated iteratively and is done in practice using Engineering Equation Solver but will be shown using the guess and check method using the same surface temperature from above. Radiation resistance uses the formula from equation E.2 but the heat transfer coefficient, h, is replaced with equation E.10.

$$\begin{aligned} h_{\mathrm{rad}} &= \epsilon\sigma(T_{\mathrm{wall}} + T_{\mathrm{amb}})((T_{\mathrm{wall}}^2 + T_{\mathrm{amb}}^2) \\ &= (1)(5.67 \times 10^{-8})(294[\mathrm{K}] + 295.4[\mathrm{K}])((294[\mathrm{K}])^2 + (295.4[\mathrm{K}])^2) \\ &= 5.73[\mathrm{W\,m^{-2}K^{-1}}] \\ R_{\mathrm{rad}} &= \frac{1}{(5.73[\mathrm{W\,m^{-2}K^{-1}}])(0.114[m^2])} \\ &= 1.51[\mathrm{K\,W^{-1}}] \end{aligned} \tag{E.10}$$

Finally all thermal resistances are recombined into equation E.1 to find the total thermal resistance, shown in equation E.11.

$$\begin{aligned} R_{\mathrm{rad}} &= 0.362[\mathrm{K\,W^{-2}}] + 1.54[\mathrm{K\,W^{-2}}] + 186.7[\mathrm{K\,W^{-2}}] + \frac{(3.77[\mathrm{K\,W^{-2}}])(1.51[\mathrm{K\,W^{-2}}])}{3.77[\mathrm{K\,W^{-2}}] + 1.51[\mathrm{K\,W^{-2}}]} \\ &= 189.7[\mathrm{K\,W^{-2}}] \end{aligned} \tag{E.11}$$

The total thermal resistance from equation E.11 can be used to find the total heat transfer rate in regions 1 and 7, shown in equation E.12.

$$\begin{aligned} Q_{1,7} &= \frac{T_{\mathrm{amb}} - T_{\mathrm{fluid}} -}{R_{\mathrm{th}}} \\ &= \frac{295.4[\mathrm{K}] - 284.7[\mathrm{K}]}{189.7[\mathrm{K\,W^{-1}}]} \\ &= 0.06[W] \end{aligned} \tag{E.12}$$

Evaluating the surface temperature of the Buna-N foam, we find that the prediction of 294 K is lower than the calculated value of 294.4 K. Therefore, the guess is updated and the calculation proceeds again. The change in surface temperature does not affect the answer appreciably and the heat transfer rate is still found to be 0.06 W.

Moving on to regions 2 and 6, the heat transfer through the sight tubes must be calculated. Using a similar thermal resistance network to the one shown above, although with few components, the total thermal resistance can be found. The thermal resistance network used is shown in Figure E.3.

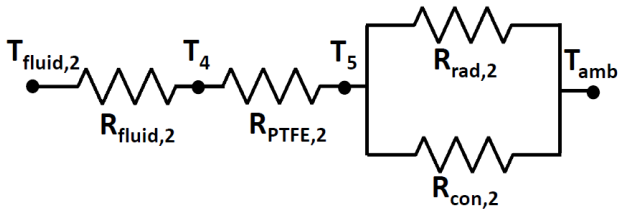

Figure E.3: Thermal resistance network for regions 2 and 6, PTFE sight tubes.

Again, R_{fluid} is calculated with equation E.2 where the heat transfer coefficient, *h*, is calculated using equation E.3. Using an inner diameter of 3.97 mm, the heat transfer coefficient is found to be 417.6 $\mathrm{W\,m^{-2}K^{-1}}$. Using equation E.2, the thermal resistance is found to be 2.5 $\mathrm{K\,W^{-1}}$. Using the thermal resistance formula in equation E.5, with an outer diameter of 6.35 mm and a thermal conductivity of 0.25 $\mathrm{W\,m^{-1}K^{-1}}$, the thermal resistance through the wall is found to be 125.6 $\mathrm{K\,W^{-1}}$. An iterative process must again be used to find the convective heat transfer coefficient on the surface of the PTFE tube. A surface temperature of 293 K is assumed and input into equation E.6. The heat transfer coefficient is found to be 6.35 $\mathrm{W\,m^{-2}K^{-1}}$ which yields a thermal resistance of 103.9 $\mathrm{K\,W^{-1}}$. The radiation heat transfer coefficient is found to be 5.78 $\mathrm{W\,m^{-2}K^{-1}}$ using equation E.10. This yields a thermal resistance of 114.1 $\mathrm{K\,W^{-1}}$. The total thermal resistance is calculated in equation E.13.

$$
\begin{aligned}
R_{\text{th},2,6} &= R_{\text{fluid}} + R_{\text{wall}} + \frac{R_{\text{conv}} \cdot R_{\text{rad}}}{R_{\text{conv}} + R_{\text{rad}}} \\
&= 2.5[\text{K W}^{-1}] + 125.6[\text{K W}^{-1}] + \frac{\left(103.9[\text{K W}^{-1}]\right) \cdot \left(114.1[\text{K W}^{-1}]\right)}{\left(103.9[\text{K W}^{-1}]\right) + \left(114.1[\text{K W}^{-1}]\right)} \\
&= 182.5[\text{K W}^{-1}]
\end{aligned}
\tag{E.13}
$$

This yields a total heat transfer rate of 0.06 W.

Heat transfer in the PEEK manifold is three dimensional. Therfore, a simple thermal resistance network cannot be used. Instead, a thermocouple is placed on the surface of the block and the surface temperature is used to find both conductive and radiative heat rate. This greatly simplified the thermal resistance network, which is shown in Figure E.4 where *h* denotes horizontally oriented surfaces and *v* denote vertically oriented surfaces.

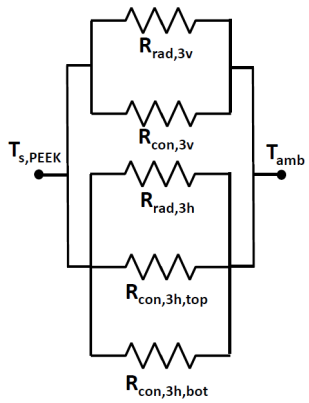

Figure E.4: Thermal resistance network for regions 3 and 5 combined, PEEK manifold.

The natural convection heat transfer coefficient can be found using equation E.14 from [76].

$$
\begin{aligned}
h &= \left(\frac{k}{L}\right)\left(0.68 + \frac{0.670 \cdot Ra^{1/4}}{\left(1 + \left(\frac{0.492}{Pr^{9/16}}\right)\right)^{4/9}}\right) \\
&= \left(\frac{0.03[\text{W m}^{-1}\text{K}^{-1}]}{0.05[\text{m}]}\right)\left(0.68 + \frac{0.670 \cdot 97977^{1/4}}{\left(1 + \left(\frac{0.492}{0.71^{9/16}}\right)\right)^{4/9}}\right) \\
&= 5.64[\text{W m}^{-2}\text{K}^{-1}]
\end{aligned}
\tag{E.14}
$$

This yields a thermal resistance of 23.2 KW^{-1}.

Natural convection for the top surface is calculated from [76] in equation E.15.

$$\begin{aligned} h &= \left(\frac{k}{L}\right)\left(0.27 \cdot Ra^{1/4}\right) \\ &= \left(\frac{0.03[\mathrm{W\,m^{-1}K^{-1}}]}{0.05[\mathrm{m}]}\right)\left(0.27 \cdot 97977^{1/4}\right) \\ &= 2.46[\mathrm{W\,m^{-2}K^{-1}}] \\ R_{\mathrm{th}} &= 517.9[\mathrm{K\,W^{-1}}] \end{aligned} \tag{E.15}$$

Similarly, for the bottom, the heat transfer coefficient and thermal resistance are calculated in E.16

$$\begin{aligned} h &= \left(\frac{k}{L}\right)\left(0.54 \cdot Ra^{1/4}\right) \\ &= \left(\frac{0.03[\mathrm{W\,m^{-1}K^{-1}}]}{0.05[\mathrm{m}]}\right)\left(0.54 \cdot 97977^{1/4}\right) \\ &= 4.93[\mathrm{W\,m^{-2}K^{-1}}] \\ R_{\mathrm{th}} &= 259.0[\mathrm{K\,W^{-1}}] \end{aligned} \tag{E.16}$$

Radiation heat transfer coefficients are calculated as in equation E.10 for all surfaces at once. The radiation heat transfer coefficient of 5.64 $\mathrm{W\,m^{-2}K^{-1}}$ gives a thermal resistance of 113.1 $\mathrm{K\,W^{-1}}$.

This is summed to give the total thermal resistance in equation E.17.

$$\begin{aligned} \frac{1}{R_{\mathrm{th,3,5}}} &= \frac{1}{R_{\mathrm{rad}}} + \frac{1}{R_{\mathrm{con,v}}} + \frac{1}{R_{\mathrm{con,h,top}}} + \frac{1}{R_{\mathrm{con,h,bot}}} \\ &= \frac{1}{113.1[\mathrm{K\,W^{-1}}]} + \frac{1}{23.2[\mathrm{K\,W^{-1}}]} + \frac{1}{517.9[\mathrm{K\,W^{-1}}]} + \frac{1}{259.0[\mathrm{K\,W^{-1}}]} \\ R_{\mathrm{th}} &= 6.7[\mathrm{K\,W^{-1}}] \end{aligned} \tag{E.17}$$

So the combined heat rate in section 3 and 5 is found to be 1.12 W.

The final section of the facility to analyze is the test section itself. Several conservative assumptions are made in this calculation. First, the entire test section is assumed to be an area weighted average temperature instead of taking the temperature profile into account. This is reasonable be-

cause only a small portion of the test section is at the peak heater temperature; the bulk of the surface is near ambient temperature. Next, the electrical harness, which provides insulation over a substantial amount of the test piece surface, is ignored. This is another conservative estimate because included it would reduce the heat transfer rate. Heat transfer through the glass cap is ignored as well and is justified in section 4.1.

First the heat transfer coefficient on the vertical wall is calculated as in equation E.14 and is found to be 10.86 $\mathrm{W\,m^{-2}K^{-1}}$. The radiation heat transfer coefficient for a surface temperature of 312.9 K is 6.39 $\mathrm{W\,m^{-2}K^{-1}}$ yielding a total thermal resistance of 1159.1 $\mathrm{K\,W^{-1}}$ and a heat transfer rate of 0.01 W into the environment.

Summing the heat transfer rates, it is found that total heat transfer from the environment is 1.37 W. A full summary of thermal resistance and heat transfer values is presented in Table E.2.

Table E.2: Total heat transfer from the surroundings.

Section	R_{th} [$\mathrm{K\,W^{-1}}$]	Q [W]
1	189.7	0.06
2	182.5	0.06
3, 5	259.0	1.12
4	1159.1	-0.01
6	182.5	0.06
7	189.7	0.06
Total		1.37

As is shown, thermal interaction with the environment is small and can be ignored. Net heat transfer is into the system, so our calculation of performance is conservative

Appendix F: Model Verification

Model verification is necessary to ensure the model is calculating the two-phase heat transfer coefficient correctly. To do this, local properties such as wall temperature, heat flux, vapor quality, and fluid temperature are taken from the model at a single point. These properties are then used to calculate the two-phase heat transfer coefficient and this value is compared to the model's calculation. For each model, these values are extracted along the center line of the channel floor, 1 mm from the inlet. For the fluid, only temperature and vapor quality are taken from the model; all other fluid properties are calculated to ensure the interpolation files are being read correctly. The four heat transfer coefficient correlations described in this work are validated this way.

F.1 Agostini and Bontemps

First, the two-phase heat transfer coefficient correlation from Agostini and Bontemps is shown because it is simpler to calculate. The values taken from the model are given in Table F.1.

Table F.1: Agostini and Bontemps model values.

Property	Unit	Value
q''	$\mathrm{W\,m^{-2}}$	2.38×10^6
x	–	0.263
T_{fluid}	°C	292.6
T_{wall}	°C	315.48
h_{tp}	$\mathrm{W\,m^{-2}K^{-1}}$	99.1×10^3

The Agostini and Bontemps correlation is shown again in equation F.1.

$$h_{\mathrm{tp}} = 28 \cdot q''^{2/3} \cdot G^{-0.26} \cdot x^{-0.10} \tag{F.1}$$

First, mass flux, G, is calculated using the mass flow value from the experiment as shown in equation F.2.

$$\begin{aligned} G &= \frac{\dot{m}}{w_{\mathrm{c}} \cdot h_{\mathrm{c}} \cdot n_{\mathrm{c}}} \\ &= \frac{8.36 \times 10^{-4}[\mathrm{kg\,s^{-1}}]}{40 \times 10^{-6}[\mathrm{m}] \cdot 200 \times 10^{-6}[\mathrm{m}] \cdot 125} \\ &= 835.8[\mathrm{kg\,m^{-2}s^{-1}}] \end{aligned} \tag{F.2}$$

This is then returned to equation F.1. The calculation is shown in equation F.3.

$$\begin{aligned} h_{\mathrm{tp}} &= 28 \cdot (2.38 \times 10^{6}[\mathrm{W\,m^{-2}}])^{2/3} \cdot (835.8[\mathrm{kg\,m^{-2}s^{-1}}])^{-0.26} \cdot x^{-0.10} \\ &= 99,118[\mathrm{W\,m^{-2}K^{-1}}] \end{aligned} \tag{F.3}$$

This agrees with the heat transfer coefficient from the model.

F.2 Lazarek and Black

Similarly, the Lazarek and Black correlation can be done with a few simple calculations. The values taken from the model are shown in Table F.2.

Table F.2: Lazarek and Black model values.

Property	Unit	Value
q''	$\mathrm{W\,m^{-2}}$	4.17×10^{6}
T_{fluid}	°C	292.7
T_{wall}	°C	304.3
h_{tp}	$\mathrm{W\,m^{-2}K^{-1}}$	356×10^{3}

Again the heat transfer coefficient correlation is shown in equation F.4 along with the definition for the boiling number and Reynolds number.

$$
\begin{aligned}
h_{\mathrm{tp}} &= \frac{k_{\mathrm{l}}}{D_{\mathrm{h}}}\left(Re_{\mathrm{l}}^{0.857} \cdot Bo^{0.714}\right) \\
Bo &= \frac{q''}{G \cdot h_{\mathrm{fg}}} \\
Re_{\mathrm{l}} &= \frac{G \cdot D_{\mathrm{h}}}{\mu}
\end{aligned}
\tag{F.4}
$$

Unlike the Agostini correlation, this correlation requires the interpolation of a physical property, h_{fg}. The values for the interpolated properties are compared for each correlation but not shown here for brevity. A comparison of each property is shown in Section F.4 where most properties are used. The calculation for mass flux, G, is given in equation F.2. The calculation of the two-phase heat transfer coefficient is shown in equation F.5.

$$
\begin{aligned}
Bo &= \frac{4.17 \times 10^{6}[\mathrm{W\,m^{-2}}]}{835.8[\mathrm{kg\,m^{-2}s^{-1}}] \cdot 182.7 \times 10^{3}[\mathrm{J\,kg^{-1}}]} \\
&= 0.027 \\
Re_{\mathrm{l}} &= \frac{4.17 \times 10^{6}[\mathrm{W\,m^{-2}}] \cdot 6.6 \times 10^{-5}[\mathrm{m}]}{8.36 \times 10^{-4}[\mathrm{kg\,s^{-}1}]} \\
&= 268 \\
h_{\mathrm{tp}} &= \frac{0.086[\mathrm{W\,m^{-1}K^{-1}}]}{6.6 \times 10^{-5}[\mathrm{m}]}\left(268^{0.857} \cdot 0.027^{0.714}\right) \\
&= 393.6 \times 10^{3}[\mathrm{W\,m^{-2}K^{-1}}]
\end{aligned}
\tag{F.5}
$$

F.3 Bertsch

The Bertsch correlation is more complicated than the preceding two because requires the interpolation of several properties and the calculation occurs in many discrete steps. The values taken from the model are given in Table F.3.

Again the correlation is shown in equation F.6.

Table F.3: Bertsch model values.

Property	Unit	Value
q''	$\mathrm{W\,m^{-2}}$	1.89×10^6
x	–	0.28
T_{fluid}	°C	292.6
T_{wall}	°C	322.2
h_{tp}	$\mathrm{W\,m^{-2}K^{-1}}$	60.12×10^3

$$
\begin{aligned}
h_{\mathrm{tp}} &= \left(1-x\right)\cdot h_{\mathrm{nb}} + \left[1 + 80\cdot\left(x^2 - x^6\right)\cdot e^{-0.6\cdot Co}\right]\cdot h_{\mathrm{con,tp}} \\
h_{\mathrm{nb}} &= P_{\mathrm{R}}^{0.12-0.2\cdot log_{10}(R_{\mathrm{p}})}\cdot\left[-log_{10}(P_{\mathrm{R}})\right]^{-0.55}\cdot M^{-0.5}\cdot(q'')^{0.67} \\
h_{\mathrm{con,tp}} &= \left(1-x\right)\cdot h_{\mathrm{cb,l}} + x\cdot h_{\mathrm{cb,v}} \\
h_{\mathrm{con,a}} &= \left(3.66 + \frac{0.0668\cdot\frac{D_{\mathrm{h}}}{L}Re_{\mathrm{a}}Pr_{\mathrm{a}}}{1+0.04\cdot\left[\frac{D_{\mathrm{h}}}{L}\cdot Re_{\mathrm{a}}\cdot Pr_{\mathrm{a}}\right]^{2/3}}\right)\cdot\frac{k_{\mathrm{a}}}{D_{\mathrm{h}}}
\end{aligned}
\tag{F.6}
$$

Here the a in $h_{\mathrm{con,a}}$ denotes either the liquid or vapor phase.

The calculation is broken up into several parts for clarity. We begin with the calculation of the liquid and vapor convective boiling terms in equation F.7. These are used to calculated the entire convective boiling term.

$$
\begin{aligned}
Re_{\mathrm{v}} &= \frac{835.8[\mathrm{kg\,m^{-2}s^{-1}}] \cdot 6.67 \times 10^{-5}[\mathrm{m}]}{1.17 \times 10^{-5}[\mathrm{kg\,m^{-1}s^{-1}}]} \\
&= 4753 \\
h_{\mathrm{con,l}} &= \left(3.66 + \frac{0.0668 \cdot \frac{6.67\times10^{-5}[\mathrm{m}]}{1\times10^{-3}[\mathrm{m}]} 4753 \cdot 3.4}{1 + 0.04 \cdot \left[\frac{6.67\times10^{-5}[\mathrm{m}]}{1\times10^{-3}[\mathrm{m}]} \cdot 4753 \cdot 0.83\right]^{2/3}} \right) \cdot \frac{3.4[\mathrm{W\,m^{-1}K^{-1}}]}{6.67 \times 10^{-5}[\mathrm{m}]} \\
&= 5032[\mathrm{W\,m^{-2}K^{-1}}] \\
Re_{\mathrm{l}} &= \frac{835.8[\mathrm{kg\,m^{-2}s^{-1}}] \cdot 6.67 \times 10^{-5}[\mathrm{m}]}{2.08 \times 10^{-4}[\mathrm{kg\,m^{-1}s^{-1}}]} \\
Re_{\mathrm{l}} &= 267.6 \\
h_{\mathrm{con,v}} &= \left(3.66 + \frac{0.0668 \cdot \frac{6.67\times10^{-5}[\mathrm{m}]}{1\times10^{-3}[\mathrm{m}]} 267.6 \cdot 0.83}{1 + 0.04 \cdot \left[\frac{6.67\times10^{-5}[\mathrm{m}]}{1\times10^{-3}[\mathrm{m}]} \cdot 267.6 \cdot 0.83\right]^{2/3}} \right) \cdot \frac{0.014[\mathrm{W\,m^{-1}K^{-1}}]}{6.67 \times 10^{-5}[\mathrm{m}]} \\
&= 856.8[\mathrm{W\,m^{-2}K^{-1}}] \\
h_{\mathrm{con,tp}} &= \big(1 - x\big) \cdot 5032[\mathrm{W\,m^{-2}K^{-1}}] + x \cdot 856.3[\mathrm{W\,m^{-2}K^{-1}}] \\
&= 6694[\mathrm{W\,m^{-2}K^{-1}}]
\end{aligned}
\tag{F.7}
$$

Next the nucleate boiling term is calculated. Here the molar mass was input directly. Reduced pressure is calculated. The fluid pressure was found by taking the saturation pressure at the temperature given in Table F.3.

$$
\begin{aligned}
P_{\mathrm{R}} &= \frac{P_{\mathrm{fluid}}}{P_{\mathrm{crit}}} \\
&= \frac{562.1[\mathrm{kPa}]}{4,058[\mathrm{kPa}]} \\
&= 0.14 \\
h_{\mathrm{nb}} &= 55 \cdot 0.14^{0.12 - 0.2 \cdot log_{10}(1[\mu\mathrm{m}])} \cdot \big(- log_{10}(0.14)\big)^{-0.55} \\
&\quad \times 102[\mathrm{kg\,kmol^{-1}}] \cdot (1.89 \times 10^{6}[\mathrm{W\,m^{-2}}])^{0.67} \\
&= 74.8 \times 10^{3}[\mathrm{W\,m^{-2}K^{-1}}]
\end{aligned}
\tag{F.8}
$$

Finally, the confinement number can be calculated and the convective and nucleate boiling terms can be used to find the total two-phase heat transfer coefficient.

$$
\begin{aligned}
Co &= \Big(\frac{\sigma}{g \cdot (\rho_\mathrm{l} - \rho_\mathrm{v}) D_\mathrm{h}^2}\Big)^{1/2} \\
&= \Big(\frac{8.76 \times 10^{-3}[\mathrm{N\,m^{-1}}]}{9.8[\mathrm{m\,s^{-2}}] \cdot (1227[\mathrm{kg\,m^{-3}}] - 27.3[\mathrm{kg\,m^{-3}}])(6.67[\mathrm{m}])^2}\Big)^{1/2} \\
&= 12.6 \\
h_\mathrm{tp} &= \big(1 - x\big) \cdot 74.8 \times 10^3[\mathrm{W\,m^{-2}K^{-1}}] \\
&\quad + \big[1 + 80 \cdot \big(0.28^2 - 0.28^6\big) \cdot e^{-0.6 \cdot 12.6}\big] \cdot 6694[\mathrm{W\,m^{-2}K^{-1}}] \\
&= 60.5 \times 10^3[\mathrm{W\,m^{-2}K^{-1}}]
\end{aligned}
\tag{F.9}
$$

F.4 Kim and Mudawar

The correlation from Kim and Mudawar is similarly complicated. This correlation relies heavily on interpolated fluid properties so a comparison of the values calculated in COMSOL to those retrieved from EES will be shown. This is presented in Table F.4.

Table F.4: Comparison of interpolated properties from COMSOL to those retrieved from EES.

Property	Unit	COMSOL Value	EES Value
mu_l	$\mathrm{kg\,m^{-1}s^{-1}}$	2.08×10^{-4}	2.08×10^{-4}
mu_v	$\mathrm{kg\,m^{-1}s^{-1}}$	1.17×10^{-5}	1.17×10^{-5}
h_fg	$\mathrm{J\,kg^{-1}}$	1.83×10^5	1.83×10^5
rho_l	$\mathrm{kg\,m^{-3}}$	1227.0	1227.0
rho_v	$\mathrm{kg\,m^{-3}}$	27.42	27.32
σ	$\mathrm{N\,m^{-1}}$	8.75×10^{-3}	8.76×10^{-3}
k_l	$\mathrm{W\,m^{-1}K^{-1}}$	0.086	0.0858

The values taken from COMSOL used in this calculation are given in Table F.5.

The series of equations for this correlation are given in equation F.10.

Table F.5: Kim and Mudawar model values.

Property	Unit	Value
q''	$\mathrm{W\,m^{-2}}$	4.39×10^6
x	–	0.24
T_{fluid}	°C	292.7
T_{wall}	°C	302.9
h_{tp}	$\mathrm{W\,m^{-2}K^{-1}}$	4.24×10^5

$$
\begin{aligned}
h_{\mathrm{tp}} &= \left(h_{\mathrm{nb}}^2 + h_{\mathrm{cb}}^2\right)^{1/2} \\
h_{\mathrm{nb}} &= \left[2345\left(Bo\frac{P_{\mathrm{H}}}{P_{\mathrm{W}}}\right)^{0.70} P_{\mathrm{R}}^{0.38}\left(1-x\right)^{-0.51}\right]\left(0.023 \cdot Re_{\mathrm{l}}^{0.8} Pr_{\mathrm{l}}^{0.4}\frac{k_{\mathrm{l}}}{D_{\mathrm{h}}}\right) \\
h_{\mathrm{cb}} &= \left[5.2\left(Bo\frac{P_{\mathrm{H}}}{P_{\mathrm{W}}}\right)^{0.08} We_{\mathrm{lo}}^{-0.54} + 3.5\left(\frac{1}{X_{\mathrm{tt}}}\right)\left(\frac{\rho_{\mathrm{v}}}{\rho_{\mathrm{l}}}\right)^{0.25}\right]\left(0.023 \cdot Re_{\mathrm{l}}^{0.8} Pr_{\mathrm{l}}^{0.4}\frac{k_{\mathrm{l}}}{D_{\mathrm{h}}}\right)
\end{aligned}
\tag{F.10}
$$

The definitions for the boiling number, Bo, the liquid only Weber number, We_{lo}, and the turbulent-turbulent Martenelli parameter, X_{tt} are given in equation F.11. The calculation of these parameters, as well as the liquid Reynolds number, Re_{l}, is shown here.

$$
\begin{aligned}
Bo &= \frac{q''}{G \cdot h_{\mathrm{fg}}} \\
&= \frac{4.39 \times 10^{6}[\mathrm{W\,m^{-2}}]}{835.6[\mathrm{kg\,m^{-2}s^{-1}}] \cdot 1.83 \times 10^{5}[\mathrm{J\,kg^{-1}}]} \\
&= 0.0287 \\
We_{\mathrm{lo}} &= \frac{G^2 D_{\mathrm{h}}}{\rho_{\mathrm{l}} \cdot \sigma} \\
&= \frac{\left(835.6[\mathrm{kg\,m^{-2}s^{-1}}]\right)^2 \cdot 6.67 \times 10^{-5}[\mathrm{m}]}{1227[\mathrm{kg\,m^{-3}}] \cdot 8.76 \times 10^{-3}[\mathrm{N\,m^{-1}}]} \\
&= 4.33 \\
X_{\mathrm{tt}} &= \left(\frac{\mu_{\mathrm{l}}}{\mu_{\mathrm{v}}}\right)^{0.1} \\
&= \left(\frac{2.08 \times 10^{-4}[\mathrm{kg\,m^{-1}s^{-1}}]}{1.17 \times 10^{-5}[\mathrm{kg\,m^{-1}s^{-1}}]}\right)^{0.1} \\
&= 7.33 \\
Re_{\mathrm{l}} &= \frac{G \cdot D_{\mathrm{h}}}{mu_{\mathrm{l}}} \\
&= \frac{835.6[\mathrm{kg\,m^{-2}s^{-1}}] \cdot 6.67 \times 10^{-5}[\mathrm{m}]}{2.08 \times 10^{-4}[\mathrm{kg\,m^{-1}s^{-1}}]} \\
&= 267.6
\end{aligned}
\tag{F.11}
$$

Finally these values can be returned to equation F.10. This calculation is shown in equation F.12.

$$
\begin{aligned}
h_{\mathrm{nb}} &= \Big[2345\Big(0.0287\frac{4.4\times10^{-4}[\mathrm{m}]}{4.8\times10^{-4}[\mathrm{m}]}\Big)^{0.70}0.14^{0.38}\Big(1-0.24\Big)^{-0.51}\Big] \\
&\quad\times\Big(0.023\cdot267.6l^{0.8}562.1l^{0.4}\frac{0.085[\mathrm{W\,m^{-1}K^{-1}}]}{6.67\times10^{-5}[\mathrm{m}]}\Big) \\
&= 4.23\times10^{6}[\mathrm{W\,m^{-2}K^{-1}}]
\end{aligned}
$$

$$
\begin{aligned}
h_{\mathrm{c}}b &= \Big[5.2\Big(0.0287\frac{4.4\times10^{-4}[\mathrm{m}]}{4.8\times10^{-4}[\mathrm{m}]}\Big)^{0.08}4.33^{-0.54}+3.5\Big(\frac{1}{7.33}\Big)\Big(\frac{27.32[\mathrm{kg\,m^{-3}}]}{1227[\mathrm{kg\,m^{-3}}]}\Big)^{0.25}\Big] \\
&\quad\times\Big(0.023\cdot267.6^{0.8}3.4^{0.4}\frac{0.085[\mathrm{W\,m^{-1}K^{-1}}]}{6.67\times10^{-5}[\mathrm{m}]}\Big) \\
&= 8.33\times10^{3}[\mathrm{W\,m^{-2}K^{-1}}]
\end{aligned}
\tag{F.12}
$$

$$
\begin{aligned}
h_{\mathrm{tp}} &= \Big(4.23\times10^{6}[\mathrm{W\,m^{-2}K^{-1}}]+(8.33\times10^{3}[\mathrm{W\,m^{-2}K^{-1}}])^{2}\Big)^{1/2} \\
&= 4.23\times10^{5}[\mathrm{W\,m^{-2}K^{-1}}]
\end{aligned}
$$